High-resolution X-ray plasma diagnostics of stellar coronae

Dissertation
zur Erlangung des Doktorgrades
des Fachbereichs Physik
der Universität Hamburg

vorgelegt von
Jan-Uwe Ness

geboren in **Oldenburg (Oldenburg)**

Hamburg
Januar 2002

Gutachter der Dissertation	:	Prof. Dr. Jürgen H.M.M. Schmitt
		Prof. Dr. Dieter Reimers
Gutachter der Disputation	:	Prof. Dr. Jürgen H.M.M. Schmitt
		Prof. Dr. Heinrich J. Wendker
Datum der Disputation	:	5. März 2002
Dekan des Fachbereiches Physik und		
Vorsitzender des Promotionsausschusses	:	Prof. Dr. F.-W. Büßer

Zusammenfassung

Mit der Entdeckung der Sonnenflecken im 17. Jahrhundert wurde ein neues Arbeitsfeld der Astronomie eröffnet. Der physikalische Ursprung dieser dunklen Flecken auf der Sonnenoberfläche ist aufs Engste mit starken magnetischen Feldern verknüpft. Als weiteres spektakuläres Phänomen ist die Korona der Sonne zu nennen, die sich in den äußersten Schichten der Sonne befindet. Die extrem hohe Temperatur verbunden mit einer sehr geringen Dichte wirft eine Menge Fragen auf, und auch hier spielt die magnetische Aktivität eine fundamentale Rolle. In der vorliegenden Arbeit wird eine Einführung in eine lange Tradition von Beobachtungen der Korona der Sonne, insbesondere im Röntgenspektralbereich, gegeben. Angefangen mit erdgebundenen Beobachtungen der sichtbaren Korona, über Spektraluntersuchungen im Röntgenbereich, bis hin zu eindrucksvollen Bildern mit hoher räumlicher Auflösung, wird ein Überblick über die Geschichte der Untersuchung der Sonnenkorona gegeben. Es hat sich gezeigt, dass das koronale Plasma hoch strukturiert und in bogenartigen Strukturen komprimiert ist, die große Ähnlichkeit mit geschlossenen Magnetfeldlinien haben.
Weitaus schwieriger ist die Untersuchung stellarer Koronen, die sich als räumlich nicht auflösbare Röntgenquellen präsentieren. Von den Röntgenmissionen *Einstein* und ROSAT weiß man, dass die Entstehung von Koronen ein natürlicher Prozess sein muss, der immer am Übergang zwischen der Photosphäre später Sterne und dem Weltraum auftritt. Eine Klassifikation von Röntgenquellen, die Röntgeneigenschaften mit fundamentalen stellaren Parametern ähnlich einem Hertzsprung-Russell Diagramm verknüpft, wäre sehr wünschenswert, jedoch wurde bisher nur ein Zusammenhang zwischen der Rotationsperiode und der Röntgenleuchtkraft gefunden.
Neue Horizonte eröffnen sich mit den neuen Röntgenmissionen *Chandra* und XMM, mit denen hochaufgelöste Röntgenspektroskopie möglich ist. Die Emissionslinien, die man mit diesen Teleskopen messen kann, werden in der vorliegenden Arbeit zur Herleitung physikalischer Eigenschaften der Koronen von Capella, Algol und Procyon verwendet. Vier weitere Sterne werden analysiert, jedoch weniger detailliert. Eine spezielle Software ist im Rahmen dieses Projektes entstanden, und der Algorithmus ist speziell für die Analyse von *Chandra* LETGS Spektren ausgelegt, ist jedoch hinreichend allgemein, dass er für alle möglichen Arten von Spektren mit niedrigen Zählraten nützlich sein sollte wie z. B. XMM-RGS Daten.
Eine Voranalyse der Spektren ergibt eine Verteilung unterschiedlicher Plasmaschichten, z. B. verschiedener Temperaturen. Zumindest eine heiße und eine kühlere Komponente sind für die aktiven Sterne Algol und Capella gefunden worden, nicht jedoch z. B. für den inaktiven Stern Procyon, der nur kühles Material zu haben scheint. Effekte optischer Tiefen wurden untersucht und können als vernachlässigbar angesehen werden. Das Kontinuum des Spektrums von Algol wurde untersucht und stimmt sehr gut mit einem Bremsstrahlungsspektrum überein. Aus diesem Fit wurde die höchste Temperatur und ein Emissionsmaß hergeleitet.
Das Hauptaugenmerk der vorliegenden Arbeit liegt auf Dichtemessungen mit Hilfe der He-

artigen Tripletts. Koronale Plasmen der Sterne Capella, Procyon, Algol, ϵ Eri, α Cen A und B und UX Ari wurden mit dieser Methode untersucht. Für diese sieben Sterne habe ich im Wesentlichen Dichten gefunden, die am unteren Rand des Sensitivitätsbereiches der He-artigen Tripletts liegen. Für Algol ergeben sich höhere Dichten, dieses Ergebnis kann jedoch auch von der Stärke des Einflusses des UV Strahlungsfeldes, das vom benachbarten B Stern ausgesandt wird, abhängen. Es wurde kein überzeugender Trend gefunden, der den Schluss zuließe, dass aktive Sterne höhere Dichten aufweisen, es ist jedoch bemerkenswert, dass die aktiven Sterne, bei denen ich niedrige Dichten gemessen habe, alle so genannte RS CVn Systeme sind, Doppelsterne, in denen beide Komponenten eine heiße Korona besitzen können. Wechselwirkungen zwischen diesen beiden Koronen sind durchaus denkbar. Sehr viel überzeugender stellt sich der Trend dar, dass aktive Sterne eine heiße Komponente besitzen, während die inaktiven Sterne nur eine „kühle" Komponente mit Plasmatemperaturen um 2 MK haben.
Die niedrigen Dichten können verwendet werden, um einschränkende Aussagen über strukturelle Aspekte wie z. B. die Loopskalenlänge oder Füllfaktoren treffen zu können. Diese Informationen versetzen uns in die Lage, stellare Koronen mit der Sonne sowie miteinander zu vergleichen. Die Dichten, die man für die Sonnenkorona gemessen hat, sind vergleichbar mit den Dichten, die ich in der vorliegenden Arbeit für inaktive Sterne gemessen habe. Die Loopskalenlängen können demnach ähnlich denen der Sonne sein, so dass diese Koronen mit der der Sonne vergleichbar sein können. Ein ganz anderes Bild muss für die aktiven Sterne gemacht werden, die ein viel größeres Emissionsmaß „unterbringen" müssen. Dies kann in Strukturen, die mit denen in der Sonne vergleichbar sind, aber mit höheren Dichten geschehen oder in viel größeren Strukturen mit dann vergleichbaren Dichten, bzw. höheren Füllfaktoren. Die Koronen, die sich auf nur einen Stern beschränken, wie z. B. im Algolsystem, scheinen eher die erste Option zu wählen, während bei den RS CVn Systemen eine Art Doppelkorona entstehen kann, die sehr große Volumina mit geringen Dichten ausfüllt. Diese beiden möglichen Konfigurationen sollten jedenfalls mit besonderer Aufmerksamkeit behandelt werden.

Abstract

With the discovery of sunspots in the 17^{th} century a new field of work in Astronomy was opened. The physical origin of these dark spots on the solar surface has been found to be tightly connected with the presence of strong magnetic fields. Another spectacular phenomenon is the solar corona, the outermost region of the Sun. The high temperature found in the corona in connection with a very low density has posed a lot of questions. Again, the magnetic activity of the Sun seems to play a fundamental role in controlling the processes observed in the solar corona. An introduction for a long tradition of observing the solar corona especially in the X-ray wavelength band is given in this work. Starting with earth-bound observations of the visible corona, and proceeding with spectral diagnostics, impressive pictures with high spatial resolution are presented. A detailed structure with the distribution of the coronal plasma, obviously confined to loop-like structures following closed magnetic field lines, is seen on these pictures.

As a far more difficult task, the observation of stellar coronae, which are not spatially resolvable, is introduced. From X-ray observations carried out with the satellites *Einstein* and ROSAT it is known that the formation of coronae must be a common phenomenon in all late-type stars that occurs at the transition from a cool star's photosphere to space. A classification of X-ray properties similar to a Hertzsprung-Russell diagram connecting X-ray emission with fundamental stellar parameters is desirable, but only the rotation of cool stars has so far been found to be connected with X-ray emission.

New approaches can be made using the recent X-ray missions *Chandra* and XMM, which allow high spectral resolution. The emission lines observable with these missions are used for deriving physical properties of the coronae of Capella, Algol, and Procyon. Four more cool stars are analyzed, but in less detail. A special software has been developed in the frame of this work, the algorithm being especially dedicated to *Chandra* LETGS spectra, but also useful for all kinds of spectral data, e.g., XMM-RGS.

Preliminary analysis of the spectra yields a distribution of plasma layers with different properties, e.g., temperatures. At least a high temperature and a low temperature component is found for the active stars Algol and Capella, but not for the inactive star Procyon. Optical depth effects seem to be negligible, such that the basic assumption of an optically thin plasma is justified at least within the scope of the current data. The continuum of Algol's coronal X-ray spectrum can be fitted by a bremsstrahlung continuum, and an upper temperature as well as an emission measure are derived from the analysis of the continuum.

The main focus of this work is the application of the method of He-like triplets for deriving plasma densities. The coronal plasmas for Capella, Procyon, Algol, ϵ Eri, α Cen A and B, and UX Ari are probed. I generally find low densities for most of these seven stars and higher densities only for ϵ Eri and Algol. For Algol this result depends, however, on the influence of the UV

radiation field emitted by the B star companion. No convincing trend could be found allowing the general conclusion of higher densities in more active stars. It is noteworthy, however, that active stars with lower densities as e.g., Capella are all RS CVn systems, i.e., binaries comprising two cool stars, possibly each of them sustaining a hot corona. An interaction between these two coronae is well conceivable. Quite convincing though is the trend of the presence of hot plasma in the more active stars, while inactive stars only have a "cool" component around 2 MK.

At low densities constraints on parameters connected with structural information as, e.g., the loop scale length or filling factors can be made. That information enables us to compare stellar coronae with the solar corona. The densities measured for the solar corona are comparable with densities measured in inactive stars. Loop scale lengths can therefore be assumed to be very similar to the Sun, such that the structural properties of these coronae are likely the same as observed for the Sun. A different picture must be drawn for the more active stars, which have to accommodate the higher emission measure either in structures with similar sizes but higher densities, or they are characterized by a plasma distribution with higher filling factors. An isolated active corona as, e.g., in the Algol system seems to prefer the first option, while RS CVn systems can well harbor a binary corona with a large volume and low densities. Therefore these two configurations must be treated differently.

Acknowledgments

This thesis would not have been possible without the contributions of a large number of individuals. In particular, I would like to express my deep gratitude to my supervisor **Prof. Dr. Jürgen H.M.M. Schmitt**, who provided me with constant and excellent support during the course of this work. I especially appreciate his valuable advice and his bright spirit providing me with a lot of enthusiasm. In addition, he patronized my scientific career with his readiness to let me benefit from his excellent connections and his broad experience.
It was always a great pleasure to discuss with **Dr. Vadim Burwitz**, and I appreciate his generosity in every concern. Particularly, his help in reducing the *Chandra* LETGS data providing me with most useful data was an essential element of this work.
A lot of experience in programming, Linux, ANSI C, GUI programming, etc., I owe to **Dr. Rainer Wichmann**, a pleasant fellow and room-mate, whose reliability and experience, but also his special character were of high value for me. I appreciate his contribution to the CORA program and to Chapter 2, and the collaboration in this project was very fruitful.
Dr. Matthias Hünsch gave me the idea to work with Jürgen Schmitt. I never regretted to follow his advice. I appreciate that he carried me through critical times during the work, and his careful reading of my thesis.
During my visit to Utrecht, **Dr. Rolf Mewe** cared for me with important insights into SRON, the Space Research Organization of the Netherlands, and provided me with interesting data, which enabled me to work out results presentable to the scientific community.
An important aspect to mention is the cooperation with my **co-authors** in the publications who contributed to the work with ideas and criticism, which helped to improve the results. Special thanks to the **principal investigators** of the instruments. Without their efforts, no scientific work would be possible.

My colleagues **Dr. Rainer Wichmann**, **Dr. Marc Hempel**, **Ansgar Reiners**, **Birgit Fuhrmeister**, and **Nadine Nettelmann** gave me valuable corrections for wording, grammar, and helped me to remove a tremendous number of obsolete commas.

I thank **Marc Audard** for careful reading with useful ideas, and **Dr. Manuel Güdel** for useful discussion and contributing with Fig. 1.5.

All work is not possible without good friends. I am glad that I have a number of friends, and I would like to mention my closest friends **Markus Götze**, **Volkmar Niemann**, and **Reinhold Bussmann**, who also supported this work with his experience in grammar and language.

Special thanks to **my parents**, who taught me the ambition and the idealism to stay the course through this work.

I acknowledge financial support from Deutsches Zentrum für Luft- und Raumfahrt e.V. (**DLR**) under 50OR98010.

Contents

Chapter 1

Introduction

1.1 General

The detailed investigation of the Sun in the 17$^{\text{th}}$ century by Galilei (1613) revealed the solar surface being not as uniform as was expected. Instead, a number of dark spots was discovered, and later (Schwabe 1856) the 11-year cycle with varying frequency of sunspots was found. While the undisturbed solar surface has a temperature of about $T_{\text{eff}} = 5700$ K, the spots are darker because the temperature in the spots is about 1200 K lower. Strong magnetic fields are measured in the center of sunspots by use of the Zeeman effect (Hale 1908, King 1934). The number of spots can therefore be considered a measure for magnetic activity of the Sun.

The corona (a word from the Latin meaning of crown) is the outermost region of the solar atmosphere. But, due to it's faintness, the corona is visible only during total solar eclipses when light from the solar surface is blocked by the Moon. Changes in the solar corona definitely correlate with sunspots (cf. Fig. 1.1) and the sunspot cycle. The magnetic activity is therefore tightly connected with the behavior of the corona.

The discovery of highly ionized iron by Grotrian (1939) revealed that the corona of the Sun must be very hot ($\sim 10^6$ K $= 1$ MK). Large quantities of X-rays can therefore be produced while the cooler solar surface produces no X-ray emission at all (cf. Fig 1.1, right panel). In Fig. 1.1 the Sun in the visible light with sunspots is seen in the left image, and in the right panel an X-ray image taken at the same time is shown. From the X-ray image it is clearly visible that the bright parts of the X-ray corona are associated with sunspots (Fig. 1.1, left panel) with particularly bright X-ray emission at the locations of the sunspots. The bright parts of the X-ray corona are called active regions, while X-ray dark regions can be seen at the poles, called coronal holes. The shape of the corona as seen in X-rays is also known to change with the sunspot cycle.

Since the surface of the Sun is too cold to produce any X-rays, the X-ray emission produced by the Sun originates exclusively from the hot corona. An analysis of the X-ray emission produced by the Sun will therefore give information about the properties and the behavior of the solar corona.

The strong magnetic fields found in the sunspots in connection with X-ray emitting plasma associated with the sunspots, makes X-ray emission a good tracer for magnetic activity.

The investigation of solar-like stars and their coronal activity is motivated by the lack of knowledge of long-term variablity of the Sun. A well known example is the *Maunder Minimum*, a period of about 70 years during the 17$^{\text{th}}$ century, shortly after the discovery of the sunspots, during which the solar activity was significantly reduced compared to that before today. We cannot travel back in time, we cannot make the Sun repeat the *Maunder Minimum* or evolve any faster. But other stars experiencing a similar evolution may be in a different stage of evolution today. X-ray observations of solar-like stars can give an idea of

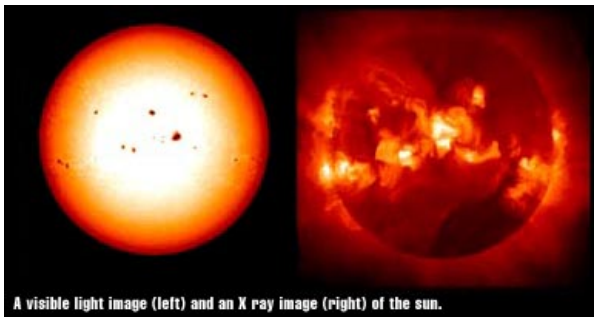

Figure 1.1: *Comparison of the Sun in visible light (left) and in X-ray light (right). Clearly visible is the correlation between the location of sunspots and the intensity in X-ray light.*

how typical the Sun is in the stellar context. Particular problems with stellar observations arise from the fact that no spatial resolution can be achieved in any spectral range, especially not in X-rays. When investigating stellar coronae one therefore has to rely exclusively on spectral diagnostics and light curves. In some very special cases, eclipse mapping can be carried out in order to obtain structural information, e.g., locating hot spots. The challenges in doing this comprise obtaining X-ray spectra with sufficient resolution and finding adequate diagnostic methods, yielding reliable results.

1.2 Solar and stellar activity

The corona of the Sun is the only corona which can be resolved spatially with current X-ray telescopes. Consequently, the solar corona is quite well known, while the spatial distribution of the coronal plasma in other stars can only be deduced from the analogy to the Sun. Before the invention of the coronograph by Lyot in 1930, coronal observations were restricted to (short) times of total solar eclipses. Direct measurements of magnetic fields in the solar corona are still not possible today.
In the late thirties, Grotrian (1939) and Edlén identified the until then mysterious spectral emission lines observed in the spectrum of the solar corona taken from the limb. They found them to be forbidden transitions of highly ionized iron (Fe), calcium (Ca), and nickel (Ni). These kinds of transitions are only possible in a very hot and tenuous plasma. The question why the solar corona is so hot (more than 1 million degrees K) has been one of the most exciting puzzles in astrophysics for the last 60 years, and no definite answer to that question has been found yet. Besides the high temperature the solar corona has a very low density. Therefore, only a small fraction of the total energy out put from solar is required to heat the corona. The total power emitted in X-rays is only about one-millionth of the solar total luminosity, so there is enough energy in the Sun to heat the corona. An important question, however, is how the energy is transported up to the corona, and what mechanism is responsible for the dissipation of the energy in the corona. According to thermodynamics heating by radiation or heat conduction from the cooler photosphere can be excluded. Therefore non-thermal processes are to be considered. Over the years several different mechanisms of powering the corona have been proposed and models of mechanical processes as, e.g., acoustic waves rivaled with magnetic processes as, e.g., Alfvén waves, for a long time. At first the model of acoustic waves was favored: Shock waves in the upper convection zone, caused by rising convective elements, accelerate with the decreasing density, until the local sound speed is reached. The sound speed is the velocity at which pressure waves propagate. The resulting shock-wave dissipates the energy in the corona. With X-ray observations carried out with an imaging X-ray telescope on board Skylab, the spatial distribution of coronal plasma was discovered in 1973. It was clearly shown that the X-ray emitting plasma is concentrated in small structures, instead of being distributed homogeneously. Especially the strong spatial coincidence of X-ray bright regions with active regions casted doubt on the acoustic heating process, and it is now commonly accepted that magnetic fields do play a fundamental role in solar and stellar activity. A dynamo-process (Parker 1979) suggests that in the frame of differential rotation poloidal

(meridional) magnetic fields are converted into toroidal fields and vice versa. Differential rotation means a lattitude dependent angular velocity. The angular velocity for then Sun is by 20% larger at the equator compared to the poles. When the toroidal fields reach the surface they form the active regions. The connection between magnetic activity and both the presence of outer convection zones and rotational velocities is qualitatively plausible, however, the exact details how the corona is heated to the measured temperatures is not well understood.

With a number of rocket flights in the sixties and short satellite missions, e.g., the Orbiting Solar Observatories (OSO 1-8) that flew in the years 1962–1978, X-ray spectroscopy was carried out for the solar corona. Measurements of temperatures and densities were possible, but little structural information about the spatial distribution of X-ray emitting material was obtained. One highlight was the discovery of the He-like triplets (cf. Sect. 1.4.1) and the sensitivity of the ratio of two emission lines to the plasma density (Gabriel & Jordan 1969). Stellar X-ray spectroscopy, however, was not possible with these instruments due to lack of sensitivity.

With the imaging telescopes flown on Skylab (1973), YOHKOH (1991), EIT (Extreme ultraviolet Imaging Telescope) on SOHO (1995), and TRACE (1998), an impressive record of the ever changing appearance of the solar X-ray corona has been obtained. A special mission dedicated to the investigation of the polar regions of the Sun is Ulysses (1990). The most characteristic features of the solar corona are its complex structure and its strong variability. Some features (e.g., coronal holes) persist over time scales of months, even years, but others (e.g., X-ray bright points) appear or disappear over timescales of hours. The spatial distribution of the coronal plasma resembles very much the typical magnetic field topology expected for the Sun. Magnetically open regions, e.g., coronal holes at the poles, are X-ray dark, and are in parallel the source of the high-speed solar wind. Magnetically closed regions have arch-like structures (loops) as can be seen in Fig. 1.2. A scaling law has been found by Rosner *et al.* (1978) relating the temperature maximum with the pressure and the semi-loop length L (cf. Sect 1.4.5).

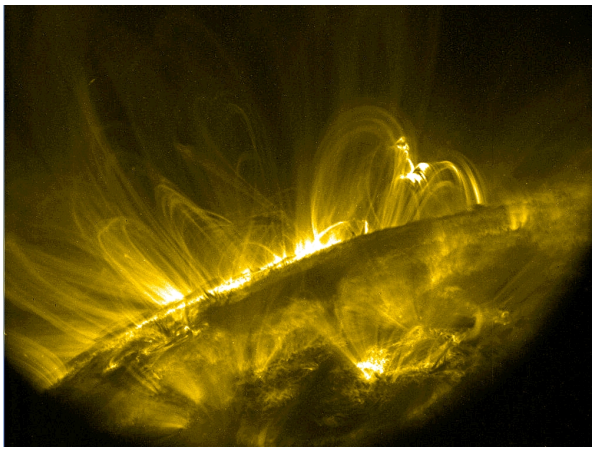

Figure 1.2: *The solar corona in the light of Fe*IX *at 171 Å, i.e., at a temperature of 1 million degrees. Loop-like structures with all kinds of spatial scales resembling a magnetic topology can be identified.*

From the chronologic order it can be seen that basically at first only the (faint) optical luminosity of the solar corona was noticed although some structural features were also recognized in white light. Only the spectral analysis beginning in the thirties gave first results for physical properties of the solar corona, while much later the direct spatial and temporal resolution of X-ray emitting coronal features became available. In the same chronological order the investigation of stellar coronae took place. Stellar activity is deduced from the X-ray luminosity L_X ranging between 10^{25} erg/s and more than 10^{32} erg/s for the most active stars (cf. Hünsch *et al.* 1998, Hünsch *et al.* 1999), and a major breakthrough in our understanding of stellar coronae and stellar activity has been accomplished by the *Einstein* mission (1978–1981) and the ROSAT mission (1990–1999). These missions demonstrated the ubiquity of stellar X-ray emission by showing that almost all classes of stars are capable of sus-

taining hot coronae (e.g., Vaiana *et al.* 1981, Schmitt *et al.* 1995, Schmitt 1997). One of the major findings of stellar X-ray astronomy is the fact that indeed all late-type main sequence stars are surrounded by coronae (Schmitt *et al.* 1995, Schmitt 1997). Conducting volume-limited surveys of X-ray emission from nearby stars using the ROSAT all-sky survey and the ROSAT pointing program, detection rates of 100 % among the F, G, K, and M dwarfs in the immediate solar neighborhood were obtained. This implies that coronal formation has to be considered a universal process that occurs at the transition from a cool star's photosphere to space. Furthermore, if one adopts the "canonical" view that the observed activity in X-rays is of magnetic origin, this finding implies that magnetic field generation in late-type stars must be ubiquitous as well.
As can be seen from Fig. 1.3, the X-ray surface brightness does not depend on the spectral type, such that a classification of X-ray properties will have to be defined on other scales but the spectral type. The only fundamental stellar parameter related to X-ray emission from cool stars, is the rotation (and the age) so far. Other stellar parameter as, e.g., the mass or the radius are to present knowledge not suited to predict X-ray emission properties, and finding classification schemes is a major challenge for present and future investigation.

The limited energy resolution of the ROSAT PSPC (Position Sensitive Proportional Counter) has been used to determine the so-called hardness ratio HR=(H-S)/(H+S), a measure for the mean energy of the collected X-ray photons. The hardness ratio yields a high value close to +1, in the case that most of the photons are measured in the hard band H, and a low value close to -1 in the case that most of the photons are found in the soft energy band S. The hardness ratio of the complete sample of nearby stars as measured by Schmitt (1997) is shown in Fig. 1.4. A trend of harder X-ray emission for stars with more X-ray output can be seen. From this trend the usage of the X-ray luminosity as a measure for activity seems to be justified. Schmitt (1997) finds the median of the observed X-ray luminosity distribution function to be at log $L_X = 27.5$, which is somewhat above the typical solar maximum emission level, hence the Sun seems to be a star with an activity level below average. This is also apparent from Fig. 1.3.
Another indication of the connection between magnetic activity and X-ray luminosity has been found by Güdel *et al.* (1997). They measured luminosities with the ASCA and ROSAT satellites for a sample of nine solar-like G stars, which are ostensibly single with ages ranging from 70 Myr to 9 Gyr. They find X-ray luminosities ranging from 1 to 500 times that of the quiet Sun. Their spectra were reduced and analyzed using the XSPEC software (Arnaud

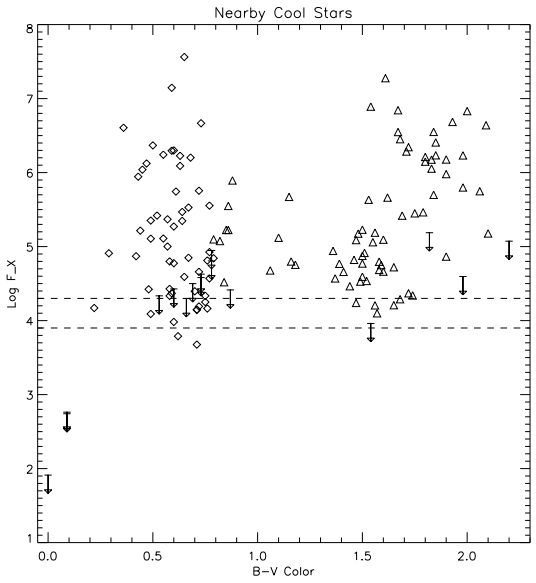

Figure 1.3: *Volume limited complete sample of nearby ($d < 13$ pc) cool stars, with mean X-ray surface brightness F_X vs. $B - V$ color (cf. Schmitt 1997). F and G type stars are plotted as diamonds, K and M ($d < 13$ pc) type stars as triangles (cf. Schmitt et al. 1995), and A type stars as upper limits. For comparison the typical X-ray surface flux level (in the* ROSAT *PSPC band pass) from solar coronal holes is shown by the two dashed lines. Clearly the observed solar coronal hole surface flux provides a good description of the observed stellar minimum X-ray surface flux.*

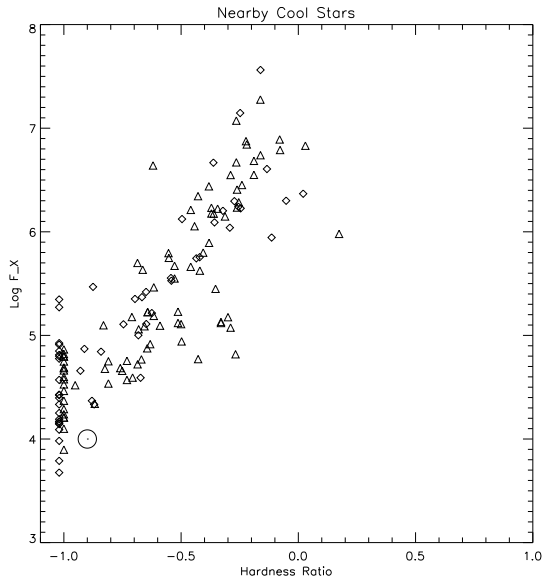

Figure 1.4: *Plot of X-ray surface brightness F_X vs. spectral hardness* HR=(H-S)/(H+S) *between soft* (S) *and hard* (H) ROSAT *PSPC counts for nearby F and G ($d < 13$ pc) stars (diamonds) and K and M ($d < 7$ pc) stars (triangles). The correlation between hardness and total X-ray output is obvious, but a large scatter around the regression curve is also apparent. A typical value in terms of F_X and HR for a solar coronal hole is also shown (⊙). (Taken from Schmitt 1997)*

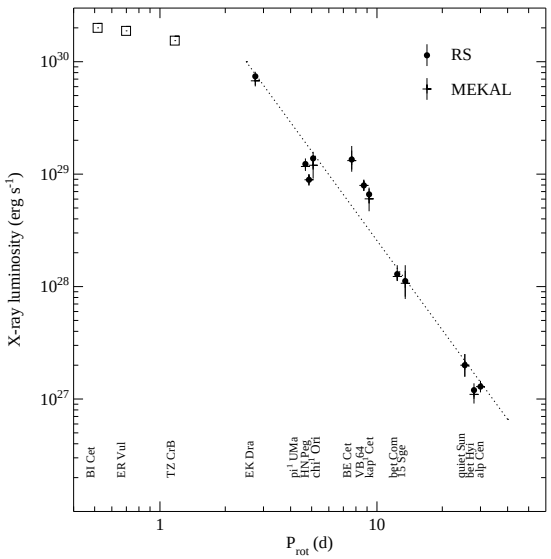

Figure 1.5: *X-ray luminosities, as measured by Güdel et al. (1997) vs. rotational period for the RS code (Raymond & Smith 1977) and the MEKAL code (Mewe et al. 1995). A convincing trend was found.*

1996) package, applying the Raymond-Smith code (Raymond & Smith 1977) in comparison with the MEKAL code (Mewe *et al.* 1995) in order to obtain three-temperature fits. Luminosities were calculated by integration of the model spectra, and for both codes quite a convincing trend is found (Fig. 1.5), portending high X-ray emission associated with fast rotation, supporting the theory of magnetic activity associated with the X-ray luminosities.

Rudimentary spectroscopic analysis was carried out with *Einstein*, e.g., for Capella. Holt *et al.* (1979) used the solid-state spectrometer (SSS) on board the *Einstein* observatory, and performed a two-temperature fit, yielding a best fit for the complete measured spectrum. They used line lists from Raymond & Smith (1977, 1979), and assumed an isothermal source in collisional equilibrium. Elemental abundances were assumed to be solar, except for Mg, Si, S, and Fe, which varied freely in their fitting procedure. They claimed to have identified Mg XI, Si XIII, S XV, and Fe. These so-called global fits are very popular for obtaining useful results from low-resolution spectra, but are occasionally applied to high-resolution spectra as well (e.g., Güdel *et al.* 2001a,b). *Einstein* spectra of Capella with a much better resolution have been obtained by Mewe *et al.* (1982) with the objective grating spectrometer (OGS), covering the range $5-30$ Å with a resolution <1 Å. They also find a bimodal temperature distribution of emission measure, and identify O VIII, Fe XVII, Fe XVIII, Fe XXIV, and Ne X. A spatial distribution of the hot plasma similar to the Sun (Fig. 1.2) is found to be possible for Capella as well. Also the Focal Plane Crystal Spectrometer (FPC) on board *Einstein* has been used to obtain a spectrum of Capella (Vedder & Canizares 1983), and O VIII, Fe XVII, and Fe XX were identified, O VII, however, was not detected. They

found no high temperature component with global fitting because the observed ions are not produced in plasma at temperatures above $\sim$ 20 MK. They also argued that many loops with similar sizes and pressures can produce a nearly isothermal plasma while a second population of longer loops would be required to account for the hotter component.

From the Sun we know that the filling factors (describe percentage of the available volume filled with emitting material) in active regions are small (Acton 1996), e.g., $f = 7\%$, but larger filling factors, i.e., the occupation of larger volumes in stellar coronae, can accommodate the larger observed X-ray outputs. On the other hand, higher electron densities n_e can lead to higher emission measures, which scale with the square of the densities: $EM \sim n_e^2 V$. Estimating the emitting volume $V = 4\pi R^2 f \ell$ with the solar radius R, and a height ℓ proportional to the semi-loop length, a value for $n_e^2 \ell \sim EM$ can be derived. High emission measures can therefore be produced by large semi-loop lengths ℓ, large filling factors f, or by higher densities n_e. Independent measurements of ℓ and f are possible for the Sun, e.g., with TRACE (as in Fig. 1.2) but not for other stars. Density measurements, however, can be performed by means of spectroscopy, paving the way to a better understanding which option nature chooses.

Most of these X-ray data were only broad band data and permitted only very crude spectral diagnostics. Higher spectral resolution data were obtained in the extreme ultraviolet band ($\lambda > 90$ Å) with the EUVE satellite (1992) ($\lambda/\Delta\lambda \sim 100$). But because of the small effective area of its spectrometers only the very strongest sources could be studied (cf. Schmitt *et al.* 1994, Schmitt *et al.* 1996a, Schmitt *et al.* 1996b). Only recently, high-resolution X-ray spectroscopy has become possible with the grating spectrometers on board *Chandra* (LETGS, HETGS) and XMM-Newton (RGS), opening a next phase of investigation of physical properties of stellar coronae by means of spectroscopy. The spectral resolution is typically $\lambda/\Delta\lambda \sim 200 - 500$ depending on the instrument and wavelength of interest. At such resolution individual lines can be identified and line ratios can be computed. However, the spectral resolution is insufficient to measure Doppler shifts and line profiles when line broadening is less than ~ 500 km/s. My PhD thesis is based on data obtained with the *Chandra* observatory, and I will give a detailed summary of the properties of the instruments on board *Chandra* with a special focus on the LETGS (Sect. 1.3.2). Especially, independent density measurements have become available and are for the first time applied to stellar coronae, enabling us to decide whether higher densities or larger filling factors lead to the higher emission measure in stellar coronae compared with the Sun. Therefore, I describe the atomic physics required for a complete understanding of the independent density diagnostics in Sect. 1.4.

1.3 The instrument

1.3.1 The *Chandra* X-Ray Observatory (CXO)

The *Chandra* X-ray Observatory (CXO) is the U.S. follow-up to the *Einstein* Observatory. *Chandra* was formerly known as AXAF, the Advanced X-ray Astrophysics Facility, but renamed by NASA in December 1998 honoring the Indian astrophysicist Subrahmanyan Chandrasekhar (1910–1995). Originally three instruments and a high-resolution mirror assembly consisting of six nested concentric mirror shells in one spacecraft were planned, but the project was reworked in 1992 and 1993. The *Chandra* spacecraft carries now a high-resolution mirror assembly consisting of four shells, two imaging detectors, and two sets of transmission gratings. Important *Chandra* features are: high spatial resolution, good sensitivity from 0.1 to 10 keV, and the capability for high spectral resolution observations over most of this range. *Chandra* is in an elliptical high-earth orbit allowing uninterrupted observing intervals of more than 48 hours.

Table 1.1: *Summary of the telescope mirrors used in various X-ray missions.*

X-ray Telescope Mirrors						
Mirror Characteristic	Einstein	EXOSAT	ROSAT	BBXRT/ASCA	Chandra	XMM
aperture diameter	58 cm	28 cm	83 cm	40 cm one module	1.2 m	70 cm one module
mirrors	4 nested one module	2 nested	4 nested	118 nested one module	4 nested	58 nested
geometric area	350	80	1140	1400 two modules	1100	6000 three modules
grazing angles (arcmin)	40-70	90-110	83-135	21-45	27-51	18-40
focal length (m)	3.45	1.09	2.4	3.8	10	7.5
mirror coating	Ni	Au	Au	Au	Ir	Au
highest energy focused (keV)	5	2	2	12	10	10
on axis resolution (arcsec)	4	18	4	75	0.5	20

A summary of a number of other X-ray missions is given in Tab. 1.1. As can be seen the major improvement is the excellent spatial resolution with a large aperture diameter. Concerning the geometrical area, XMM is certainly superior, while *Chandra* is rather comparable with ROSAT in this respect.

The X-ray Optics

The heart of the observatory is, of course, the X-ray telescope. X-rays can be focused only by means of grazing-incidence where the angle between the incident ray and the reflecting surface is less than a critical angle. This critical grazing angle is approximately $10^{-2}(2\rho)^{1/2}/\mathrm{E}$, where ρ is the density in g/cm^3 and E is the photon energy in keV. Thus, higher energy telescopes must have dense optical coatings (iridium, platinum, gold, etc.) and small incidence angles. The X-ray optical elements for *Chandra* and similar telescopes resemble shallow angle cones, and two reflections are required to provide good imaging over a useful field of view. The first CXO surface is a paraboloid and the second a hyperboloid – the classic Wolter-1 design. Hans Wolter developed this system in 1951 for X-ray microscopy in Kiel. The collecting area is increased by nesting concentric mirror pairs, all having the same focal length. The wall thickness of the inner elements limits the number of pairs, and designs have tended to fall into two classes: Those with relatively thick walls achieve stability, hence angular resolution, at the expense of collecting area; those with very thin walls maximize collecting area but sacrifice angular resolution. NASA's *Einstein* Observatory (1978), the German, US ROSAT (1990), and the CXO optics are examples of the high-resolution designs, while the Japanese-American ASCA (1993) and European XMM mirrors are examples of emphasis upon large collecting area.

The mirror design for CXO includes eight optical elements comprising four paraboloid/hyperboloid pairs which have a common ten-meter focal length, element lengths of 0.83 m, diameters of 0.63, 0.85, 0.97, and 1.2 m, and wall thicknesses between 16 mm and 24 mm. Zerodur, a glassy ceramic from Schott, was selected for the mirrors because of its low coefficient of thermal expansion and previously demonstrated capability (ROSAT) of permitting very smoothly polished surfaces. Originally, six mirrors were planned, but only four were realized due to reduction of funds.
X-ray testing demonstrated that the CXO mirrors are indeed the largest high-resolution X-ray optics ever made; the nominal effective area (based on the ground calibrations) is shown as a function of energy in the left panel of Fig. 1.6, in comparison with those of the *Einstein* and ROSAT predecessors. The CXO effective area is about a factor of four greater than that of *Einstein*. The effective areas of CXO and ROSAT are comparable at low energies, because the somewhat smaller ROSAT mirrors have larger incidence angles; the smaller incidence angles of CXO yield more throughput at higher energies. The fraction of the incident energy included in the core of the expected CXO response to 1.49 keV X-rays (point source) is shown as a function of image radius in the right panel of Fig. 1.6 including early in-flight data. The responses of the *Einstein* and ROSAT mirrors also are shown. The improvement within $0.5''$ is dramatic, although it is important to note that the ROSAT mirrors surpassed their specification and were well matched to the principal detector for that mission.

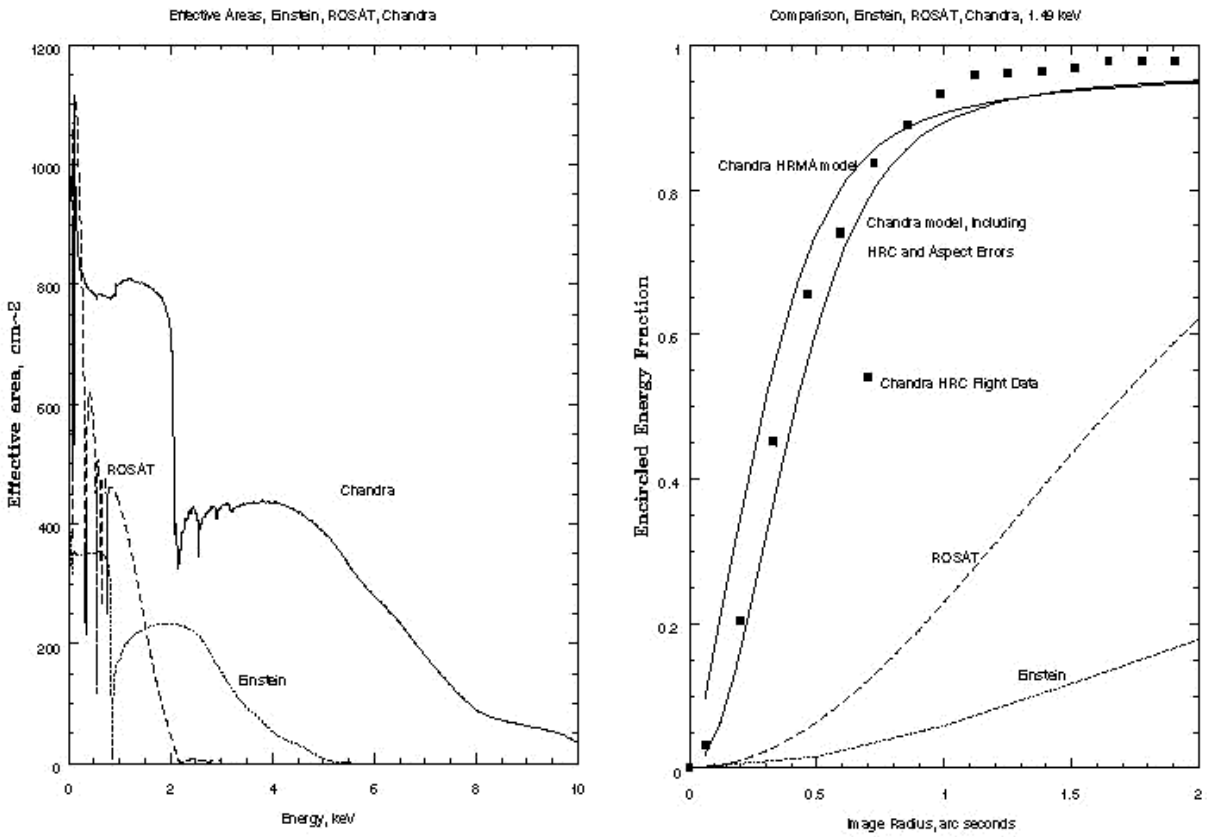

Figure 1.6: *Comparison between Chandra,* ROSAT, *and Einstein. Left panel: Nominal effective areas for the telescopes. Right panel: encircled energy fraction at 1.49 keV.*

The Instrumentation

CXO has two focal plane instruments – the High-Resolution Camera (HRC-I and HRC-S for imaging and spectroscopy) and the Advanced CCD Imaging Spectrometer (ACIS-I and ACIS-S). Each of these instruments has two detectors, one optimized for imaging of X-rays that pass directly through the optics and the other optimized for imaging X-rays that are dispersed by the objective transmission gratings when the latter are commanded into place directly behind the HRMA (High Resolution Mirror Assembly). Each focal-plane detector operates essentially in photon counting mode and has low internal background. A slide mechanism is utilized to place the appropriate instrument into the focus of the telescope. Provision for focus adjustment is also present.

The Focal Plane Instruments (Detectors)

The High Resolution Camera HRC was built at the Smithsonian Astrophysical Observatory in Cambridge, MA (SAO), and the PI is Dr. S. Murray. The HRC-I (imaging mode) is a large-format 100-mm-square microchannel plate coated with a cesium iodide photocathode to improve X-ray response. A conventional cross-grid charge detector reads out the photo-induced charge cloud and the electronics can determine the arrival time as accurate as 16 μs, and the position with a resolution of about 18 μm or 0.37″. The spectroscopy readout detector (HRC-S) is a 300 mm×30 mm, 3-section microchannel plate (MCP) (cf. Fig. 1.10). Sectioning allowed the two outside sections to be

tilted in order to conform more closely to the Rowland circle that includes the low-energy gratings (cf. Fig. 1.7).

The ACIS is built by the Massachusetts In-

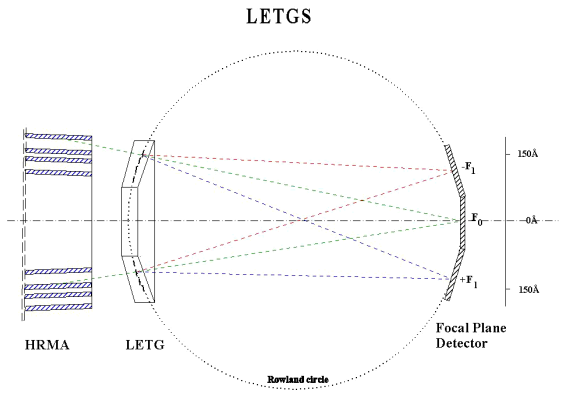

Figure 1.7: *Construction of the observatory in spectroscopic mode. The X-ray light is focused by the four mirrors (left), and is dispersed by the transmission grating. The detector is placed in the focal plane.*

stitute of Technology's Center for Space Research in collaboration with Lincoln Laboratories with Prof. G. Garmire of the Pennsylvania State University as the Principal Investigator. Lockheed-Martin integrated the instrument. It has two charge coupled-device (CCD) detector arrays: ACIS-I is optimized for high-resolution spectrometric imaging, and ACIS-S is optimized for readout of the high-energy transmission gratings, although these functions are not mutually exclusive. The ACIS-I is a 2×2 array of CCDs. The 4 CCDs tilt slightly toward the optics to match the focal surface more closely. Each CCD has 1024×1024 pixels of 24 μm (0.5″) size. The ACIS-S is a 1×6 array with each chip tilted slightly to match the Rowland circle and includes two back-illuminated CCDs, one of which is at the best focus position. The back-illuminated devices cover a broader bandwidth than the front-illuminated chips and, under certain circumstances, may be the best choice for high-resolution, spectrometric imaging.

The Transmission Gratings

Both sets of objective transmission gratings consist of hundreds of co-aligned facets mounted to supporting structures on 4 annuli (one for each of the four co-aligned mirror pairs) to intercept the X-rays exiting the HRMA. In order to optimize the energy resolution, the grating support structure holds the facets close to the Rowland toroid that intercepts the focal plane. The Low Energy Transmission grating is shown in Fig. 1.9. The High Energy Transmission Grating (HETGS) looks very much the same with the inner two rings assigned to the High Energy Grating (HEG) and the outer two rings the Medium Energy Grating (MEG).

The High-Energy Transmission Grating (HETG) provides high-resolution spectroscopy at the higher end of the CXO energy range. Prof. C. Canizares of the Massachusetts Institute of Technology Center for Space Research is the Principal Investigator. This group developed the instrument in collaboration with MIT's Nanostructures Laboratory. The HETG has 336 2.5 cm square grating facets. The HETG uses gratings with two different periods which are oriented to slightly different dispersion directions, forming a shallow "X" image on the readout detector. The inner two rings of the support structure are the high-energy grating facets, and the outer two rings are the medium-energy grating facets. The ACIS-S is the primary readout for the HETG.

A detailed description of the LETGS is given in Sect. 1.3.2.

The effective areas for the CXO gratings are presented in Fig. 1.8 in comparison with the Reflection Grating Spectrometer (RGS) onboard XMM and the spectral ranges of earlier X-ray missions. As can be seen, the LETGS has the largest wavelength range, comprising the ranges of both ROSAT and *Einstein*, respectively. When transforming total X-ray luminosities L_X for comparison with earlier missions, the spectral range can be adapted to the spectral ranges of, e.g., ROSAT or *Einstein* without the need of any model.

The gratings HEG and MEG on board *Chandra* as well as the RGS on board XMM provide large effective areas between 1.2 and 31 Å. With this spectral range the are centered on wavelengths containing the L-shell lines from ionization stages of Fe XVII to Fe XXIV and the K-shell lines of hydrogenic and helium-like ions of oxygen through nickel. The decline of effective area is quite dramatic for the HEG and the MEG at wavelengths above 17 Å.

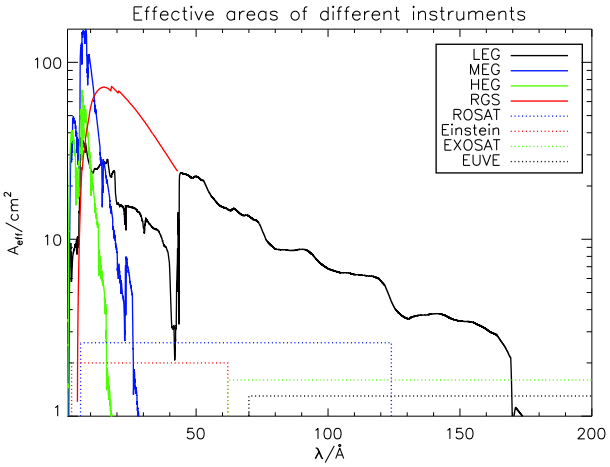

Figure 1.8: *Effective areas for the gratings onboard Chandra in comparison with RGS onboard XMM, and earlier missions (only spectral ranges).*

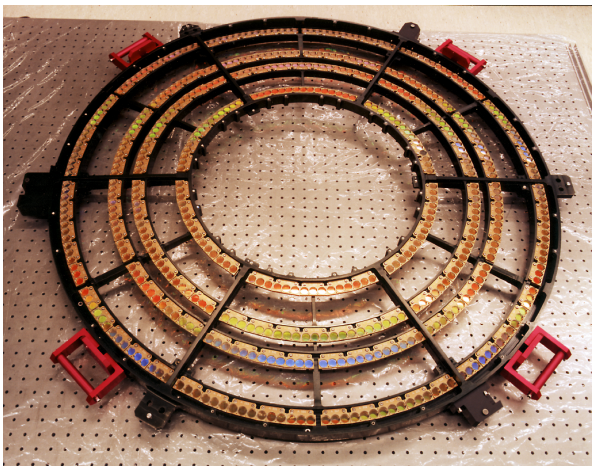

Figure 1.9: *The Low Energy Transmission Grating was designed, tested, and adjusted by MPE, Garching. The assembly of the grating elements was built by the company of Heidenhain at Traunreut. 540 single grating facets are mounted on a ring shaped frame with very high precision. During the mission the whole grating ring can be switched into the beam path of the telescope to perform spectroscopy. The diffractive effect of the grating can be seen in the optical light by its decomposition in spectral colors.*

1.3.2 The Low Energy Transmission Grating Spectrometer (LETGS)

The Low-Energy Transmission Grating (LETG) provides high-resolution spectroscopy at the lower end of the CXO energy range. Dr. A. Brinkman of the "Space Research Organization of the Netherlands" (SRON) is the Principal Investigator. The LETG was developed in collaboration with the Max Planck Institut für Extraterrestrische Physik, Garching (Dr. P. Predehl). The LETG has 540 1.6 cm diameter grating facets, three per grating module. Ultraviolet contact lithography was used to produce an integrated all-gold facet bonded to a stainless-steel facet ring. An individual facet has 0.43 μm-thick gold grating bars with 50% filling factor and 9920 Å period, resulting in 1.15 Å/mm dispersion. The HRC-S is the primary LETG readout detector.

As can be seen from Fig. 1.9, a ring-like frame is used as a support structure for the grating facets. This ring can be inserted into the beam in a way that one ring will be directly behind each mirror. It can be seen that originally six mirrors were planned, but only four were realized due to limited funds. The construction is shown in Fig. 1.7. The X-ray light, focused by the mirrors (High Resolution Mirror Assembly HRMA), is dispersed in transmission. The detector (HRC) is divided into three segments in order to account for the focal plane to be a section of a circle, the Rowland circle. The gaps between the segments cannot be used for analysis, and in order not to loose the same part of the spectrum on both sides of the detector. The 0^{th} order is shifted off center, so the con-

struction is not completely symmetrical. An extra benefit from this asymmetric construction is that the wavelength range covered by the LETGS is a little bit larger on one side of the detector.

1.3.2.1 Obtaining Spectra from the HRC

The High Resolution Camera HRC

The HRC is a microchannel plate (MCP) detector with high spatial resolution but low energy resolution. It has a large field of view and is useful for imaging large objects (e.g., galaxies, supernova remnants, clusters of galaxies), or a large region of the sky with high resolution. In spectroscopy mode the HRC-S is used to collect the dispersed spectrum from the LETGS. The ACIS can also be used but is less sensitive and yields a smaller wavelength range. But the higher intrinsic energy resolution allows for disentangling higher dispersion orders from the first dispersion order, which is not possible with the HRC-S.
Fig. 1.10 shows the focal plane layout of the HRC. HRC-I (imaging mode) has its maximum linear dimension along the dispersion direction of the Low Energy Transmission Grating (LETG), for which it is the backup readout. HRC-S consists of three separate 100 mm × 27 mm segments. The outer two segments are tilted toward the HRMA in order to approximately match the LETG Rowland surface. UV/Ion shields (to block UV and low energy ions) consisting of aluminized polyamide are shown in Fig. 1.10.

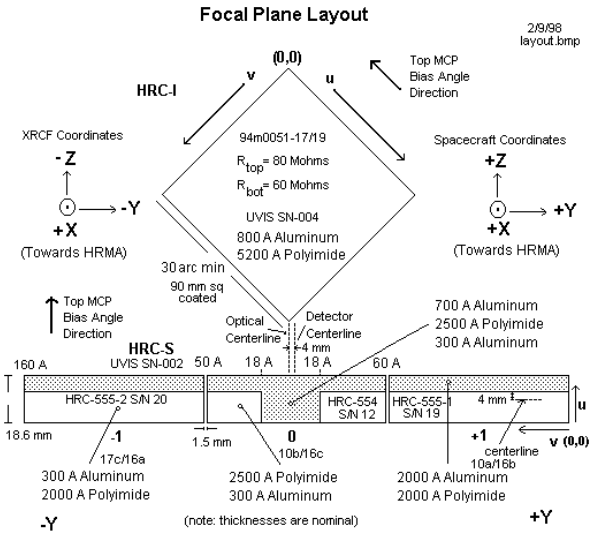

Figure 1.10: *Sketch of the High Resolution Camera HRC*

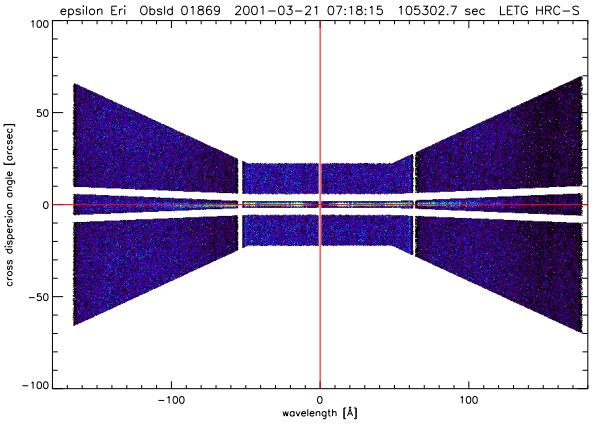

Figure 1.11: *X-ray Image of ϵ Eri obtained by the HRC-S with the LETGS as grating. Only the extraction regions containing the spectral trace (middle) and adjacent regions for obtaining the instrumental background are shown.*

The extraction procedure using the HRC-S

Due to the limited intrinsic energy resolution of the MCP the spectra are obtained exclusively from the spatial distance along the dispersion direction between individual photons encountered and the 0^{th} order. The procedure is demonstrated in Fig. 1.11. Shown are only the parts of the image used for the extraction, consisting of three horizontal extraction regions associated with the spectral trace and the adjacent instrumental background. The shapes of the extraction regions are optimized in order to collect as many source photons as possible while keeping the background as low as possible. The extraction regions are inter-

rupted by the 0^{th} order, which is marked by the thin vertical line at 0 Å, and the gaps between the microchannel plates, where no photons can be extracted. Negative wavelength values indicate the spectrum associated with the left dispersion direction, which should be symmetrical to the positive wavelength scale. However, left and right sides are treated separately during the extraction. The spectral trace is in the middle horizontal stripe, within which the source photons are collected. The regions associated with the background are scaled in a way that the area is always a factor ten larger than the corresponding area for the spectral trace. As can be seen in Fig. 1.11, the gaps are not at the same distance from the center, which is intended for retaining the chance to measure what is lost on the respective other side of the detector. Along the dispersion direction the image is divided into bins, which can be converted into a wavelength scale by using the distance from the 0^{th} order and the lattice parameter of the grating. The number of pixels included in cross dispersion direction is optimized for collecting as many source counts as possible while keeping the background as low as possible. The number of photons for each bin returns a count spectrum. Since the point spread function becomes broader near the edge of the detector, larger areas for photon counting are necessary there, in order not to loose too many source counts spread outside the defined extraction region. As can be seen in Fig. 1.11, the same spectrum should be measured on both sides of the 0^{th} order, such that, ideally, the two spectra can be co-added, in order to increase the signal to noise ratio (S/N). This is justified at least for the central segment for wavelengths up to $\sim$ 50 Å shown by Ness *et al.* 2001a (cf. Chapter 3). For this, individual lines are measured on both sides separately, and their measured wavelengths are compared. The differences are smaller than the average line width, and the calibration is therefore sufficient for co-adding both spectra without loosing resolution. However, one can always measure on both sides separately, if ambigous spectral features provoke suspicion of malicious co-adding.

1.4 Analysis

Since the methods are only briefly described in the papers, a detailed description of the methods applied in order to obtain densities and temperatures is given in this section.

1.4.1 Atomic physics of He-like ions

In general, spectroscopic density measurements rely on processes that depend on collisional (de-)excitations. The coronal plasma can be considered a collisional plasma, i.e., all excitations are induced by collisions. This is justified from, e.g., the low optical depths (cf. Sect. 1.4.4). Radiative de-excitations of the excited states are related with very much different time scales $\tau_{\rm rad}$. Resonance lines are permitted transitions with small time scales $\tau_{\rm rad}$, while, e.g., intercombination lines with changes of the multiplicity are forbidden, i.e., have very low transition probabilities and thus comparably long time scales $\tau_{\rm rad}$. However, these time scales are all much smaller than typical time scales for collisions $\tau_{\rm col}$, when considering the low densities in coronal plasmas. Excited states which can only return to the ground level via a forbidden transition can thus be de-populated by this radiative transition. In coronal plasmas with higher densities, the time scales for collisions $\tau_{\rm col}$ will become smaller, such that for forbidden transitions they can become comparable to the radiative time scale ($\tau_{\rm rad} \approx \tau_{\rm col}$). A density dependent balance of radiative transitions and excitations by collisions into higher excited states is reached. The forbidden transition is favoured in a plasma with a low density, while the latter process is more likely in a high-density plasma, which allows for a higher frequency of collisions. The He-like triplets consist of a resonance line, an intercombination line, and a forbidden line. The time scales for radiative decay $\tau_{\rm rad}$ are different for the intercombination line and the

forbidden line, yielding a higher value for the forbidden line. Therefore the ratio of these two lines is density sensitive in low density plasmas, where the intercombination line can be considered a permitted line in comparison with the forbidden line. The naming convention abbreviates the resonance line with an r, the intercombination line with i, and the other forbidden line with an f.

The theory of the atomic physics of He-like triplets has been developed by Gabriel & Jordan (1969) and refined by, e.g., Blumenthal *et al.* (1972), Mewe & Schrijver (1978), Pradhan & Shull (1981), Pradhan *et al.* (1981), Pradhan (1982), Pradhan (1985), and recently Porquet *et al.* (2001). The term diagram and a typical spectrum referring to the term diagram are shown in Figs. 1 and 2 of Sect. 7. Basically, the excited states 1s2l (l is either s or p) split up into the terms 1s2p ^{1}P$_1$, 1s2p ^{3}P$_{0,1,2}$, 1s2s ^{3}S$_1$, and 1s2s ^{1}S$_0$ out of which the levels with J $\neq 0$ decay to the ground state 1s^2 ^{1}S$_0$ through the resonance line r, the intercombination line i, and the forbidden line f, respectively; the latter two lines involve spin changes and therefore violate the selection rules for electric dipole radiation. Although the radiative transition rate for the forbidden line is quite small, the excited 2 ^{3}S$_1$ state does still decay radiatively in a low-density plasma, because collisional depopulation processes are very rare. In a high-density plasma collisional de-excitations dominate and hence the forbidden line disappears. Since these de-excitations will populate the level 2 ^{3}P the intercombination line will become stronger while the forbidden line will become weaker, such that the ratio of f/i is smaller in high-density plasmas. The range of densities measurable by this method is limited by the low-density limit at which collisions are too rare to de-populate the level 2 ^{3}S (associated with the forbidden line) and the high-density limit at which also the level 2 ^{3}P (associated with the intercombination line) will be de-populated by collisions before it can decay radiatively. Complications arise from other competing processes populating and depopulating the ^{3}P and ^{3}S levels. These are in particular radiative transitions induced by, e.g., the underlying photospheric stellar radiation field (discussed in Sect. 1.4.1.1) as well as ionization and recombination processes from the Li-like and H-like ions, respectively. Basically the first effect ist most severe for He-like ions in low ionization stages, while the latter affects more the highly ionized ions. It is customary to describe the measured line intensities r, i, and f in terms of the ratios

$$R_{\rm obs} = \frac{\rm f}{\rm i} \quad \text{and} \quad G_{\rm obs} = \frac{\rm i + f}{\rm r}\,. \qquad (1.1)$$

In this work the notation of, e.g., Pradhan & Shull (1981) is used. In other contexts (e.g., calculating ions of higher ionization stages) a different notation labeling r as **w**, f as **z**, and i as **x**+**y** is often used pointing out that the intercombination line consists of two transitions, ^{3}P$_{1,2} \rightarrow ^1$S$_0$, also called M2 and E1 transitions, which cannot be resolved. Theory describes the density sensitivity of the R ratio by the functional dependence

$$R(n_e) \;=\; R_0 \frac{1}{1 + \phi/\phi_{\rm c} + n_e/N_{\rm c}} \qquad (1.2)$$

(Gabriel & Jordan 1969), where R_0 is the low-density limit, $\phi/\phi_{\rm c}$ describes the influence of external radiation fields, and $n_e/N_{\rm c}$ represents the influence of (density-dependent) collisional excitations. Electron densities n_e are inferred from equating $R(n_e)$ with $R_{\rm obs}$. The so-called low-density limit R_0 can be considered the ratio of excitation probabilities, applies for $n_e = 0$ and $\phi = 0$ in Eq. 1.2, and is given by

$$R_0 = \frac{1+F}{B} - 1 \qquad (1.3)$$

(Blumenthal *et al.* 1972), where B is the radiative branching parameter averaged over the two components of the intercombination line and F is the ratio of the collision rates from the ground to the levels 2 ^{3}S and 2 ^{3}P, respectively (including cascade effects from upper levels through radiative transitions after excitation or recombination). The parameter $N_{\rm c}$ is the so-called critical density (cf. Tab. 1.2), at which

the observed line ratio is density-sensitive, and is given by

$$N_{\rm c} = \frac{A(2\,^3{\rm S}_1 \rightarrow\ 1\,^1{\rm S}_0)}{(1+F)C(2\,^3{\rm S}_1 \rightarrow\ 2\,^3{\rm P})}\,, \qquad (1.4)$$

where $A(2\,^3{\rm S}_1 \rightarrow\ 1\,^1{\rm S}_0)$ is the radiative transition probability of the forbidden line, $C(2\,^3{\rm S}_1 \rightarrow\ 2\,^3{\rm P})$ is the electron collisional rate coefficient for the transition from $2\,^3$S to $2\,^3$P, and F as in Eq. 1.3. Finally, the parameters ϕ (the radiative absorption rate from $2\,^3$S to $2\,^3$P induced by an external radiation field) and $\phi_{\rm c}$ describe the additional possible influence of the stellar radiation field on the depopulation of the ^{3}S state (cf. Sect. 1.4.1.1). The latter is insignificant for the He-like triplets of higher ionization stages, but can have a large impact on low-Z ions, as C V or N VI. But it is found that in some cases the influence can be significant for O VII and even for Ne IX as well. Values for R_0 and $N_{\rm c}$ are listed in Tab. 1.2. As can be seen, a large temperature range can be probed with the different He-like ions. While lower temperature plasmas can be probed in the density range around $10^9\,{\rm cm}^{-3}$, the high temperature ions Si and Mg are only sensitive at very high densities above $10^{12}\,{\rm cm}^{-3}$. The ratio G=(i+f)/r, a measure of the relative strength of the resonance line, depends on the electron temperature $T_{\rm e}$ (e.g., Porquet *et al.* 2001). G can be used to derive temperatures for the lines used for density diagnostics that can be compared with the maximum formation temperature $T_{\rm m}$.

Table 1.2: *Atomic Parameters for He-like triplets. $T_{\rm m}$ is the peak line formation temperature (MEKAL), R_0 is the low-density limit and $N_{\rm c}$ the density where R falls to half its low-density value (Pradhan & Shull 1981).*

ion	$T_{\rm m}$/MK	R_0	$N_{\rm c}/(10^{10} cm^{-3})$
C V	1	10.6	0.051
N VI	1.4	4.9	0.45
O VII	2.2	3.95	3.00
Ne IX	4.0	3.5	59.0
Mg XI	6.3	2.6	620
Si XIII	10.0	2.67	3090

1.4.1.1 Influence of radiation fields on the density diagnostics with He-like triplets

The method of He-like triplets has been applied in the seventies and eighties for density diagnostics of the solar corona quite extensively. The consideration of external radiation fields was only important for C V regarding the temperature of the solar photosphere, hence was commonly considered negligible. The application of this method has become available for other stars with the advent of the high resolution spectrometers on board *Chandra* and XMM, capable of measuring individual emission lines. The investigation of densities in the coronal plasmas of other stars requires rethinking this issue, since not only different coronal properties will be encountered, but also different photospheric conditions. When regarding an F star like Procyon, a comparably inactive corona stands in contrast to a warmer photosphere, and the strong external radiation field cannot be neglected as in the case of the Sun. In the Algol system, a binary consisting of a K star bearing a very active corona and a B star which can be considered X-ray dark, the external radiation field originating from the companion B star is worth investigating. These two examples are discussed in Chapter 5. Surprisingly, the radiation field has non-negligible effects on the density diagnostics up to O VII, and even for Ne IX the effect is noticeable in spite of the distance of this source and the dilution of the radiation. This effect is estimated by a dilution factor

$$W = \frac{1}{2}\left[1 - \left\{1 - \left(\frac{r_\star}{a}\right)^2\right\}^{1/2}\right] \qquad (1.5)$$

(Mewe & Schrijver 1978) where $r_\star$ is the extent of the radiation source (e.g., the stellar

radius) and a is the distance between the radiation source and the plasma under investigation. Normally the surface of the star itself is the dominant radiation source, and in these cases $a = r_\star$, i.e., $W = 1/2$, is used.
In order to estimate the contribution of the radiation field to the line ratio f/i, described by the term ϕ/ϕ_c in Eq. 1.2, measurements of the flux at the respective wavelengths for the transition f→i must be carried out. The wavelengths at which the radiation must be measured depend on the He-like ions because the energies in the term diagram depend on the potential of the nucleus. From the energy difference of the levels i and f the wavelengths can be calculated, and they all lie in the ultraviolet range. Appropriate missions for these kinds of measurements are, e.g., the IUE (International Ultraviolet Explorer) mission or the new Hubble STIS instrument. The fluxes obtained from these missions can be converted to intensities, which can be compared with Planck curves in order to obtain the radiation temperatures. The correct Planck curve will be used to estimate the term ϕ/ϕ_c. The details of this procedure using IUE data are described in Chapter 3 (Ness *et al.* 2001a), Chapter 6 (Ness *et al.* 2001c), and Chapter 7 (Ness *et al.* 2001d).

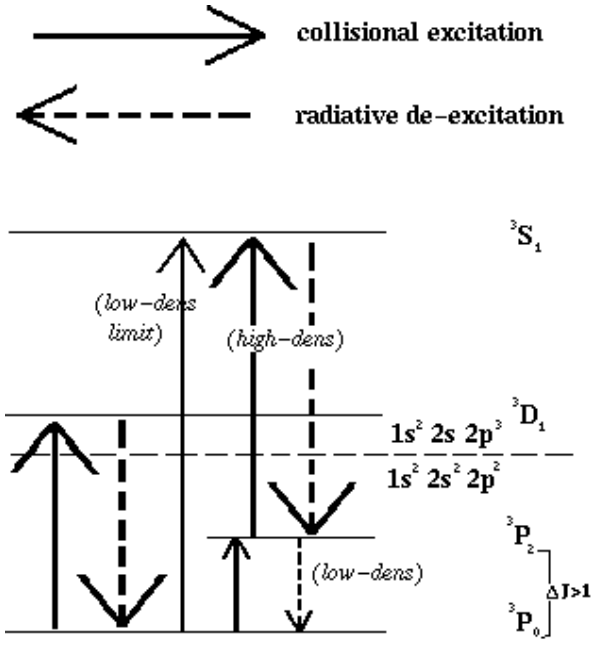

Figure 1.12: *Term diagram of Fe XXI. The excited level $2s2p^3\,{}^3S_1$ can be populated from the ground level states $2s^22p^2\,{}^3P_0$ and ${}^3P_2$. Since the transition ${}^3P_2$–${}^3P_0$ is forbidden ($\Delta J > 1$), it can decay radiatively only in low-density plasmas, while in high density plasmas, the collisional excitation into the excited level $2s2p^3\,{}^3S_1$ will be preferred. The electron collision strength for ${}^3P_0$–${}^3S_1$ is very small in comparison with ${}^3P_2$–${}^3S_1$, such that the line corresponding to the transition ${}^3S_1$–${}^3P_2$ is strong only in high density-plasmas.*

1.4.2 Density diagnostics with Fe XXI line ratios

In addition to He-like ions, ions with more than two electrons can be used as a density diagnostic. Line ratios of Fe XXI can be used as density diagnostics for plasmas with electron densities in the range of $10^{11} - 10^{14}\,\mathrm{cm}^{-3}$ since the populations of the ground configuration ($1s^22s^22p^2$) levels vary with n_e (Mason *et al.* 1979). The ground configuration of Fe XXI $1s^22s^22p^2$ splits up into ${}^3P$, ${}^1D$, ${}^1S$. The energy difference between the ground state ${}^3P_0$ and the excited levels ${}^3P_1$ and ${}^3P_2$ is 9 eV and 14.5 eV, respectively, and 30 eV between ground state and ${}^1D_2$. In low-density plasmas virtually all atoms are in the ground state ${}^3P_0$, while in high-density plasmas the occupation of excited levels can be described by Boltzmann statistics. Consequently, from excited levels certain lines will appear only in high-density plasmas. In contrast to He-like lines the appearance of certain lines is an indicator of high-density plasmas.
Generally, in a low-density plasma ($n_e < 10^{13}\,\mathrm{cm}^{-3}$), the strongest line produced by Fe XXI and measurable with the LETGS is the transition $2s^22p^2\,{}^3P_0$–$2s2p^3\,{}^3D_1$ at 128.73 Å, which is measured in virtually all active stars. At higher densities ($n_e > 10^{11}\,\mathrm{cm}^{-3}$), e.g., the level $2s2p^3\,{}^3S_1$ will be populated from the

$2s^22p^2$ ground state $^3P_2$, which in low-density plasmas can decay radiatively via the forbidden transition to the ground state $^3P_0$ (cf. Fig. 1.12), before the collisional excitation into $^3S_1$ can take place. Therefore, in the high-density case, the long time scale for the radiative decay of the forbidden transition $^3P_2$–$^3P_0$ gives rise to the population of $^3S_1$ level. Similar transitions between excited states $2s2p^3$ and the ground state $2s^22p^2$ are density sensitive (Mason *et al.* 1979), and wavelengths are 97.9 Å ($^3S_1$–$^3P_1$), 102.2 Å ($^3S_1$–$^3P_2$), 117.5 Å ($^3P_1$–$^3P_1$), and 121.2 Å ($^3P_2$–$^3P_2$), which can be measured with the LETGS, and line fluxes with respect to the 128.73 Å line can be calculated. Observationally, the 128.73 Å line always seems to be the strongest Fe XXI line, suggesting that coronal densities ought not to exceed $n_e \sim 10^{13}\,\mathrm{cm}^{-3}$, and the other Fe XXI lines are weaker, and it is not always clear that they have been clearly detected.
Measured flux ratios can be compared with theoretical flux ratios, obtained, e.g., with the line data base Chianti (Dere *et al.* 2001) or from Brickhouse *et al.* (1995). The theoretical flux ratio vs. n_e curves are very flat for low densities and start to deviate from the low-density plasma situation only for values of $n_e > 10^{11}\,\mathrm{cm}^{-3}$. This makes the method insensitive for the lower limit. However, this low-density limit lies much lower than the low-density limit of Si XIII, which is formed at similar temperatures. The method with Fe XXI line ratios is therefore better suited for measuring lower densities at high temperature, while the Si and Mg triplets can only be used for high-density plasmas at high temperatures.

1.4.3 Measuring plasma temperatures with line ratios

Plasma temperatures can be derived quite easily from ratios of emission lines emitted by elements in different ionization stages, e.g., O VIII and O VII. The measured ratio is compared with the temperature dependent ratio of the cooling functions for the corresponding ions, which can be taken from theoretical line data, e.g., MEKAL (Mewe *et al.* 1995), SPEX (Kaastra *et al.* 1996), or Chianti (Dere *et al.* 2001). The point of this method is that the cooling function of the ion in the lower ionization stage is shifted towards lower temperatures in comparison with the higher ionization stage, so a strong dependence with the temperature is found. Using ions from the same element makes this method independent of elemental abundances.
The temperature dependence of the so-called He-like G ratio can also be used for measurements of plasma temperatures. The advantage of this method is that it is not only independent of abundance effects but measures the temperature within the same plasma region, while the method of using line ratios of different ionization stages is only an average over hotter and cooler regions. In many cases, however, the G-ratio is not temperature sensitive for the temperatures to be measured.

1.4.4 Optical depth effects

The general assumption underlying the analysis of coronal plasmas is that the plasma is optically thin, i.e., no radiative scattering takes place. With this assumption the atomic data, which are always calculated for optically thin plasmas, can be used without any correction. Otherwise, line fluxes from resonance lines must be considered to be reduced , thus underestimated, since absorbed photons are lost (except for the small fraction re-emitted into the direction of the observer). An estimate of optical thickness can be obtained by comparing resonance lines with large oscillator strengths f with lines with small oscillator strengths. A popular example is the strong Fe XVII line at 15 Å ($f = 2.66$) in comparison with an Fe XVII line at 15.27 Å ($f = 0.6$). The theoretically calculated line ratio 15 Å line by 15.27 Å line yields the expected ratio in the case $\tau = 0$, i.e., optically thin plasma, while the measured line ratio must be smaller than this value when

the plasma is not optically thin. The ratio of these two ratios is called the escape factor P of a "homogeneous mixture of emitters and absorbers in a slab geometry" (Kaastra & Mewe 1995, Mewe *et al.* 2001), and can be used to derive the optical depth τ from

$$P(\tau) = [1 + 0.43\tau]^{-1}. \tag{1.6}$$

Significant values for τ can be used for calculating constraints on $n_e\ell$ by use of

$$\tau = 1.2\ 10^{-17} \left(\frac{n_i}{n_{el}}\right) A_z \left(\frac{n_H}{n_e}\right) \lambda\ f \sqrt{\frac{M}{T}} n_e\ell, \tag{1.7}$$

where the fractional ionization is denoted by n_i/n_{el}, the elemental abundances by A_z, the ratio of hydrogen to electron density $n_H/n_e = 0.85$ for typical cosmic plasmas with solar composition, the oscillator strength f for the ion under consideration, the atomic number M, the wavelength λ, measured in Å, the temperature T in K, the electron density n_e in cm^{-3} and the mean free path denoted by ℓ (Schrijver *et al.* 1994). Uncertainties in theoretical atomic data, however, can pose problems, while laboratory measurement (e.g., EBIT; Brown *et al.* 2001) seem to be more reliable (cf. Ness *et al.* 2001e, Chapter 4.7).

1.4.5 Analysis of magnetically confined loops

Investigation of the solar corona revealed that the coronal plasma is confined in loop-like structures. As can be seen from Fig. 1.2 these loops can have different sizes and luminosities. An analysis of the dynamics of the quiescent solar corona was carried out by Rosner *et al.* (1978), and a relation between the maximum temperature, the pressure, and the length of a loop has been found and was successfully tested with data from the S-054 Skylab telescope. They also found that hydrostatic solutions are stable only if the temperature maximum is located at the top of loop structures, and that acoustic mode damping in a coronal heating model is inconsistent with the loop model. Their scaling law reads $T_{\max} \sim 1.4 \times 10^3 (pL)^{1/3}$, and

$$n_e\, L = 1.3 \times 10^6\, T_{\max}^2 \tag{1.8}$$

can be derived using $p \sim 2n_e k T_{\max}^2$ for the pressure p, with $T_{\max}$ the maximum temperature, sometimes also called apex temperature, because of the finding of Rosner *et al.* (1978) that the maximum temperature must be at the peak, or apex, of the loop. n_e is the apex electron density and L the semi-loop length. The loop geometry is considered semi-circular, and generalizations of the basic Eq. 1.8 (also called RTV model) have been developed by Vesecky *et al.* (1979), including cross sections that increase with height in a way representing loop field structures by a magnetic line dipole below the chromosphere. The scaling law is only slightly modified by their results, which can conveniently be approximated by introducing a factor $\Gamma^{-0.1}$ into the scaling law (or $\Gamma^{0.3}$ in Eq. 1.8), describing tapered loops. In the semi-circular geometry, the cross section is constant through the whole loop, but Γ represents the ratio of the loop cross section at the apex to that at the loop foot-point, and is thus an expansion factor with $\Gamma = 1$ for the special case of an RTV model.

1.5 Scope of this work

With the instrument described in Chapter 1.3 and the methods described in Sect. 1.4, coronal densities and temperatures are derived for the well known stars Capella, Procyon, and Algol. A description of the LETG spectrometer on board the *Chandra* telescope has been given in Chapter 1.3. The data obtained with this instrument have been analyzed with a program developed by myself. The background of the development has lead me to the name CORA, which stands for CORonal Activity. A detailed description is given in Chapter 2 in an article to be submitted for publication in the *Astron. Nachr.* The functionality and the comfortable usage have invited a number of other people in the scientific community to use this program.

Table 1.3: *Summary of stellar properties and measurement of X-ray luminosities carried out with the LETGS for the stars analyzed in Chapter 5. Stellar properties are collected from the literature (references given below as indicated by superscripts). ROSAT measurements are taken from, e.g., Hünsch et al. (1998, 1999). All X-ray luminosities L_X are given in units 10^{28} erg/s.*

	Algol	Capella	Procyon	ϵ Eri	α Cen		UX Ari
					A	B	
HD	19356	34029	61421	22049	128620	128621	21242
Spectr. Type	K2IV	G1III+ G8/K0III	F5 IV-V	K2V	G2V	K0V	G5V/K0IV
$R_\star/R_\odot$	3.5[16]	9.2[7]	2.06[10]	0.81[14]	1.23[19]	0.80[19]	0.93/>4.7[20]
v sin$i$ [km/s]	55	5[3]	2.8[5]	1.7[17]	2.7[17]	1.1[17]	6/37[20]
P/days	2.8674[18]	84[12]	19.8[9]	11.1[6]	29[17]	42[17]	6.44[21]
T_{eff}/K	4500[16]	5700[7]	6530[4]	5180[1]	5770[19]	5350[19]	5700/4750[21]
log g	3.2[16]	2.6[11]	4.05[4]	4.75[1]	4.38[2]	4.73[2]	4.27/3.5[21]
d/pc	28[15]	13[20]	3.5	3.22	1.34		50[20]
t_{exp}/ksec	81.4	218.5	140.7	105.3	81.5		112.76
Measured luminosities							
$^{(leg)}L_X$	1445	276	1.05	10.57	0.673	0.54	7375
$^{(ros)}L_X$	1101	266	1.14	2.43	0.58	0.51	1856
ROSAT[8]	661	419.16	1.9	2.1	0.22		1205
$^{(ein)}L_X$	1265	253	0.65	2.53	0.26	0.3	1693
Einstein[13]	371	281	1.21	1.47	0.074	0.148	2900

$^{(leg)}$Total range of the LETGS
$^{(ros)}$Range 0.1–2.4 keV (ROSAT range: 5.2–124 Å)
$^{(ein)}$Range 0.15–4 keV (Einstein range: 3–83 Å)

The CORA program is particularly useful for LETGS spectra, but is designed in a way that other spectra can also be analyzed.
The powerful method of the He-like triplets for density measurements (cf. Sect. 1.4.1), for the first time applied in great detail to another star than the Sun, is described in Chapter 3. Densities and temperatures are derived for Capella and Procyon, and conclusions to the distribution of the coronal plasma are discussed.
A similar but more extensive study of an LETGS spectrum of Algol is given in Chapter 4. Besides the He-like triplets, Fe XXI line ratios are used to obtain plasma densities. A number of Fe lines are detected in the spectrum and are used for temperature measurements and estimation of optical depth effects. The continuum emission is modeled under the assumption of the Maxwellian bremsstrahlung mechanism in order to derive an upper limit of the temperature and emission measure. New insights are found using the measured temperatures, densities and emission measure.
The analysis of temperatures and densities for the seven stars Algol, Capella, Procyon, ϵ Eri, α Cen A and B, and UX Ari with quite different properties and degrees of activity is given in Chapter 5. A summary of this sample of stars and the observations is given in Tab. 1.3. Trends indicating higher temperatures and higher densities for the more active stars are found, although the RS CVn stars

seem to behave differently.
The two Chapters 6 and 7 are dedicated to a closer look on the radiation fields, posing problems on the density analysis with the prominent He-like triplets. Archival data from the IUE satellite are used to measure the influence from the radiation fields (see also Sect. 1.4.1.1), and a clear trend with the spectral type of the stars is pointed out. The situation in the Algol system is especially interesting, given the exceptional situation that the radiation field does not originate from the stellar surface but from the companion star, making the influence of the radiation field dependent on either the spatial distribution of the coronal plasma or the phase of the system. This is described in Chapter 6, while Chapter 7 focuses more on the comparison between the seven stars discussed in Chapter 5.

References for Table 1.3

[8]Berghöfer T.W., Schmitt J.H.M.M., & Cassinelli J.P., 1996, A&A 118, 481

[1]Drake & Smith 1993, ApJ 412, 797

[2]England 1980 MNRAS 191, 23

[3]Fekel, Moffett, & Henry 1986, ApJS 60, 551

[4]Fuhrmann *et al.*, 1997, A&A 323, 909

[5]Gray 1981, ApJ 251, 152

[6]Gray & Baliunas 1996, ApJ 441, 436

[7]Hummel *et al.*, 1994, ApJ 107(5), 1859

[8]Hünsch M., Schmitt J.H.M.M., & Voges W., 1998, A&A 132, 155

[8]Hünsch M., Schmitt J.H.M.M., Sterzik M.F., & Voges W., 1999, A&A 135, 319

[9]derived from i=31.91° by Innis, Isaak *et al.*, 1994, MNRAS 271, 573

[10]Irwin *et al.*, 1992, PASP 104, 489

[11]Kelch *et al.*, 1978, ApJ 220, 962

[12]Krisciunas & Guinan 1990, Informational Bulletin on Variable Stars, 3548, 1

[13]McDowell J.C., 1994, The Einstein Observatory Soft X-ray Source List, HEAO, Einstein Obs. Unscreened IPC Data Archive

[14]Noyes *et al.*, 1984, ApJ 285, L23

[15]Perryman M.A.C., Lindegren L., Kovalevsky J., *et al.*, 1997, A&A 323L, 49

[16]Richards M.T. 1993, ApJ, 86, 255

[17]Saar S.H. & Osten R.A. 1997, MNRAS 284, 803

[18]Schmitt & Favata 1999, Nat 401, 44

[19]Soderblom 1986, A&A 158, 273

[20]Strassmeier *et al.*, 1993, A&A 100, 173

[21]Vogt S.S. & Hatzes A.P., 1991, sacs coll 297

Bibliography

Acton L.W., 1996, in Proceedings of CSW9, eds. R. Pallavicini and A.K. Dupree, ASP Conf. Ser. 109, 45

Arnaud K.A., 1996, Astronomical Data Analysis Software and Systems V, eds. Jacoby G. and Barnes J., p17, ASP Conf. Series volume 101.

Audard M., Behar E., Güdel M., *et al.*, 2001, A&A 365, L329

Blumenthal G.R., Drake G.W., & Tucker W.H., 1972, ApJ 172, 205

Brickhouse N.S., Raymond J.C., & Smith B.W., 1995, ApJS 97, 551

Brickhouse N.S., Dupree A. K., Edgar R. J., 2000, ApJ 530, 387

Brown G.V., Beiersdorfer P., Chen H., *et al.*, 2001, ApJ 557, L75

Canizares C.R., Huenemoerder D.P., Davis D.S., *et al.*, 2000, ApJ 539, L41

Dere K. P., Landi E., Young P. R., & Del Zanna G., 2001 ApJS 134, 331, The Chianti database, with extension to X-Ray wavelengths

Gabriel A.H. & Jordan C., 1969, MNRAS 145, 241

Galilei Galileo, Welser Marcus, de Filiis Angelo Istoria E dimostrazioni intorno alle macchie solari E loro accidenti comprese in tre lettere scritte all'illvstrissimo signor Marco Velseri, Roma, G. Mascadi, 1613.

Grotrian W., 1939, Naturwiss. 27, 214

Güdel M., Audard M., Briggs K., *et al.*, 2001a, A&A 365, L336

Güdel M., Audard M., Magee H., *et al.*, 2001b, A&A 365, L344

Güdel M., Ginan E.F., & Skinner S.L., 1997, ApJ 483, 947

Hale G.E., 1908, ApJ 28, 315

Holt S.S., White N.E., Becker R.H., *et al.*, 1979, ApJ 234, L65

Hünsch M., Schmitt J.H.M.M., & Voges W., 1998, A&A 132, 155

Hünsch M., Schmitt J.H.M.M., Sterzik M.F., & Voges W., 1999, A&A 135, 319

Jordan C., Sim S.A., McMurry A.D., and Aruvel M., 2001, MNRAS 326, 303

Kaastra J. & Mewe R., 1995, A&A 302, L13

Kaastra J.S., Mewe R., & Nieuwenhuijzen H., 1996, in UV and X-ray Spectroscopy

King R.B., 1934, ApJ 80, 136

Mason H.E., Doschek G.A., Feldman U., & Bhatia A.K., 1979, A&A 73, 74

Mewe R. & Schrijver J., 1978, A&A 65, 99

Mewe R., Gronenschild E.H.B.M., Westergaard N.J., *et al.* 1982, ApJ 260, 233

Mewe R., Kaastra J.S., & Liedahl D.A., 1995, Legacy 6, 16 (MEKAL)

Mewe R., Raassen A.J.J., Drake J.J., *et al.*, 2001, A&A 368, 888

Ness J.U., Mewe R., Schmitt J.H.M.M., *et al.*, 2001a, A&A 367, 282

Ness J.U., Mewe R., Schmitt J.H.M.M., *et al.*, 2001b, ASP Conf. Series, in press (talk held at Stellar Coronae 2001)

Ness J.U., Mewe R., Schmitt J.H.M.M., *et al.*, 2001c, ASP Conf. Series, in press (poster at Stellar Coronae 2001)

Ness J.U., Mewe R., Schmitt J.H.M.M., *et al.*, 2001d, PASP in press (presentation at Cool Stars workshop CSW12)

Ness J.U., Schmitt J.H.M.M., Burwitz V., *et al.*, 2001e, submitted to A&A

Parker E.N., 1979, Cosmical Magnetic Fields, Oxford Univ. Press, Oxford

Phillips K.J.H., Mathioudakis M., Huenemoerder D.P., *et al.*, 2001, MNRAS 325, 1500

Porquet D., Mewe R., Dubau J., *et al.*, 2001, A&A 376, 1113

Pradhan A.K. & Shull J.M., 1981, ApJ 249, 82

Pradhan A.K., Norcross D.W., & Hummer D.G., 1981, ApJ 246, 1031

Pradhan A.K., 1982, ApJ 263, 477

Pradhan A.K., 1985, ApJ 288, 824

Raymond J.C. & Smith B.W., 1977, ApJS 35, 419

Rosner R., Tucker W.H., & Vaiana G.S., 1978, ApJ 220, 643

Schmitt J.H.M.M., Haisch B.M., & Drake J.J., 1994, Science 265, 1420

Schmitt J.H.M.M., Fleming T.A., & Giampapa M.S., 1995, ApJ 450, 392

Schmitt J.H.M.M., Drake J.J., Stern R.A., & Haisch B.M., 1996a, ApJ 457, 882

Schmitt J.H.M.M., Drake J.J., Haisch B.M., & Stern R.A., 1996b, ApJ 467, 841

Schmitt J.H.M.M., 1997, A&A 318, 215

Schrijver C.J., van den Oord G.H.J., & Mewe R., 1994, A&A 289, L23

Schwabe M., 1856, MNRAS 16, 62

Vedder P.W. & Canizares C.R., 1983, ApJ 270, 666

Vaiana G. S., Fabbiano G., Giacconi R., *et al.*, 1981, ApJ 245, 163

Vesecky J.F., Antiochos J.H. & Underwood J.H., 1979, ApJ 233, 987

Chapter 2

Fitting of individual emission lines

In the frame of this work, a specific software has been developed, capable of treating spectra measured with the Low Energy Transmission grating LETGS on board the *Chandra* observatory.

Astron. Nachr./AN **32X** (200X) X, XXX–XXX

CORA - Emission line fitting with Maximum Likelihood

A tool for spectra with small count numbers, with rigorous application of Poisson statistics

J.-U. NESS AND R. WICHMANN

Universität Hamburg, Gojenbergsweg 112, D-21029 Hamburg, Germany

Received January 24, 2002; accepted *date will be inserted by the editor*

Abstract. The advent of pipeline-processed data both from space- and ground-based observatories often disposes of the need of full-fledged data reduction software with its associated steep learning curve. In many cases, a simple tool doing just one task, and doing it right, is all one wishes.
In this spirit we introduce CORA, a line fitting tool based on the maximum likelihood technique, which has been developed for the analysis of emission line spectra with low count numbers and has successfully been used in several publications.
CORA uses a rigorous application of Poisson statistics. From the assumption of Poissonian noise we derive the probability for a model of the emission line spectrum to represent the measured spectrum. The likelihood function is used as a criterion for optimizing the parameters of the theoretical spectrum and a fixed point equation is derived allowing an efficient way to obtain line fluxes.
As an example we demonstrate the functionality of the program with an X-ray spectrum of Capella obtained with the LETGS on board the Chandra observatory. An approach of analyzing the Ne IX triplet is introduced.

Key words: Techniques: spectroscopic – X-rays: stars

1. Introduction

Many astronomical data reduction packages provide a broad range of functionality to cover all aspects of data treatment, from the reduction of raw input data up to the analysis of the final reduced data. This implies that these packages are huge and may have a steep learning curve. Also, sometimes their data analysis tasks require sophisticated input formats (like XSPEC where input needs to be in the so-called OGIP FITS format).

On the other hand, both space- and more recently also ground-based observatories often provide observers with pre-processed, calibrated data, and basically one only would need a simple tool doing one simple task (e.g., line fitting) to perform the final data analysis. Facing this problem during the analysis of Chandra X-ray data, we have developed CORA, a tool for fitting emission lines in spectra with low count numbers (i.e., with Poissonian statistics). This tool has been used in several recent publications (e.g., Ness et al. 2001, 2002; Stelzer et al. 2002). Here we present an outline of the tool and its underlying algorithm, and discuss its relation to other software.

Given an observed spectrum, it is often desirable to determine the parameters of spectral lines by fitting a model to the data. The actual fit is done by *maximum likelihood estimation*, i.e., the probability of the data given the model parameters (the *likelihood* of the parameters) is maximized by varying the model parameters. Usually this maximum likelihood estimate is obtained by minimizing the χ^2 function:

$$\chi^2 = \sum_{i=1}^{N} \left(\frac{y_i - f(x_i; a_1 \ldots a_M)}{\sigma_i} \right)^2 , \qquad (1)$$

where (x_i, y_i) are the observed data points, N the number of data points, σ_i the measurement errors of the individual y_i, and $f(x_i; a_1 \ldots a_M)$ the function that represents the fitted model with parameters $(a_1 \ldots a_M)$.

However, the χ^2 function is only a maximum likelihood estimator if the measurement errors are normally distributed (and independent). As photon shot noise follows a Poissonian distribution (Dereniak & Crowe 1984), the assumption of normally distributed measurement errors is only valid in the limit of large counts.

Correspondence to: jness@hs.uni-hamburg.de

 0044-6337/02/32210-0223 $ 17.50+.50/0

We therefore have the following requirements:

1. For the analysis of spectral features with low counts, it is desirable to take into account the individual measurement errors σ_i for each spectral bin, and to model them with a Poisson distribution.
2. To handle different instruments, it should be possible to choose between different line profiles, where the minimum set of useful profiles would be include the Gauss, Lorentz, and Voigt profiles.
3. To improve portability, the format of the input data should be as simple as possible, possibly plain ASCII data. This is because it is always much easier to convert a sophisticated format into a simpler one than vice versa.
4. In order to obtain quick and useful results, usage should be simple, and there should be a GUI (Graphical User Interface) to guide the user.
5. The program should not require proprietary tools that might not be available for some prospective users.

2. Data input

The spectrum to be analyzed must be provided as an ASCII file containing five columns: (1) wavelengths, (2) raw counts, (3) errors for counts, (4) instrumental background in counts, and (5) an error for the instrumental background counts. The non-subtracted spectrum should be given in counts, negative values will not be accepted. The instrumental background must be given on the same wavelength grid.

As the algorithm is based on the assumption of Poissonian errors, the count errors in the data file are only used for including error bars in the final plot.

The errors in the instrumental background are not used in the current version, instead they are also assumed to be Poissonian in the algorithm. The spectrum can also be given in three columns (wavelength, counts, and background counts), or two columns (wavelength and counts). For the errors the square root of the count numbers will be adopted, and, in the latter case, the instrumental background will assumed to be zero in all bins.

3. Method of analysis

3.1. Background treatment

Before determining the flux of any emission line, the background must be modeled. The background consists of essentially two components: instrumental background and source background, which may consist of continuum radiation and weak, unresolved lines.

The instrumental background bg is also present on those parts of the detector not illuminated by the target source, such that it can be obtained from regions adjacent to the spectral trace on the detector. We supply the option to use a second-order polynomial to smooth the instrumental background.

A far more difficult task is the determination of a reliable source background sbg. The source background is by definition present only on the extracted spectral trace, and may be contaminated by weak, unrecognized spectral lines and/or specific effects of the instrument, e.g., higher order contamination.

In order to estimate the source background, we adopted the following procedure. We first concentrate on the spectral region of interest, and consider the continuum in this (small) region as constant, thus one parameter sbg is sufficient to describe the source background. In this region we generate a background subtracted spectrum, and calculate the median of the count values thus obtained for all bins within the investigated (small) part of the spectrum. All bins containing more counts than 3σ above this median value are excluded from calculating a final median value, which is used as a constant source background sbg measured in counts/Å. The median is a statistically robust estimate of the continuum (which we implicitly assume to be flat over the considered part of the spectrum) as long as more than 50% of all bins belong to the source background, i.e., the spectrum contains not too many lines.

For each bin i with the bin-size $\Delta\lambda$ in Å we thus obtain a total value for the background of $b_i = \frac{sbg}{\Delta\lambda} + bg_i$ in the studied wavelength range.

3.2. Fit procedure

The emission line spectra are fitted with a maximum likelihood technique similar to that used by Schmitt et al. (1996) for their EUVE spectra. The spectrum is assumed to consist of the background b and of M discrete emission lines. The treatment of the background b is described in Sect. 3.1.

Each line j is assumed to be represented by a normalized profile $g_j(\lambda; \lambda_j, \sigma_j)$, e.g., a Gaussian profile

$$g_j(\lambda; \lambda_j, \sigma_j) = \frac{1}{\sqrt{2\pi}\sigma_j} \mathrm{e}^{-\frac{(\lambda-\lambda_j)^2}{2\sigma_j}} \quad (2)$$

with the dispersion σ_j and the central wavelength λ_j. The choice of an adequate profile function depends on the properties of the grating, the detector and, provided sufficient spectral resolution, the physical properties of the source. In the current version a Gauss profile, a Lorentz profile, and a Pseudo-Voigt profile are implemented. Other profile functions can easily be implemented. In the pseudo-Voigt approximation the weighted sum of a Gauss and a Lorentz profile

$$Voigt_{\mathrm{pseudo}} = (1-\eta)Gauss(\Gamma) + \eta Lorenz(\Gamma)$$

is used. Here, the FWHM Γ is computed as

$$\Gamma = (\Gamma_{\mathrm{G}}^5 + 2.69296\Gamma_{\mathrm{G}}^4\Gamma_{\mathrm{L}} + 2.42843\Gamma_{\mathrm{G}}^3\Gamma_{\mathrm{L}}^2 + 4.47163\Gamma_{\mathrm{G}}^2\Gamma_{\mathrm{L}}^3 + 0.07842\Gamma_{\mathrm{G}}\Gamma_{\mathrm{L}}^4 + \Gamma_{\mathrm{L}}^5)^{1/5}.$$

The mixing parameter η is computed as

$$\eta = 1.36603(\Gamma_{\mathrm{L}}/\Gamma) - 0.47719(\Gamma_{\mathrm{L}}/\Gamma)^2 + 0.11116(\Gamma_{\mathrm{L}}/\Gamma)^3.$$

(For reference, see Thompson et al. 1987).

After the selection of M lines with their central wavelengths λ_j and their linewidths σ_j a specific part of the total spectrum will be extracted for investigation, including all selected lines with sufficient adjacent background. This part of the spectrum contains a number of bins, called N here, and

the number of expected counts c_i in the i^{th} bin can be calculated as

$$c_i = \frac{sbg}{\Delta\lambda} + bg_i + \sum_{j=1}^{M} a_j g_{i,j} \ , \tag{3}$$

where a_j, the amplitude, reflects the total number of counts of line j, and $g_{i,j}$ is the value of the normalized profile function for line j in bin i. In order to compare the modeled spectrum c_i with the measured spectrum n_i, we assume n_i to be a Poisson realization of c_i. The total probability of the observations $n_1 \ \ldots \ n_N$ is then given by

$$P(n_1 \ \ldots \ n_N) = \prod_{i=1}^{N} e^{-c_i} \frac{c_i^{n_i}}{n_i!} \tag{4}$$

and the likelihood function $\mathcal{L}(a_j, \lambda_j, \sigma_j, j = 1 \ldots N)$ is defined as

$$\mathcal{L} = -2 \ \ln P = -2 \sum_{i=1}^{N} (-c_i + n_i \ln c_i) + const \ . \tag{5}$$

The best-fit values of the parameters a_j, λ_j, and σ_j ($j = 1 \ \ldots \ N$) are determined by finding extremal values of $\mathcal{L}$ through:

$$\frac{\partial \ln \mathcal{L}}{\partial \, a_j} = 0 \qquad \frac{\partial \ln \mathcal{L}}{\partial \, \lambda_j} = 0 \qquad \frac{\partial \ln \mathcal{L}}{\partial \, \sigma_j} = 0 \ . \tag{6}$$

λ_j and σ_j are in principle fixed by the wavelengths of the considered lines and the instrumental resolution. Complications arise from possible wavelength calibration errors and line blends. A minimization procedure is provided for solving Eqs. 6 numerically for λ_j and σ_j, such that no derivative of the normalized profile function is necessary. The amplitudes a_j, proportional to the line flux, are the genuine interesting parameters. Analysis of the likelihood equations shows that for the amplitudes a_j a fixed point equation can be derived for each line j with λ_j and σ_j assumed to be given:

$$a_{j,new} = \sum_{i=1}^{N} n_i \frac{a_{j,old} g_{i,j}}{c_{i,old}} \ . \tag{7}$$

We point out that this fixed point equation is independent of the choice of the profile function.

Eq. 7 can be efficiently solved by iteration. Measurement errors are determined by assuming the likelihood curve $\mathcal{L}(a_j)$ to be parabolic and finding the value of Δa_j where $\mathcal{L}(a_j \pm \Delta a_j) = \mathcal{L}(a_j) + \mathrm{d}\mathcal{L}$ resulting in $\Delta a_j = \sqrt{2\mathrm{d}\mathcal{L}/\mathcal{L}_j''}$ with $\mathcal{L}_j''$ the second derivative of $\mathcal{L}$ with respect to a_j known from equations 5 and 3. We choose $\mathrm{d}\mathcal{L} = 1$ which yields formal 1 σ errors (Press et al. 1992).

Similarly the errors for λ_j and σ_j are calculated in the case the values are optimized by minimization. We determine the errors in $\mathrm{d}\lambda_j$ and $\mathrm{d}\sigma_j$ numerically from $\mathcal{L}(\lambda_j)$ and $\mathcal{L}(\sigma_j)$, respectively with $\mathrm{d}\mathcal{L} = 1$, i.e., errors being given within 68.3%; thus formally we treat all other parameters as "uninteresting".

When measuring line blends, a more refined error analysis is necessary for the amplitudes in order to account for correlated errors. This is done by calculating the matrix of correlated errors $\Delta a_{ij} = \sqrt{2\partial\mathcal{L}/\partial\mathcal{L}_i\partial\mathcal{L}_j}$. The Eigenvalues $E_j(\Delta a_{ij})$ of this matrix (Hesse-matrix) will be the correlated errors Δa_j (cf. Strong 1985).

3.2.1. Imposing restrictions on the fit

The algorithm has been developed in the context of analyzing high resolution X-ray spectra of cool stars (e.g., Ness et al. 2001, 2002) obtained with the LETGS on board Chandra. It is therefore designed to meet some of the specific challenges of this instrument. Nevertheless some of these features are useful in a variety of other contexts as well. The spectra measured with the LETGS contain a number of isolated and blended emission lines above a continuum of varying strength. A good profile function for these emission lines is the Gauss profile function (Eq. 2). When fitting multiple lines, the relative line positions are well known (e.g., Dere et al. 2001), while absolute line positions might need correction. For this purpose the wavelengths λ_j can vary either freely or - if the relative wavelength positions of the lines to be fitted are known - only one line is fitted, and all other line positions will be set according to the relative line positions given with the start values in order to account for possible shifts of the overall wavelength scale.

The great benefit from the high-resolution X-ray spectra lies in the new opportunity to analyze the plasma by use of temperature- and density sensitive line flux ratios. When dealing with low-signal data or with blends, it can be desirable to require certain line ratios to be fixed to values that retain realistic physical conditions, while still obtaining the best fit result for the rest. For this purpose M weights f_j and a value v can be given fulfilling

$$\sum_{j=1}^{M} f_j a_j = v \ . \tag{8}$$

All lines with $f_j = 0$ can vary freely. Choosing, e.g., $f_2 = 4$, $f_5 = -1.$, and $v = 0$, a constraint on the line flux ratio of $f_5/f_2 = 4$ can be demanded, while fitting the other line counts $a_{j\neq 2,5}$ freely. This feature has been used by Ness et al. (2002) for fitting the Ne IX triplet for Algol, which is heavily blended by Fe XIX. The same Ne IX triplet is also seen in the Chandra LETGS spectrum of Capella, and in Sect. 4, we discuss the deblending of this triplet using CORA in some detail.

A big problem of the LETGS is the higher dispersion orders, which cannot be disentangled from the first order by intrinsic energy resolution of the detector. The wavelengths of the fitted lines can be multiplied with a factor reflecting the dispersion order. In that way the line flux of, e.g., the O VIII line at 18.97 Å can be measured at 38 Å, 57 Å, 76 Å, etc. with the same starting value, i.e., 18.97 Å in combination with the corresponding factor. This feature can also be used for systematic blue- or redshifts.

3.3. Implementation details

The introduced program consists of two independent parts. The actual fit program is a standalone program written in ANSI C that reads in the spectrum and a *configuration file* performs the fit outputs the results and generates a plot (using the PGPLOT vector plotting library). The configuration file contains initial fitting parameters as well as settings for various options for fitting and plotting.

To customize the selection of input parameters and options, the program is delivered with a graphical user interface (GUI) programmed with GTK+ (Gimp ToolKit), a multiplatform open source GUI toolkit. This GUI allows to interactively select the region of interest within the spectrum, set initial values for plotting parameters, select options for fitting and plotting, and actually run the fit.

The program can be used to create plots for publication. Plot parameters can be given modifying the outlook of the plot, e.g., only the spectrum can be plotted with no fitted line, or labels can be included, as can be seen in Fig. 1.

4. Analysis of a Chandra LETGS spectrum of Capella

In order to demonstrate the potential of the developed tool, we present as an example, a Chandra LETGS spectrum of Capella (cf. Ness et al. 2001, Mewe et al. 2001). The analysis of the Ne IX triplet is particularly difficult, because the intercombination line at 13.52 Å is blended by an Fe XIX line. For this reason Mewe et al. (2001) did not analyze the Ne IX triplet, and also the HETGS spectra, in spite of its better resolution, posed problems that were not fully solved by Canizares et al. (2000) or Phillips et al. (2001).

However, density diagnostics with the Ne IX triplet is interesting, because it allows to probe plasma of intermediate temperature. Although it is not possible to resolve the blend, the problem can be approached by using physical constraints derived from other lines in the spectrum in order to restrict the fit parameters.

Using the CORA tool presented here, in their analysis of Algol Ness et al. (2002) used a fixed G ratio (cf. Gabriel & Jordan 1969) that grants a realistic plasma temperature. Since the theoretical wavelengths are not as reliable as the resolution, the wavelength values were iterated freely. We applied this technique to the Capella LETGS spectrum, and show the result in Fig. 1. As can be seen from the labels, the G ratio is 0.8, and a measured f/i ratio of 3.24 $\pm$ 0.35 (68.3% confidence error) is obtained, which is consistent with the ratio measured by Ayres et al. (2001). They give 2.9 $\pm$ 0.5, but point out that their value is uncertain due to the blending.

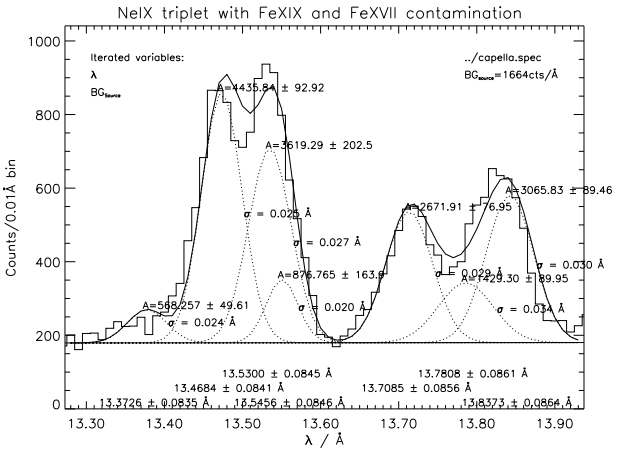

Fig. 1. Spectrum of Capella: Example of a constrained fit of the Ne IX triplet at 13.5 Å, where the intercombination line at 13.52 Å is blended by an Fe XIX line.

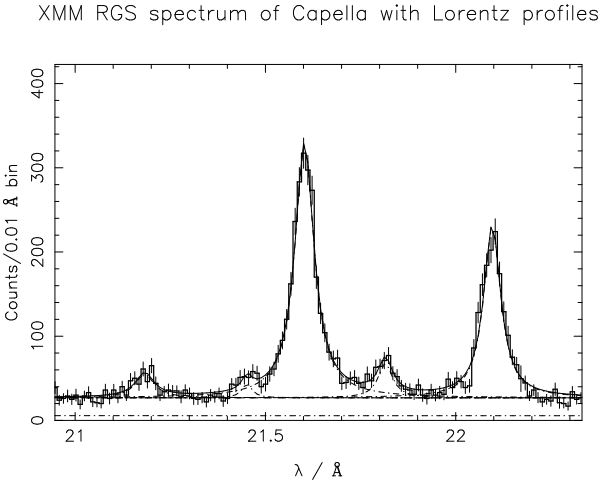

Fig. 2. XMM-RGS Spectrum of Capella: It is clearly visible that the Lorentzian profile function is best suited for RGS spectra.

5. Conclusion

5.1. Limitations

The program is designed for a specific purpose, but is programmed for more general applications. However, not all possible demands are met, and we wish to point out this fact by mentioning the limitations.

The source background is considered a constant within the wavelength range of interest. This assumption might be poor in cases when the wavelength region of interest is large, which is the case when the emission lines are far apart. The procedure is therefore limited to (multiple) fitting of nearby lines only. The small wavelength range restricts the program to fitting only individual lines, but no global fit is possible with this program.

The line profiles are restricted to Gaussian, Lorentzian, or Pseudo Voigt profile functions. Experience has shown that the Chandra LETGS and HETGS spectra are sufficiently well modeled with the Gaussian profile, while XMM RGS spectra require Lorentzian profiles (cf. Fig. 2). Other normalized profiles, however, can easily be implemented.

The algorithm follows the philosophy to stick as close to the raw data as possible in order to avoid interference of systematic errors with statistical errors. We therefore insist on non-subtracted count spectra to be given. Flux spectra can of course be given, because the units cannot be checked. Systematic errors in the effective areas and the exposure time, however, spoil the Poisson statistics, such that no useful errors will be returned. Since the subtraction of the instrumental background also spoils the Poisson statistics, no spectrum containing bins with negative count values will be accepted.

5.2. Comparison with other tools

We have developed CORA because we felt that none of the existing tools, at least those we know of, did fulfill our perceived needs.

In particular, both the popular MIDAS and IRAF packages provide tasks for line fitting and deblending, but according to the documentation the assumption of Poisson statistics is only used in the final derivation of error estimates (e.g., in the IRAF SPECFIT task), while from Eqs. 6 one can see that the Poisson statistics directly enters into the likelihood function that determines the fit result, and therefore should be accounted for not only for error estimation, but also for the fitting procedure itself. This is done in the rigid approach used by CORA.

The XSPEC package provides a task to perform line fitting with Poisson statistics. However, XSPEC requires input data in a special FITS format, and in fact we have not been able to convert the ASCII data available to us into that format. XSPEC is an excellent reduction tool, treating raw data from X-ray missions, but once the reduction has been performed in another way but with XSPEC, it is very difficult to make use of the XSPEC tasks for further data analysis. In such cases, tools like CORA are clearly the better choice. As noted above, CORA is limited to fits within small spectral windows. For global fits, eventually including a more or less complete list of lines, XSPEC is certainly superior.

Since CORA pursues only one single goal, in contrast to many other applications it is easy to use, and also easy to install. CORA is released under the terms of the GNU Public License (FSF 1991), and can be downloaded from the METALAB ftp archive (http://metalab.unc.edu/pub/Linux/science/astronomy).

Acknowledgements. The development of CORA has benefitted substantially from discussions with J. H. M. M. Schmitt.
J.-U.N. acknowledges financial support from Deutsches Zentrum für Luft- und Raumfahrt e.V. (DLR) under 50OR98010.
R.W. acknowledges financial support from the Deutsche Forschungsgemeinschaft (DFG Schwerpunktprogramm 'Physics of star formation').

References

Ayres T. R., Brown A., Osten R., et al., 2001, ApJ 549, 554
Canizares C. R., Huenemoerder D. P., Davis D.S., et al. 2000, ApJ 539, L41
Dere K. P., Landi E., Young P. R., Del Zanna G. 2001, ApJS 134, 331 (The Chianti line database)
Dereniak E. L. & Crowe D. G. 1984, Optical Radiation Detectors (New York: Wiley)
Gabriel A. H. & Jordan C., 1969, MNRAS 145, 241
Mewe R., Raassen A. J. J., Drake J. J., et al., 2001,A&A 368, 888
Free Software Foundation Inc. (FSF) 1991, 59 Temple Place - Suite 330, Boston, MA 02111-1307, USA
Ness J. U., Mewe R., Schmitt J. H. M. M., Raassen A. J. J., et al., 2001, A&A 367, 282
Ness J. U., Schmitt J. H. M. M., Burwitz V., et al. 2002, submitted
Press W. H., Teukolsky S. A., Vetterling W. T., Flannery B. P. 1992, Numerical Recipes, Cambridge Univ. Press
Phillips K. J. H., Mathioudakis M., Huenemoerder D. P. et al. 2001, MNRAS 325, 1500
Schmitt J. H. M. M., Drake J. J., Stern R. A. et al., 1996, Astrophys. J. 457, 882
Stelzer B., Aschenbach B., Audard M. et al. 2002, in prep.
Strong A. W., 1985 A&A, 150, 273
Thompson P., Cox D. E., & Hastings J. B., J. Appl. Cryst. 1987 20, 79

Chapter 3

Density diagnostics for Capella and Procyon

Published in:
Astronomy and Astrophysics, Vol. 367, pp. 282-296 (2001)

Astronomy & Astrophysics 367, 282-296 (2001)

Helium-like triplet density diagnostics:

Applications to CHANDRA–LETGS X-ray observations of Capella and Procyon

J.-U. Ness[1], R. Mewe[2], J.H.M.M. Schmitt[1], A.J.J. Raassen[2,3], D. Porquet[4], J.S. Kaastra[2], R.L.J. van der Meer[2], V. Burwitz[5], and P. Predehl[5]

[1] Universität Hamburg, Gojenbergsweg 112, D-21029 Hamburg, Germany
[2] Space Research Organization Netherlands (SRON), Sorbonnelaan 2, 3584 CA Utrecht, The Netherlands
[3] Astronomical Institute "Anton Pannekoek", Kruislaan 403, 1098 SJ Amsterdam, The Netherlands
[4] CEA/DSM/DAPNIA, Service d'Astrophysique, CEA Saclay, F-91191 Gif sur Yvette Cedex, France
[5] Max-Planck-Institut für Extraterrestrische Physik (MPE), Postfach 1603, D-85740 Garching, Germany

Received 18 September 2000 / Accepted 1 December 2000

Abstract. Electron density diagnostics based on the triplets of Helium-like C V, N VI, and O VII are applied to the X-ray spectra of Capella and Procyon measured with the Low Energy Transmission Grating Spectrometer (LETGS) on board the Chandra X-ray Observatory. New theoretical models for the calculation of the line ratios between the forbidden (f), intercombination (i), and the resonance (r) lines of the helium-like triplets are used. The (logarithmic) electron densities (in cgs units) derived from the f/i ratios for Capella are $< 9.38\,\mathrm{cm}^{-3}$ for O VII (2σ upper limit) (f/i=4.0±0.25), 9.86 ± 0.12 cm^{-3} for N VI (f/i=1.78±0.25), and 9.42 ± 0.21 cm^{-3} for C V (f/i=1.48±0.34), while for Procyon we obtain $9.28^{+0.4}_{-9.28}$ cm^{-3} for O VII (f/i=3.28±0.3), 9.96 ± 0.23 cm^{-3} for N VI (f/i=1.33±0.28), and < 8.92 cm^{-3} for C V (f/i=0.48±0.12). These densities are quite typical of densities found in the solar active regions, and also pressures and temperatures in Procyon's and Capella's corona at a level of $T \sim 10^6$ K are quite similar. We find no evidence for densities as high as measured in solar flares. Comparison of our Capella and Procyon measurements with the Sun shows little difference in the physical properties of the layers producing the C V, N VI, and O VII emission. Assuming the X-ray emitting plasma to be confined in magnetic loops, we obtain typical loop length scales of $L_{Capella} \geq 8\ L_{Procyon}$ from the loop scaling laws, implying that the magnetic structures in Procyon and Capella are quite different. The total mean surface fluxes emitted in the helium- and hydrogen-like ions are quite similar for Capella and Procyon, but exceed typical solar values by one order of magnitude. We thus conclude that Procyon's and Capella's coronal filling factors are larger than corresponding solar values.

Key words. Atomic data – Atomic processes – Techniques: spectroscopic – Stars: individual: Capella & Procyon – stars: coronae – stars: late-type – stars: activity – X-rays: stars

1. Introduction

The hot plasma in the corona of the Sun and of other stars is thought to be in "coronal equilibrium". Atomic excitations occur through collisions with electrons. The excited atoms decay radiatively and the emitted radiation escapes without any further interaction with the emitting plasma. As a consequence, the emission is optically thin, and the total flux emitted in some spectral band or in a given emission line is proportional to the emission measure EM, defined as the integral of the square of the plasma density n over the emitting volume elements dV through $EM = \int n^2 \mathrm{d}V$. Thus, observationally, the contributions of density and volume to a given observed value of EM cannot be disentangled.

Stellar X-ray surveys carried out with the *Einstein* and ROSAT satellites have shown an enormous range of X-ray luminosity (L_X) for stars of given spectral type (cf., Vaiana et al. (1981), Schmitt (1997)). Typically, one observes star to star variations in L_X of up to four orders of magnitude, with the largest X-ray luminosities found among the stars with the largest rotation rates. While one definitely finds a correlation between mean coronal temperature and X-ray luminosity (Schmitt et al. (1985); Schmitt (1997)), it is also clear that the single-most important factor contributing to the large variations in L_X is

Send offprint requests to: J.-U. Ness
Correspondence to: jness@hs.uni-hamburg.de

the variation in emission measure. The conclusion therefore is that active stars (can) have a couple of orders of magnitude higher coronal emission measure, while maintaining the same optical output as low-activity stars like our Sun.

The emission measure is directly linked to the structure of stellar coronae, if we assume, going along with the solar analogy, that the X-ray emitting plasma of a stellar corona is confined in magnetic loops. The observed values of EM and L_X for a given star could be accounted for either by the existence of more loops than typically visible on the solar surface, by higher density loops or by longer, more voluminous loops. Thus the question is reduced to the following: if $EM_\star \gg EM_\odot$ for an active star, one wants to know whether this is due to $n_\star > n_\odot$ or $V_\star > V_\odot$ or both.

Spatially resolved solar observations allow to disentangle density and volume contributions to the overall emission measure. One finds the total X-ray output of the Sun dominated – at least under maximum conditions – by the emission from rather small, dense loops. Stellar coronae always appear as point sources. The only way to infer structural information in these unresolved point sources has been via eclipse studies in suitably chosen systems where one tries to constrain the emitting plasma volume from the observed light curve. Another method to infer structure in spatially unresolved data are spectroscopic measurements of density. The emissivity of plasma in coronal equilibrium in carefully selected lines does depend on density. Some lines may be present in low-density plasmas and disappear in high-density plasmas such as the forbidden lines in He-like triplets, while other lines may appear in high-density plasmas and be absent in low-density plasmas (such as lines formed following excitations from excited levels). With the high-resolution spectroscopic facilities onboard *Chandra* it is possible to carry out such studies for a wide range of X-ray sources. The purpose of this paper is to present and discuss some key density diagnostics available in the high-resolution grating spectra obtained with *Chandra*. We will specifically discuss the spectra obtained with the Low Energy Transmission Grating Spectrometer (LETGS) for the stars Capella and Procyon.

Both Capella and Procyon are known to be relative steady and strong X-ray sources; no signatures of flares from these stars have ever been reported in the literature. Both Capella and Procyon are rather close to the Sun at distances of 13 pc and 3.5 pc (Tab. 1), so that effects of interstellar absorption are very small. Both of them have been observed with virtually all X-ray satellites flown so far. Capella was first detected as an X-ray source by Catura et al. (1975), and confirmed by Mewe et al. (1975), Procyon by Schmitt et al. (1985). The best coronal spectra of Capella were obtained with the *Einstein* Observatory FPCS and OGS (Vedder et al. (1983), Mewe et al. (1982)), the EXOSAT transmission grating (Mewe et al. (1986), Lemen et al. (1989)) and EUVE (Dupree et al. (1993), Schrijver et al. (1995)), while high-spectral resolution spectral data for Procyon have been presented by Mewe et al. (1986) and Lemen et al. (1989) using EXOSAT transmission grating data and Drake et al. 1995 and Schrijver et al. (1995) using EUVE data. Note that Schmitt et al. (1996b) and Schrijver et al. (1995) investigated the coronal density of Procyon using a variety of density sensitive lines from Fe X to Fe XIV in the EUV range and found Procyon's coronal density consistent with that of solar active region densities.

Table 1. Properties of Procyon and Capella: mass M, radius R, effective temperature $T_{\rm eff}$, log g and the limb darkening coefficient ϵ

	Procyon	Capella
d/pc	3.5	13
$M/M_\odot$	1.7 ± 0.1[4]	2.56 ± 0.04[3]
$R/R_\odot$	2.06 ± 0.03[4]	9.2 ± 0.4[3]
$T_{\rm eff}$/K	6530 ± 90[2]	5700 ± 100[3]
log g	4.05 ± 0.04[2]	2.6 ± 0.2[5]
Spectr. type	F5 IV-V	Ab: G1 III
		(Aa: G8/K0 III)
ϵ	0.724[1]	0.83[1]

References:
[1]Díaz-Cordovés et al. (1995),
[2]Fuhrman et al. (1997),
[3]Hummel et al. (1994),
[4]Irwin et al. (1992),
[5]Kelch et al. (1978)

The plan of our paper is as follows: We first briefly review the atomic physics of He-like ions as applicable to solar (and our stellar) X-ray spectra. We briefly describe the spectrometer used to obtain our data, and discuss in quite some detail the specific procedures used in the data analysis, since we plan to use these methods in all our subsequent work on *Chandra* and XMM-Newton spectra. We then proceed to analyze the extracted spectra and describe in detail how we dealt with the special problem of line blending with higher dispersion orders. Before presenting our results we estimate the formation temperatures of the lines, the influence of the stellar radiation field and the influence of optical depth effects followed by detailed interpretation. The results will then be compared to measurements of the Sun and we close with our conclusions.

2. Atomic physics of He-like ions

The theory of the atomic physics of helium-like triplets has been extensively described in the literature (Gabriel & Jordan (1969), Blumenthal et al. (1972), Mewe & Schrijver (1978), Pradhan et al. (1981), Pradhan & Shull (1981),

Pradhan (1982), Pradhan (1985), and recently Porquet & Dubau (2000) and Porquet et al. (2001)). Basically, the excited states (1s2l) split up into the terms 2^1P, $2^3P, 2^1S$, and 2^3S, out of which the levels with J $\neq 0$ decay to the ground state 1^1S through the resonance line (abbreviated by r), the intercombination line (i) and the forbidden line (f), respectively; the latter two lines involve spin changes and therefore violate the selection rules for electric dipole radiation. Although the radiative transition rate for the forbidden line is quite small, in a low-density plasma collisional depopulation processes are so rare, that the excited 2^3S state does decay radiatively. In a high-density plasma collisional deexcitations dominate and hence the forbidden line disappears. Complications arise from other competing processes populating and depopulating the ^3P and ^3S levels. These are in particular radiative transitions induced by the underlying photospheric stellar radiation field (discussed in Sect. 5.2) as well as ionization and recombination processes from the Li-like and H-like ions.

It is customary to describe the measured line intensities r, i and f in terms of the ratios

$$R_{\rm obs} = \frac{f}{i} \qquad \text{and} \qquad G_{\rm obs} = \frac{i+f}{r}\,. \tag{1}$$

In this paper we use the notation used in e.g. Pradhan & Shull (1981). In other contexts (e.g. calculating ions of higher ionization stages) another notation labeling r as **w**, f as **z** and i as **x**+**y** is often used pointing out that the intercombination line separates via M2 and E1 transitions into two components. Theory describes the density sensitivity of the R ratio by the functional dependence

$$R(N_{\rm e}) \;=\; R_0 \frac{1}{1+\phi/\phi_{\rm c}+N_{\rm e}/N_{\rm c}}\,. \tag{2}$$

Densities are inferred from equating $R(N_{\rm e})$ with $R_{\rm obs}$. For convenience, we follow here the expressions as given by Blumenthal et al. (1972). The low-density limit R_0, which applies for $N_{\rm e}=0$ and $\phi=0$, is given by

$$R_0 = \frac{1+F}{B} - 1, \tag{3}$$

with the radiative branching parameter B averaged over the two components of the intercombination line. The parameter $N_{\rm c}$, the so-called critical density (cf., Tab. 2), above which the observed line ratio is density-sensitive, is given by

$$N_{\rm c} = \frac{A(2^3S_1 \rightarrow\ 1^1S_0)}{(1+F)C(2^3S_1 \rightarrow\ 2^3P)}\,, \tag{4}$$

where $A(2^3S_1 \rightarrow\ 1^1S_0)$ is the radiative transition probability of the forbidden line, $C(2^3S_1 \rightarrow\ 2^3P)$ is the electron collisional rate coefficient for the transition from 2^3S to 2^3P, and F is the ratio of the collision rates from the ground to the levels 2^3S and 2^3P, respectively (including cascade effects from upper levels through radiative transitions after excitation or recombination). Finally, the parameters ϕ (the radiative absorption rate from 2^3S to 2^3P induced by an external radiation field) and $\phi_{\rm c}$ describe the additional possible influence of the stellar radiation field on the depopulation of the ^3S state (cf., Sect. 5.2). The latter is insignificant especially for the He-like triplets of higher ionization stages than C V. Values for R_0 and $N_{\rm c}$ used in this paper are listed in Tab. 2. Obviously, for very large densities or large radiation fields the forbidden line and hence R disappears. The ratio

$$G = (i+f)/r, \tag{5}$$

a measure of the relative strength of the resonance line, depends on the electron temperature, $T_{\rm e}$ (e.g., Porquet et al. (2001)). G can be used to derive temperatures for the lines used for density diagnostics that can be compared to the maximum formation temperature $T_{\rm m}$.

Table 2. Atomic Parameters for He-like triplets. $T_{\rm m}$ is the peak line formation temperature (MEKAL), R_0 is the low-density limit and $N_{\rm c}$ the density were R falls to half its low-density value.

ion	$T_{\rm m}$/MK	R_0	$N_{\rm c}/(10^{10} cm^{-3})$
C V	1	10.6	0.051
N VI	1.4	4.9	0.45
O VII	2.0	3.495	3.00

3. Instrument description

The Low Energy Transmission Grating Spectrometer (LETGS) on board the Chandra Observatory is a diffraction grating spectrometer covering the wavelength range between 2–175 Å (0.07–6 keV). 540 individual grating elements are mounted onto a toroidal ring structure. Each of the elements consists of a freestanding gold grating with 1μm grating period. The fine gold wires are held by two different support structures, a linear grid with 25.4 μm and a coarse triangular mesh with 2 mm spacing. The whole grating ring can be inserted into the convergent beam just behind the High Resolution Mirror Assembly (HRMA) thereby dispersing the light of any X-ray source in the field of view into its spectrum. The efficiency of the grating spectrometer is of the order of 10% on average but is enhanced by a factor of two around 2 keV due to partial transparency effects; a more detailed description of the instrument is presented by Predehl et al. (1997). Both sides of the spectrum are recorded with a microchannel plate detector (HRCS), placed behind the transmission grating. In contrast to CCD based detectors, the HRCS detector provides essentially no intrinsic energy resolution, the energy information for individually recorded events is solely contained in the events' spatial location.

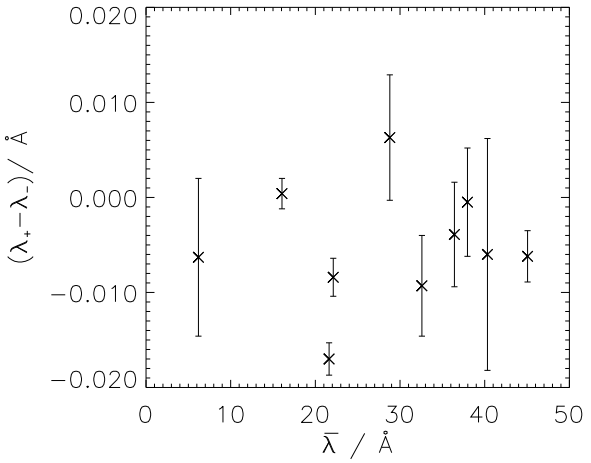

Fig. 1. Comparison of fit results from left side (λ_-) and right side (λ_+) of the spectrum.

Table 3. List of the data sets with start and stop times and durations used in this paper.

Obs. ID.	time [ksec]	Observation date [UT] start	end
Capella			
62435	22.34	09-06-1999 00:35:40	09-06-1999 06:48:01
01167	15.36	09-09-1999 13:10:06	09-09-1999 17:26:08
01244	12.37	09-09-1999 17:42:27	09-09-1999 21:08:36
62410	11.33	09-09-1999 23:43:57	09-10-1999 02:52:48
01246	15.00	09-10-1999 03:06:06	09-10-1999 07:16:08
62422	11.68	09-12-1999 18:26:42	09-12-1999 21:41:20
62423	14.80	09-12-1999 23:37:44	09-13-1999 03:44:28
01420	30.30	10-29-1999 22:49:29	10-30-1999 07:14:27
01248	85.36	11-09-1999 13:42:24	11-10-1999 13:25:05
total:	218.54		
Procyon			
00063	70.39	11-06-1999 21:24:31	11-07-1999 16:57:38
01461	70.36	11-07-1999 17:04:55	11-08-1999 12:37:39
total:	140.75		

4. Observations and data analysis

4.1. Observations

The data described and analyzed in this paper were gathered during the calibration phase of the *Chandra* LETGS. Part of the data has already been presented by Brinkman et al. (2000). The individual observation intervals used in our analysis are listed in Tab. 3. As is clear from Tab. 3, the observations extend over two days for Procyon and over two months for Capella. Our analysis refers to the mean properties of Procyon and Capella; the subject of possible time variations is not subject of this paper. The total on source integration times are 218.54 ksec for Capella and 140.75 ksec for Procyon. Since the sources are among the strongest coronal X-ray sources (cf., Hünsch et al. (1998a,b)), it is also evident that these spectra belong to the highest quality coronal X-ray spectra reasonably obtainable with the *Chandra* LETGS.

4.2. Data extraction

All the HRCS datasets analyzed in this paper (see Tab. 3) were processed using the standard pipeline processing. The incoming X-rays are diffracted by the grating, dispersing the different energy photons to different detector positions along the dispersion direction. Therefore the spectral information obtained with the LETGS has to be extracted spatially. The pulse heights with which the HRC detector records registered events contains some very modest energy information, which was, however, not used. At each wavelength, the photons have to be integrated in cross-dispersion direction. Because of the spectrograph's astigmatism, the width of the spectral trace in cross-dispersion direction is wavelength dependent. For wavelengths below 75 Å we choose a 3.6″ wide extraction box around the spectral trace which includes almost all of the source signal while keeping the background level low. For wavelengths greater than 75 Å the extraction box widens in cross dispersion direction to 8.4″ at 175 Å. In addition the photons in four background regions of identical shape to that of the object extraction region where selected. These regions are displaced 12″ and 24″ above and below the source extraction box in order to check for any spatial variation of the background in cross-dispersion direction.

4.3. Symmetry of the grating spectrum

For the purpose of verifying the symmetry of the dispersed spectra, we determined empirical wavelengths of ten strong emission lines recorded on both sides of the middle detector plate (i.e. $\lambda < 50$ Å). For the example of Capella we plot the wavelength difference $(\lambda_+ - \lambda_-)$ against the mean wavelength $\frac{1}{2}(\lambda_+ + \lambda_-)$ in Fig. 1. As can be seen from Fig. 1, the wavelength values obtained from the right and left side agree to within less than the instrumental resolution of ∼0.06 Å (cf. σ-values in Tab. 4) Both spectra can thus be added for the analysis in order to increase the SNR of the data. In the following we will always consider co-added spectra.

4.4. Method of analysis

4.4.1. Treatment of background

Before determining the flux of any emission line, the spectral background must be modeled. This background consists of essentially two components: instrumental background and source background, which may consist of continuum radiation and weak lines. The instrumental back-

ground is also present on those parts of the microchannel plate not illuminated by X-rays from the target source. We checked for any variation of the instrumental background perpendicular to the dispersion direction and found none. We then modeled this instrumental background *bg* along the dispersion direction by a low-order polynomial and found acceptable fits for almost the whole spectrum. A far more difficult task is the determination of a reliable source background *sbg*. The source background is by definition present only on the extracted spectral trace; it is formed by continuum radiation from the source, and possibly by weak, unrecognized spectral lines and/or higher order contamination.

For the determination of the fluxes of individual emission lines, the source background is required only in the vicinity of the line(s) under consideration and is approximated by a single number. Our numerical procedures can, however, scope with arbitrary source background models. In order to estimate this source background, we adopted the following procedure. We first subtracted the instrumental background from the spectral trace on the source, and calculated the median of the thus obtained count values for all bins within the investigated (small) part of the spectrum. The median is a statistically robust estimate of the background (which we assume to be flat over the considered part of the spectrum) as long as more than 50 % of all bins belong to the source background, i.e. the spectrum contains not too many lines. For each bin i we thus obtain a background value of $sbg + bg_i$ in the studied wavelength range.

4.4.2. Fit procedure

The emission line spectra are fitted with a maximum likelihood technique similar to that used by Schmitt et al. (1996a) for their EUVE spectra. The spectrum is assumed to consist of the background b and of M discrete emission lines. The treatment of the background b is described in Sect. 4.4.1. Each line j is assumed to be represented by a normalized profile $g_j(\lambda;\lambda_j,\sigma_j)$, e.g. a Gaussian profile

$$g_j(\lambda;\lambda_j,\sigma_j) = \frac{1}{\sqrt{2\pi}\sigma_j} \mathrm{e}^{-\frac{(\lambda-\lambda_j)^2}{2\sigma_j^2}} \tag{6}$$

with the dispersion σ_j and the central wavelength λ_j. The assumption of a Gaussian line profile is of course arbitrary. Strong isolated emission lines (like O VIII Ly$_\alpha$) can be fitted quite well with such a model, and other analytical models can easily be incorporated into our scheme. Let the observed spectrum be given on a grid of N bins with wavelength values $\lambda_1 \ldots \lambda_N$. The number of expected counts c_i in the i^{th} bin can then be calculated as

$$c_i = sbg + bg_i + \sum_{j=1}^{M} a_j g_{i,j} \ , \tag{7}$$

where a_j is the total number of counts of line j and $g_{i,j}$ is the value of the profile function for line j in bin i. In order to compare the modeled spectrum c_i with a measured spectrum n_i, we assume n_i to be a Poisson realization of c_i. The total probability of the observations $n_1 \ \ldots \ n_N$ is then given by

$$P(n_1 \ \ldots \ n_N) = \prod_{i=1}^{N} e^{-c_i} \frac{c_i^{n_i}}{n_i!} \tag{8}$$

and the likelihood function $\mathcal{L}(a_j,\lambda_j,\sigma_j, j = 1 \ldots N)$ is defined as

$$\mathcal{L} = -2 \ \ln P = -2 \sum_{i=1}^{N} (-c_i + n_i \ln c_i) + const \ . \tag{9}$$

The best-fit values of the parameters a_j, λ_j and σ_j ($j = 1 \ \ldots \ N$) are determined by finding extremal values of $\mathcal{L}$ through:

$$\frac{\partial \ln \mathcal{L}}{\partial a_j} = 0 \, , \qquad \frac{\partial \ln \mathcal{L}}{\partial \lambda_j} = 0 \, , \qquad \frac{\partial \ln \mathcal{L}}{\partial \sigma_j} = 0 \, . \tag{10}$$

The physical meaning of the fit parameters a_j, λ_j and σ_j is quite different. λ_j and σ_j are in principle fixed by the wavelengths of the considered lines and the instrumental resolution, complications arise from possible wavelength calibration errors and line blends. On the other hand, the amplitudes a_j, proportional to the line flux, are the genuine interesting parameters. Analysis of the likelihood equations shows that for the amplitude a_j a fixed point equation can be derived for each line j with λ_j and σ_j assumed to be given:

$$a_{j,new} = \sum_{i=1}^{N} n_i \frac{a_{j,old} g_{i,j}}{c_{i,old}} \ . \tag{11}$$

Eq. 11 can be efficiently solved by iteration. In order to find optimum values for the wavelengths λ_j and linewidths σ_j, we seek minimal values of $\mathcal{L}$ by ordinary minimization procedures. In this process the wavelengths λ_j can vary either freely, or – if the wavelengths of the lines to be fitted are all known – the wavelength differences between the individual lines in a multiplet can be kept fixed in order to account for possible shifts of the overall wavelength scale. Similarly, the line widths σ_j can either vary freely or be fixed, and in such a way blended lines can be described. In this fashion an optimal value for $\mathcal{L}$ is obtained, and the parameters a_j, λ_j (if fitted) and σ_j (if fitted) represent our best fit measurements of these values. Measurement errors are determined by assuming the likelihood curve $\mathcal{L}(a_j)$ to be parabolic and finding the value of Δa_j where $\mathcal{L}(a_j \pm \Delta a_j) = \mathcal{L}(a_j) + \mathrm{d}\mathcal{L}$ resulting in $\Delta a_j = \sqrt{2\Delta\mathcal{L}/\mathcal{L}_j''}$ with $\mathcal{L}_j''$ being the second derivative of $\mathcal{L}$ with respect to a_j known from Eqs. 9 and 7. We choose $\Delta\mathcal{L} = 1$ which yields formal 1 σ errors.

Similarly the errors for λ_j and σ_j are calculated. We determine the errors in $\mathrm{d}\lambda_j$ and $\mathrm{d}\sigma_j$ numerically from $\mathcal{L}(\lambda_j)$ and $\mathcal{L}(\sigma_j)$, respectively with $\Delta\mathcal{L} = 1$, i.e. errors being given within 68.3%. Thus formally we treat all other parameters as "uninteresting".

Table 4. Measured line ratios for Capella and Procyon

Capella	λ [Å]	σ [Å]	A [cts]	sbg [cts/Å]	$R_{\rm obs}$ =f/i	$G_{\rm obs} = \frac{\rm i+f}{\rm r}$
O VII						
r	21.62 ± 0.005		3071.2 ± 56.0			
i	21.82 ± 0.007	0.027	544.8 ± 31.4	2997	3.92±0.24	0.87±0.03
f	22.12 ± 0.001		2135.2 ± 51.1			
N VI						
r	28.79 ± 0.003		491.2 ± 31.49			
i	29.1 ± 0.004	0.03	228.2 ± 26.5	3265	1.68±0.23	1.25±0.14
f	29.54 ± 0.003		384.5 ± 29.4			
C V						
r	40.28 ± 0.002	0.026	440.7 ± 26.9			
i	40.72 ± 0.008	0.026	101.3 ± 18.24	1200	1.58±0.36	0.59±0.1
f	41.5 ± 0.005	0.029	160.2 ± 22.37			
Procyon						
O VII						
r	21.6 ± 0.006		731.6 ± 28.7			
i	21.8 ± 0.004	0.027	203 ± 16.8	0	3.21±0.3	1.17±0.08
f	22.1 ± 0.003		652.4 ± 27.3			
N VI						
r	28.8 ± 0.003		200.2 ± 16.8			
i	29.1 ± 0.006	0.03	77.4 ± 12.3	0	1.26±0.26	0.87±0.14
f	29.55 ± 0.005		97.1 ± 13.2			
C V						
r	40.28 ± 0.003	0.03	203.8 ± 17.0			
i	40.75 ± 0.004	0.028	123.1 ± 14.2	0	0.51±0.12	0.92±0.16
f	41.48 ± 0.01	0.046	63.4 ± 13.5			

4.5. Extracted spectra and measured line ratios

With the procedure described in Sect. 4.4 we analyzed the spectra of the He-like triplets of O VII, N VI, and C V for the two stars Capella and Procyon. In Figs. 2 and 3 the measured spectra are plotted with bold line-dotted lines and the best-fit model curve is indicated by a thin solid line. The total background, i.e. the instrumental background and the assumed source continuum background, is shown with a dotted line. The derived best-fit parameters are given in Tab. 4, where we list, for both Capella and Procyon, the derived empirical wavelengths, the line widths and the line strengths (in counts). For reference purposes we also list the source background values used. Extrapolating the instrumental background onto the spectral trace shows that Procyon's source background must be quite small as expected for a low coronal temperature X-ray source. It will therefore be neglected for the purpose of line flux modeling. In Tab. 4 we also list the ratios between forbidden and intercombination line, and that of the sum of intercombination and forbidden line to the resonance line, which are needed for subsequent analysis. Since no significant rotational or orbital line broadening is expected given the even high spectral resolution of our *Chandra* data, the line-width σ was kept fixed for all models assuming that this value described the instrumental resolution. Starting values for the wavelengths were taken from Mewe et al. (1985).

The O VII triplet has the best signal to noise ratio in both stars and is unaffected by any significant contamination from higher orders as can be seen from Fig. 2 and Fig. 3 in the top panel. As far as the N VI triplet is concerned, it is not as isolated as the O VII triplet and requires further analysis. In both Procyon (Fig. 2) and Capella (Fig. 3) additional lines appear. At 28.44 Å a line attributed to C VI is evident for both Capella and Procyon. In order to minimize any possible cross talk, this line was included in the fit. The line at 30 Å seen in the Capella spectrum is interpreted as the second order of the strong Fe XVII line at 15.013 Å; Fe XVII is strong in Capella, but essentially absent in Procyon. A somewhat strange feature can be seen only in the N VI spectrum of Procyon at about 29.3 Å. This is not a line but an instrumental effect which is present only on the negative side of the spectrum.

4.5.1. Analysis of the C V triplet

Contamination with higher order lines makes the analysis of the C V triplet for Capella particularly difficult (cf.,

Table 5. Fit result in the 13 – 14 Å range for Capella. The assumed source background is 5792 cts/Å

Line	λ [Å]	σ [Å]	A [cts]
Ne IX	13.46 ± 0.003	0.025	4373.9 ± 82.92
Fe XIX	13.53 ± 0.001	0.025	4683.4 ± 84.52
Ne IX	13.71 ± 0.004	0.033	3019.9 ± 74.50
Fe XIX	13.8 ± 0.02	0.02	496.6 ± 62.06
Fe XVII	13.83 ± 0.008	0.03	3337.6 ± 77.94

Fig. 3). This is clear since the Capella spectrum contains strong emission in the band between 13 – 14 Å, which appears in third order in the 39 – 42 Å band under consideration for the C V triplet. Specifically, the interfering lines are Ne IX (13.44 Å × 3 = 40.32 Å), Fe XIX (13.52 Å × 3 = 40.56 Å), Ne IX (13.7 Å × 3 = 41.1 Å), Fe XIX (13.795 Å × 3 = 41.385 Å) and Fe XVII (13.824 Å × 3 = 41.472 Å). We modeled the contamination from these five lines by first determining their first order contributions, transforming the fit results to third order. In the transformation the first order intensities are reduced by a factor of 14.1. This reduction factor is obtained by comparison of first and third order of the isolated 15.013 Å line (Fe XVII). Since the contaminating photons are rather energetic, we expect essentially the same reduction factor in the range 13 – 14 Å. The first order fit result is plotted in Fig. 4 and the resulting fit values are listed in Tab. 5. Technically the higher order contamination was treated as an additional nonconstant contribution to the instrumental background. In addition to the C V triplet, another line, Si XII at 40.91 Å, appearing strong in Capella but weaker in Procyon, had to be modeled. The source background was estimated by requiring the lowest count bins to be adequately modeled. The median function could not be applied since there are too many lines in the considered wavelength range. The result of this modeling exercise is shown in Fig. 3 in the bottom panel, where the dotted line, representing the background, is not constant, but heavily influenced by higher order lines. We emphasise that the errors listed in Tab. 4 do not include errors from the fits in the 13 Å band. We point out in particular that the forbidden C V line lies on top of the third order Fe XVII 13.824 Å line, so that any derivation of the forbidden line flux does require an appropriate modeling of the third order contamination. This is especially difficult because the Fe XVII 13.824 Å line is blended with the Fe XIX 13.795 Å line in first order, while in third order this blend is resolved.

The strong emission in the 13 Å regime is mostly due to iron in excitation stages Fe XVII and Fe XIX. Since there is no significant emission from iron in these high excitation stages in the spectrum of Procyon, there is no blending with third order lines in this case. From Fig. 2 it can be seen that the modeling is straightforward for Procyon.

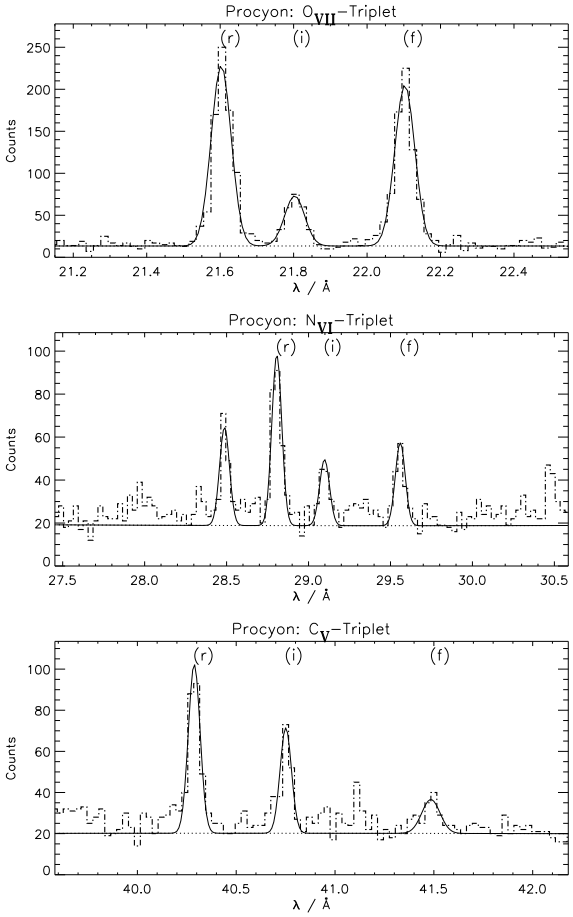

Fig. 2. Spectrum (line-dotted) and fitted (solid) curve for the O VII, N VI, and C V triplet for Procyon. The dotted line represents the total background. The binsize is 0.02 Å for O VII and 0.03 Å for C V and N VI.

5. Results and interpretation

Inspection of our Chandra spectra of Capella and Procyon shows the O VII and N VI forbidden lines to be present in both cases. The C V forbidden line is very weak but present for Procyon, it is also present in Capella despite being significantly contaminated by third order radiation. The observed f/i-ratios for O VII are very close to the expected low-density limit R_0 for both Procyon and Capella, while the measured f/i-ratios for N VI and C V are definitely below the respective values of R_0 in both cases. Before giving a quantitative interpretation of the observed line ratios we must first consider the formation temperature of the studied He-like lines. Especially for the C V triplet the stellar radiation field can contribute significantly to the depopulation of the atomic level from which the forbidden line originates. Low forbidden line intensities can thus also indicate large radiation fields and not necessarily high densities.

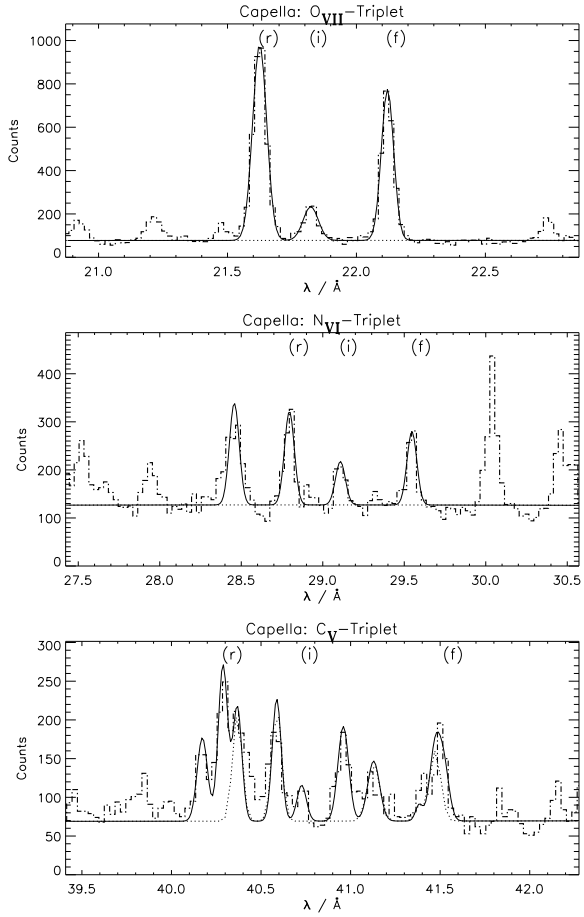

Fig. 3. Spectrum (line-dotted) and fitted (solid) curve for the O VII, N VI, and C V triplet for Capella. The dotted line represents the total background. The binsize is 0.02 Å for O VII and 0.03 Å for C V and N VI.

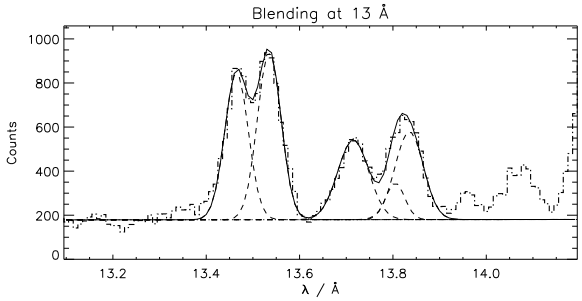

Fig. 4. First order spectrum responsible for third order contamination of the C V triplet of Capella; shown are the data (dash-dotted histogram) as well as the best fit (solid line). Note that the feature near 13.8 Å is actually a line blend (consisting of Fe XIX and Fe XVII contributions) resolved in third order.

Table 6. Temperature diagnostics from ratio of Ly_α/r and from the ratio $G = (i+f)/r$. Values for r and G are taken from Tab. 4 (the G values listed are corrected for effective areas; cf., Tab. 7). For comparison the peak line formation temperature T_m is also given. $T(G)$ is calculated according to Porquet et al. (2001).

Ion	λ [Å]	Procyon [cts]	Capella [cts]
C VI (cts)	33.75	697.5 ± 28.1	2151.1 ± 51.3
C V (cts)	40.27	203.8 ± 17.0	440.7 ± 26.9
C VI/C V		3.42 ± 0.32	4.88 ± 0.41
T(H-He)/MK		1.14 ± 0.03	1.27 ± 0.03
G_{obs}		1.27 ± 0.21	0.81 ± 0.14
$T(G)$/MK		0.32 ± 0.15	0.98 ± 0.43
T_m/MK		1.0	1.0
N VII (cts)	24.8	206.9 ± 16.95	2280.3 ± 53.6
N VI (cts)	28.79	200.2 ± 16.8	491.2 ± 31.49
N VII/N VI		1.03 ± 0.12	4.64 ± 0.41
T(H-He)/MK		1.5 ± 0.05	2.5 ± 0.08
G_{obs}		0.93 ± 0.16	1.33 ± 0.15
$T(G)$/MK		1.25 ± 0.60	0.47 ± 0.17
T_m/MK		1.4	1.4
O VIII (cts)	18.97	673.2 ± 27.6	14676.8 ± 124.3
O VII (cts)	21.6	731.6 ± 28.7	3071.2 ± 56
O VIII/O VII		0.92 ± 0.05	4.78 ± 0.13
T(H-He)/MK		2.13 ± 0.03	3.4 ± 0.03
G_{obs}		1.21 ± 0.08	0.90 ± 0.03
$T(G)$/MK		1.0 ± 0.16	2.01 ± 0.16
T_m/MK		2.0	2.0

5.1. Formation temperature of lines

For the purpose of density diagnostics it is customary to assume that all of the emission is produced at a single temperature T_m (cf., Tab. 2), which corresponds to the peak of the contribution function of the considered line, the so-called formation temperature. It should be kept in mind, however, that He-like ions are present over a relatively broad temperature range, and therefore this assumption might be poor if steep emission measure gradients are present. The measured value of G is also a temperature diagnostics, although optical depth effects in the resonance line may contribute (cf., Acton (1978)); the relevance of optical depth effects to our results is analyzed in section 5.4. In Tab. 6 we show the temperatures T(G) determined from converting the observed G_{obs} values into temperatures according to Porquet et al. (2001) using an electron density of $n_e = 5 \cdot 10^9$ cm^{-3}. We also determined temperatures by studying the line ratio between the observed Ly_α lines of O VIII, N VII, and C VI and the r-lines of O VII, N VI, and C V respectively by assuming isothermal plasma emission. We assume plasma emissivities as calculated in the codes MEKAL (Mewe et al. (1985), Mewe et al. (1995)) and SPEX (Kaastra et al. 1996). The thus obtained fluxes are multiplied with effective areas (cf., Tab. 7) before comparison with the measured ratios. The results are listed in Tab. 6 as T(H-He).

Table 7. Effective areas of the detector at the designated wavelengths. The values are taken from In-Flight Calibration by Deron Pease (9 March 2000).

element	λ / Å	$A_{\rm eff}$ / cm^2		
		λ_+	λ_-	total
C VI	33.76	5.09	5.09	10.18
C V (r)	40.28	2.34	2.34	4.68
C V (i)	40.74	1.65	1.65	3.30
C V (f)	41.5	1.76	1.76	3.52
N VII	24.8	7.76	7.75	15.51
N VI (r)	28.8	6.34	6.33	12.67
N VI (i)	29.1	6.16	6.15	12.31
N VI (f)	29.54	5.80	5.79	11.59
O VIII	18.98	10.08	10.70	20.78
O VII (r)	21.62	6.47	7.05	13.52
O VII (i)	21.82	6.36	6.94	13.30
O VII (f)	22.12	6.22	6.81	13.03

Table 8. Investigation of the influence of the stellar radiation field. Measured fluxes from the IUE satellite F_λ are converted to intensity I_λ taking into account limb darkening effects using ϵ from Tab. 1.

	C V	N VI	O VII
$\lambda_{\rm f\to i}$/Å	2272	1900	1630
$I_{\rm pot}$/eV	392.1	552.1	739.3
Capella			
$F_\lambda/(10^{-11}\frac{\rm ergs}{\rm cm^2\,s\,Å})$	2 ± 0.5	1.2 ± 0.5	0.25 ± 0.05
$I_\lambda/(10^4\frac{\rm ergs}{\rm cm^2\,s\,Å\,strd})$	1.98 ± 0.5	1.19 ± 0.3	0.25 ± 0.5
$T_{\rm rad}$/K	4585 ± 100	4976 ± 150	5029 ± 50
$\phi/\phi_{\rm c}$	2.54 ± 0.86	0.2 ± 0.1	0.003 ±0.0005
Procyon			
$F_\lambda/(10^{-11}\frac{\rm ergs}{\rm cm^2\,s\,Å})$	15 ± 4	7 ± 3	0.6 ± 0.3
$I_\lambda/(10^4\frac{\rm ergs}{\rm cm^2\,s\,Å\,strd})$	21 ± 5	9.8 ± 4	0.84 ± 0.4
$T_{\rm rad}$/K	5532 ± 150	5778 ± 200	5406 ± 300
$\phi/\phi_{\rm c}$	26.67 ± 9.3	1.58 ± 0.84	0.01 ± 0.015
$\phi_{\rm c}/({\rm s}^{-1})$	34.6	148	717

As can be seen from Tab. 6, the temperatures T(G) and T(H-He) do not agree. This is not surprising given the fact that we are likely dealing with a temperature distribution. For Procyon the temperatures T(H-He) agree quite well with T_m, while T(G) agrees with T_m only for N VI. For Capella the respective temperatures T(H-He) always exceed those found for Procyon, while the T(G) temperature derived from N VI is below that found for Procyon. We tentatively conclude that the observed N VI and O VII emission in Capella has significant contributions from plasma at temperatures away from the peak in the line emissivity curve, while for Procyon the emission appears to come from rather close to the line emissivity peak.

5.2. Influence of the stellar radiation field

The observed C V line ratios are particularly interesting. While the observed value for Capella agrees well with the solar observations (cf., Austin et al. (1966), Freeman & Jones (1970)), the observed value for Procyon is rather small. The important point to keep in mind in this context is that Procyon and Capella are stars with different properties compared to the Sun. Procyon is of spectral type F5V-IV (cf., Tab. 1) with an effective temperature of 6500 K, Capella is a spectroscopic binary, the components of which are of spectral type G1 and G8; occasionally the brighter component is also classified as F9. Strictly speaking, what really matters is the effective temperature of the radiation field at the wavelength corresponding to the energy difference between forbidden and intercombination line levels, i.e., 2272 Å for C V (cf., Tab. 8) for the transition $2\ ^3P \to 2\ ^3S$. We investigated the stellar surface radiation fluxes from measurements obtained with the International Ultraviolet Explorer satellite (IUE). We first determined continuum fluxes from archival IUE data, and converted these fluxes into intensities using the expression

$$I_\lambda = F_\lambda \frac{d^2}{R^2}\frac{1}{2\pi(1-\frac{\epsilon}{2})}, \tag{12}$$

where ϵ is the (linear) limb darkening coefficient. It is determined from Díaz-Cordovés et al. (1995) using $\log g$ and $T_{\rm eff}$ listed in Tab. 1; d and R are distance and radius of the sample stars as listed in Tab. 1. For the case of the binary system Capella we assumed the worst case and attributed all emission to the Ab component, i.e., the star with the higher radiation temperature. The other component Aa (G8/K0 III) is about equally bright in the corona as G1 III (cf., Linsky et al. (1998)), but much weaker in the chromosphere and transition region. From the thus obtained value for the intensity a radiation temperature $T_{\rm rad}$ can be inferred from the appropriate Planck curve, expressed as

$$u_\nu = W\frac{8\pi h\nu^3}{c^2}\frac{1}{\exp\left(\frac{h\nu}{kT_{\rm rad}}\right)-1}, \tag{13}$$

where W is the dilution factor of the radiation field (we take $W=\frac{1}{2}$ close to the stellar surface). The results derived from these data are listed in Tab. 8.

In order to compute the dependence of $\phi/\phi_{\rm c}$, required in Eq. 2, on $T_{\rm rad}$ we use the calculations by Blumenthal et al. (1972), who derive the expression

$$\frac{\phi}{\phi_{\rm c}} = \frac{3(1+F)c^3}{8\pi h\nu^3}\frac{A(2^3P\to 2^3S)}{A(2^3S_1\to\ 1^1S_0)}u_\nu \tag{14}$$

with $\phi_{\rm c} = A(2^3S_1\to\ 1^1S_0)/(1+F)$, transition probabilities $A(i\to j)$, and u_ν the spectral energy density at the

appropriate $2^3P_1 \rightarrow 2^3S_1$ frequency ν. The factor 3 is the ratio of the statistical weights of the levels 2^3P and 2^3S. F is approximated by Blumenthal et al. (1972) through

$$F(\xi) = \frac{3\xi H(\xi) exp(\xi/4) + 1.2\xi + 2H(\xi) + 2}{3\xi exp(\xi/4) + 0.6\xi H(\xi) + H(\xi) + 1}, \quad (15)$$

where

$$H(\xi) = \frac{C(1^1S \rightarrow 2^3S)}{C(1^1S \rightarrow 2^3P)}, \quad (16)$$

with $\xi = I/kT_{\rm rad}$ and the collisional excitation rate coefficients $C(i \rightarrow j)$. The ionization potentials $I_{\rm pot}$ for the ions C V, N VI, and O VII are taken from Pradhan & Shull (1981). The collisional excitation rate coefficients $C(i \rightarrow j)$ were taken from Pradhan et al. (1981) for C V and O VII while the rate coefficients for N VI were obtained by interpolation from these values.

From Eq. 14 we determine the values used in Eq. 2 for the calculation of the theoretical curves in Fig. 5. They are also listed in Tab. 8. For comparison, we also give in Tab. 8 the values derived from recent calculations by Porquet et al. (2001) considering a multi-level model previously used by Porquet & Dubau (2000), and taking into account the effect of temperature on G and $R(n_e)$ (Porquet et al. (2001), see also Porquet & Dubau (2000)).

5.3. Analysis and interpretation

In Fig. 5 we show for Procyon and Capella the expected line ratio f/i as a function of the electron density $n_{\rm e}$ in comparison with the observed line ratio $R_{\rm obs}$ (corrected for detector efficiencies) and its 1σ error. The expected curves are plotted for the radiation temperature range estimated for the two stars as listed in Tab. 8; for O VII the stellar radiation field does not significantly influence the f/i ratio as expected. We used the formation temperatures $T(G)$ calculated from the G ratios as listed in Tab. 6, thus assuming all the emission being produced at a single temperature. In Tab. 9 we summarize the derived densities and their 1σ errors for Procyon and Capella not accounting for errors in $T(G)$. No density values could be determined for the C V triplet in Procyon and for the O VII triplet in Capella. Instead we give upper limits for the two cases (Tab. 9); for Capella only a 2σ upper limit could be determined.

Obviously, for both stars the measured line ratios are within (Capella) and very close to (Procyon) the low-density limit R_0. At any rate, the measured f/i ratio is larger for Capella than for Procyon, so one arrives at the somewhat unexpected conclusion that the coronal density in the active star Capella should be smaller than in the inactive star Procyon.

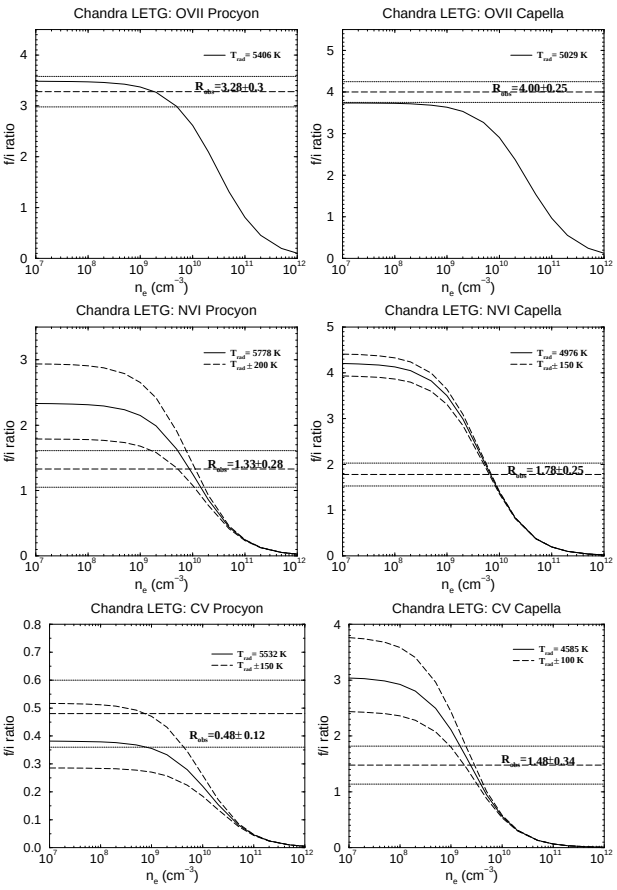

Fig. 5. Theoretical curves in the radiation temperature range given in Tab. 8 in comparison with the measured value of $R_{\rm obs}$ for the O VII, N VI and the C V triplet for Capella and Procyon. The measured R values from Tab. 4 are corrected for detector efficiencies.

Table 9. Results of density diagnostics

log $n_{\rm e}$/cm^{-3}	**Capella**	**Procyon**
C V	9.42 ± 0.21	<8.92
N VI	9.86 ± 0.12	9.96 ± 0.23
O VII	<9.38 (2σ upper limit)	$9.28^{+0.4}_{-9.28}$

5.4. Optical depth effects

In all of the above analysis we assumed all triplet lines to be optically thin. In the following section we show this assumption to be consistent with our results. Let us therefore assume that the optical depth in the resonance lines is not small. This leads to a reduction of the measured resonance line flux due to radiative scattering. At line center the optical depth is given by the equation

$$\tau = 1.2\ 10^{-17} \left(\frac{n_i}{n_{el}}\right) A_z \left(\frac{n_H}{n_e}\right) \lambda\ f \sqrt{\frac{M}{T}} n_e \ell \quad (17)$$

(Schrijver et al. 1994) with the fractional ionization is denoted by n_i/n_{el}, the elemental abundances by A_z, the ratio of hydrogen to electron density is $n_H/n_e = 0.85$, the oscillator strength $f = 0.7$ for all ions, the atomic number is M, the wavelength λ is measured in Å, the temperature T in K, the electron density n_e in cm^{-3} and the mean free path is denoted by ℓ. In Eq. 17 we adopt a value of unity for the fractional ionization and use the solar abundances. We further assume T at the peak line formation and note, that τ is rather insensitive to the precise value of T. We can determine – for each resonance line – that value of $n_e\ell$ which yields an optical depth of unity. Adopting a maximum value of n_e of 10^{10} cm^{-3} (cf. Tab. 9), we determine lower values of ℓ of $1.3\,10^{12}$ cm, $5.6\,10^{12}$ cm and $6.0\,10^{11}$ cm, for O VII, N VI and C V, respectively. Assuming a geometry most suitable for resonance scattering, we can compute the respective emission measures of $n_e^2\ell^3$ respectively. Comparing these emission measures with those derived from the measured line fluxes f_λ

$$EM = \frac{4\pi d^2 f_\lambda}{p_\lambda(T)} \tag{18}$$

with the line cooling function $p_\lambda(T)$ and the distance d (cf. Tab.1), shows the former to be larger by a few orders of magnitude for both stars. This inconsistency shows that the assumption of a non-negligible optical depth is invalid and we conclude that optical depth effects are irrelevant for the analysis of He-like triplets in Procyon and Capella.

6. Conclusions

6.1. Comparison with the Sun

Both Capella and Procyon are considered to be solar-like stars. In the solar context the He-like triplets of oxygen, nitrogen and carbon have been known for a long time and in fact the He-like ion density diagnostics have been first developed to interpret these solar data. Many solar observations are available for the O VII triplet, while only very few observations have been made for the N VI and C V triplets. The first observations of the C V triplet are reported by Austin et al. (1966), who obtained an f/i-ratio of 1.9, while Freeman & Jones (1970) found an f/i-ratio of 1.0. The latter authors also observed the N VI triplet, but failed to detect the intercombination line and hence deduced $f/i > 1.9$. Brown et al. (1986) observed the C V and N VI triplets during a flare and found a mean value of $f/i \approx 2$ with large scatter between $0.1-4$ around this mean for N VI and a value of 0.21 (with a scatter between $0.17-0.25$) for C V. In consequence, little can be said about the solar N VI line ratios because of the large measurement errors. The measured ratios for both Capella and Procyon are certainly consistent with the range of N VI f/i values quoted by Brown et al. (1986). As far as C V is concerned, the flare data yield very low f/i ratios indicative of high densities. The C V f/i ratio observed for Capella is higher, and that for Procyon – still higher than that observed for the Brown et al. (1986) flare – we argue is due to large photospheric radiation fluxes. We therefore conclude that the layers contributing the C V emission in Capella and Procyon are at lower density than those encountered in solar flares, and the same applies to the layers emitting N VI.

Observations of the O VII triplet in the solar corona are reported by Freeman & Jones (1970), McKenzie et al. (1978), McKenzie et al. (1982), all of which refer to the quiescent corona, while some of the observations from McKenzie et al. (1982) and Brown et al. (1986) refer to flares and those of Parkinson (1975) refer to active regions. In addition we considered some data points collected from various sources cited by Doyle (1980). In Fig. 6 we plot G vs. R of these solar observations and compare these solar data with our *Chandra* measurements for Procyon and Capella. For clarity we omitted individual error bars, which are typically $0.1-0.3$ for the solar measurements. As can be seen from Fig. 6, most of the solar measurements yield R value between 3 and 4. A few values are significantly lower around R $\approx$ 2, with all them referring to flares or active regions. Our *Chandra* measurements (3.28 for Procyon, 4.0 for Capella) thus fall into the bulk part of the solar data. Unfortunately, the solar data are by no means unambiguous. It is not always clear which regions the data refer to (except for the flare observations by Brown et al. (1986)), and further, most of the observations are relatively old and have not been taken with high spatial resolution; they are comparable in some sense to our full disk observations of stellar X-ray sources. In addition, the instrumentation used in different experiments is quite different and each experiment is affected by its own specific difficulties. Nevertheless it seems fair to state that most O VII measurements referring to quiescent conditions are close to the low density limit, thus indicating that the physical properties of the O VII emitting layers in Capella and Procyon should not be that different from those in the Sun; a little puzzling in this context is the large scatter of the solar G data. In contrast, the solar flare data (R $\sim$ 2) is much lower than any of the other measurements, consistent with a high density plasma.

6.2. Comparison between Procyon and Capella

Inspection of Tab. 9 suggests that $n_{Procyon} \geq n_{Capella}$ for the densities derived from C V, N VI, and O VII; there is definitely no evidence for $n_{Procyon} < n_{Capella}$. These findings are in contradiction to the claims made by Dupree et al. (1993), who argue on the basis of Fe XXI line ratios measured with the EUVE satellite that $n_{Capella} \sim 10^{13}$ cm^{-3}. A recent analysis of the long wavelength part ($\lambda > 90$ Å) of the LETGS spectrum of Capella by Mewe et al. (2001), however, yielded plasma densities of 5×10^{12} cm^{-3} at most for the plasma emitting in the Fe XXI lines with no evidence for any deviations from the low density limit. Of course, these values refer to those

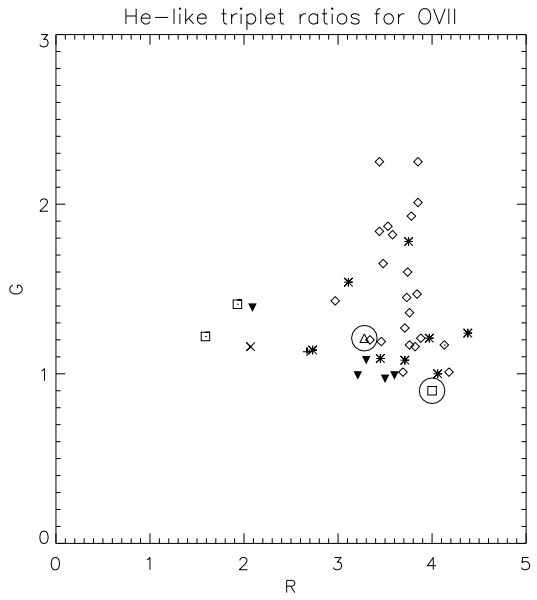

Fig. 6. Measurements of solar values for He-like ratios of O VII:
Freeman & Jones (1970) (dotted open box),
McKenzie et al. (1982): quiescent (diamond), flare (asterix),
McKenzie et al. (1978) (dotted diamond),
Doyle (1980) (filled triangle upside down),
Parkinson (1975): active region (plus symbol),
Brown et al. (1986): flare (cross).
Encircled are our measurements of Procyon (open triangle) and Capella (open box).

plasma layers emitting in the Fe XXI line, which ought to be at far higher temperature ($\approx$ 8 MK) than those emitting in the C V, N VI, and O VII lines (1 – 2 MK). If we assume all the observed emissions to come from the same magnetically confined structures (loops), one expects the gas pressure to be more or less constant and hence the density at lower temperatures even higher. However, plasma densities (for Capella) of $\approx 10^{13}$ cm^{-3} at temperatures of 2 MK are clearly inconsistent with our LETGS spectra. Therefore the plasma emitting in the Fe XXI line is either at the low density limit or the Fe XXI emission comes from different structures than the emissions from He-like ions.

Our temperature measurements of the line forming regions (cf., Tab. 6) are not fully conclusive, although they suggest that the same lines of C V, N VI, and O VII respectively are formed at a somewhat higher temperature (at most a factor of 2) in Capella as compared to Procyon. As a consequence we must have $p_{Procyon} \approx p_{Capella}$ for the gas pressures in the respective line forming regions. Capella's peak coronal temperature is clearly much higher than Procyon's. If we again assume – going along with the solar analogy – that for both Procyon and Capella (all of) the X-ray emission originates from magnetically confined plasma loops, the loop top temperatures in Capella must be higher than in Procyon. The loop scaling laws then imply for the typical loop length scales L for Procyon and Capella $\frac{L_{Capella}}{L_{Procyon}} = (\frac{T_{max,Capella}}{T_{max,Procyon}})^3$. A conservative estimate yields $\frac{T_{max,Capella}}{T_{max,Procyon}} > 2$, thus $L_{Capella} \geq 8\ L_{Procyon}$. The conclusion then appears inescapable that the typical sizes of the magnetic structures in Procyon and Capella are quite different by probably at least one order of magnitude.

Next, it is instructive to compare the total mean surface fluxes emitted in the helium- and hydrogen-like ions of carbon, nitrogen and oxygen for Procyon and Capella. Using the measured count ratios and correcting for the effects of distance, exposure times and the surface areas of the stars we find for the C V, C VI, N VI, N VII, O VII, and O VIII lines values of (Capella)/(Procyon) of 0.96, 1.37, 1.09, 4.9, 1.87, and 9.71 respectively. Therefore up to those temperatures where the C V, C VI, and N VI lines are formed, the mean surface fluxes in the two stars hardly differ at all; pressures and temperatures are also quite similar. We therefore conclude that the physical characteristics and global properties (such as filling factor) of Procyon's and Capella's corona at a level of $T \sim 10^6$ K are very similar.

It is interesting to again perform a comparison to the Sun. Freeman & Jones (1970) quote – for their SL801 rocket flight on Nov 20 1969 – resonance line fluxes of 4.2 10^{-3}, 2.1 10^{-3}, and 3.1 10^{-3} erg/(cm^2 sec) for O VII, N VI, and C V respectively. Correcting for the distance between Earth and Sun we find average surface fluxes of 200, 100, and 150 erg/cm^2/sec for O VII, N VI, and C V respectively on the solar surface. Carrying out the same calculation for our *Chandra* data, we find – using the effective areas given in Tab. 7 – mean surface fluxes in O VII of 3700 and 1980 erg/(cm^2 sec), in N VI of 480 and 430 erg/(cm^2 sec), and in C V of 830 and 860 erg/(cm^2 sec) for Capella and Procyon respectively. We therefore recover our previous finding that Capella's and Procyon's surface fluxes are quite similar, and determine in addition that both stars exceed typical (?) solar values by one order of magnitude. Since the physical conditions of the line emitting regions are quite similar, we conclude that the coronal filling factors are larger.

Evaluating now the coronal pressure for Procyon we find – using the densities and temperatures derived from N VI – p(N VI) = 4.4 dyn/cm^2, a value also very typical for solar active regions. From the loop scaling law (Rosner et al. (1978)) $T_{max} = 1.4 \times 10^3 (pL)^{(1/3)}$ we deduce a typical length of 2.7×10^8 cm using $T_{max} = 1.5 \times 10^6$ K. This value must be considered as a lower limit to the probable length scale because of the unfortunate sensitive dependence of L on T_{max} through $L \sim T_{max}^3$; T_{max} is likely somewhat higher than $T_{max} = 1.5 \times 10^6$ K as suggested by the temperatures derived from the O VIII data. At any rate, however, the conclusion is, that the X-ray emission originates from low-lying loops and hence also our *Chandra* data support the view that Procyon's corona has an appearance very similar to the Sun's, just like the conclusion drawn by Schmitt et al. (1996b) from their EUVE spectra. It then follows that the sizes of the

magnetic loops in Procyon's corona are similar to the loops found in the solar corona. Adopting – for argument's sake – a characteristic length of $L_{Proc} = 1\times10^9$ cm, we then find for Capella $L_{Capella} > 8\times10^9$ cm, and possibly even a significant fraction of Capella's radius. This result is somewhat puzzling. On the Sun, loop structures, i.e., magnetically closed topologies, are occasionally found at larger heights, but they are always of low density and they never contribute significantly to the overall X-ray emission. It will be interesting to see whether this behavior is typical for active stars in general, or whether it applies only to Capella. After all, Capella may not be the prototypical active star. Its corona is not as hot as that of other stars, it does not produce flares and its radio emission is very weak.

Acknowledgements. We thank Tom Ayres, U/COLORADO (CASA), for very useful discussion. J.-U. N. acknowledges financial support from Deutsches Zentrum für Luft- und Raumfahrt e.V. (DLR) under 50OR98010.
The Space Research Organization Netherlands (SRON) is supported financially by NWO.

References

Acton L.W., 1978, ApJ 255, 1069
Austin W.E., Purcell J.D., Tousey R., & Widing K.G., 1966, ApJ 145, 373
Blumenthal G.R., Drake G.W., & Tucker W.H., 1972, ApJ 172, 205
Brinkman A.C., Gunsing C.J.T., Kaastra J.S., et al., 2000, ApJ 530, L111
Brown W.A., Bruner M.E., Acton L.W., et al., 1986, ApJ 301,981
Catura R.C., Acton L.W., & Johnson H.M., 1975, ApJL 196, L47
Díaz-Cordovés J., Claret A., & Giménez A., 1995, A&AS 110, 329
Doyle J.G., 1980, A&A 87, 183
Drake J.J., Laming J.M., Widing K.G., 1995, ApJ 443, 393
Dupree A.K., Brickhouse N.S., Doschek G.A., et al., 1993, ApJL 418, L41
Freeman F.F. & Jones B.B., 1970, Sol. Phys. 15, 288
Fuhrman K., Pfeiffer M., Frank C., et al., 1997, A&A 323, 909
Gabriel A.H. & Jordan C., 1969, MNRAS 145, 241
Hummel C.A., Armstrong J.T., Quirrenbach A., et al., 1994, ApJ 107, 1859
Hünsch M., Schmitt J.H.M.M., & Voges W., 1998a, A&AS 127, 251
Hünsch M., Schmitt J.H.M.M., & Voges W., 1998b, A&AS 132, 155
Irwin A.W., Fletcher J.M., Yang S.L.S., et al., 1992, PASP 104, 489
Kaastra J.S., Mewe R., Nieuwenhijzen H., 1996, in UV and X-ray Spectroscopy of Astrophysical and Laboratory Plasmas, K. Yamashita and T. Watanabe (eds.), Tokyo, Universal Academy Press, Inc., p. 411 (SPEX)
Kelch W.L., Linsky J.L., Basri G.S., et al., 1978, ApJ 220,962
Lemen J.R., Mewe R., Schrijver C. J., et al., 1989, ApJ 341, 474
Linsky L.L., Wood B.E., Brown A., et al. 1998, ApJ 492, 767
McKenzie D.L., Rugge H.R., Underwood J.H., et al. 1978, ApJ 221, 342
McKenzie D.L. & Landecker P.B., 1982, ApJ 259, 372
Mewe R. & Schrijver, J., 1978, A&A 65, 114
Mewe R., Heise J., Gronenschild E.H.B.M., et al. 1975, ApJL 202, L67
Mewe R., Gronenschild E.H.B.M., Westergaard N.J., et al., 1982, ApJ 260, 233
Mewe R., Gronenschild E.H.B.M., & van den Oord G.H.J., 1985, A&AS 62, 197
Mewe R., Schrijver C.J., Lemen J.R., et al., 1986, Advances in Space Research 6, 133
Mewe R., Kaastra J.S., & Liedahl D.A., 1995, Legacy 6, 16 (MEKAL)
Porquet D., Mewe R., Dubau J., et al. 2001, A&A 376, 1113
Mewe R., Raassen A.J.J., Drake J.J., et al., 2000b, A&A 368, 888
Parkinson J.H., 1975, Sol. Phys. 42, 183
Porquet & Dubau 2000, A&AS 143, 495
Pradhan A.K., 1982, ApJ 263, 477
Pradhan A.K., 1985, ApJ 288, 824
Pradhan A.K., Norcross D.W., & Hummer D.G., 1981, ApJ 246,1031
Pradhan A.K., Shull J.M., 1981, ApJ 249,821
Predehl P., Braeuninger H., Brinkman A., et al., 1997, Proc. SPIE 3113, 172
Rosner R., Tucker W.H., & Vaiana G.S., 1978, ApJ 220, 643
Schmitt J.H.M.M., Harnden F.R., Jr., Rosner R., et al., 1985, ApJ 288, 751
Schmitt J.H.M.M., Haisch B.M., & Drake J.J., 1994, Science 265, 1420
Schmitt J.H.M.M., Drake J.J., Stern R.A., et al., 1996a, ApJ 457, 882
Schmitt J.H.M.M., Drake J.J., Haisch B.M., et al., 1996b, ApJ 467, 841
Schmitt J.H.M.M., 1997, A&A 318, 215
Schrijver, C.J., van den Oord G.H.J., & Mewe R., 1994, A&AL. 289, L23
Schrijver, C.J., van den Oord G.H.J., Mewe R., et al., 1995, A&A 302, 438
Vaiana G.S., Cassinelli J.P., & Giacconi R., 1981, ApJ 244, 163
Vedder P.W., & Canizares C.R., 1983, ApJ 270, 666

Chapter 4

Analysis of a *Chandra* LETGS spectrum of Algol

Submitted for publication in: Astronomy and Astrophysics

Astronomy & Astrophysics manuscript no.
(will be inserted by hand later)

Chandra LETGS Observation of the Active Binary Algol

J.-U. Ness[1], J.H.M.M. Schmitt[1], V. Burwitz[2], R. Mewe[3], and P. Predehl[2]

[1] Universität Hamburg, Gojenbergsweg 112, D-21029 Hamburg, Germany
[2] Max-Planck-Institut für Extraterrestrische Physik (MPE), Postfach 1603, D-85740 Garching, Germany
[3] Space Research Organization Netherlands (SRON), Sorbonnelaan 2, 3584 CA Utrecht, The Netherlands

received January 24, 2002; accepted ...

Abstract. A high-resolution spectrum obtained with the low-energy transmission grating onboard the Chandra observatory is presented and analyzed. Our analysis indicates very hot plasma with temperatures up to $T \approx 15 - 20\,\mathrm{MK}$ from the continuum and from ratios of hydrogen-like and helium-like ions of Si, Mg, and Ne. In addition lower temperature material is present since O VII and N VI are detected. However, no C VI is found. Two methods for density diagnostics are applied. The He-like triplets from N VII to Si XIII are used and densities around $10^{11}\,\mathrm{cm}^{-3}$ are found for the low temperature ions. Taking the UV radiation field from the B star companion into account, we find that the low-Z ions can be affected by the radiation field quite strongly, such that densities of $3 \times 10^{10}\,\mathrm{cm}^{-3}$ are also possible, but only assuming that the emitting plasma is immersed in the radiation field. For the high temperature He-like ions only low density limits are found. Using ratios of Fe XXI lines produced at similar temperatures are sensitive to lower densities but again yield only low density limits. We thus conclude that the hot plasma has densities below $10^{12}\,\mathrm{cm}^{-3}$. Assuming a constant pressure corona we show that the characteristic loop sizes must be small compared to the stellar radius and that filling factors below 0.1 are unlikely.

Key words. Atomic data – Atomic processes – Techniques: spectroscopic – Stars: individual: Algol – stars: coronae – stars: late-type – stars: activity – X-rays: stars

1. Introduction

Stellar coronae cannot be spatially resolved, yet they are thought to be highly structured just like the solar corona, whose X-ray emission comes almost exclusively from hot plasma confined in magnetic loops. So far the only way to infer structural information in such unresolved stellar point sources has been via eclipse studies in suitably chosen binary systems. Observations of the X-ray light curve can yield information on the location of the X-ray emission (Preś et al. 1995), although the eclipse mapping reconstruction problem is highly under-determined; after all, one is trying to reconstruct a three-dimensional intensity distribution from a one-dimensional light curve. Among a variety of problems discussed in detail by Schmitt (1998), a specific difficulty arises from the fact that in most eclipsing systems both components are known or likely to be X-ray emitters. Obviously the reconstruction problem is easier to solve in those cases where one of the binary components is X-ray dark. At X-ray wavelengths only two such systems have been studied so far, the eclipsing binary systems α CrB (cf. Schmitt & Kürster 1993) and β Per (= Algol; Oord & Mewe 1989).

Send offprint requests to: J.-U. Ness
Correspondence to: jness@hs.uni-hamburg.de

The Algol system actually consists of three components, a close eclipsing binary (containing a B8 main sequence star and a K2IV subgiant) and a more distant F-type star, which is not of interest for our purposes. The stellar parameters of the two stars of the eclipsing binary system (inclination angle is i=81°) are listed in Tab. 1. Algol is one of the strongest coronal X-ray emitters in the soft X-ray band and has been observed with essentially all X-ray satellites flown so far. Particular interest in Algol's X-ray emission arises from the fact that no magnetic dynamos and magnetic activity phenomena should occur on stars of spectral type B8, since such stars are fully radiative and thus the primary component of Algol should be X-ray dark. In consequence, all of Algol's X-ray emission is believed to originate from the cool secondary, which is rapidly rotating because it is tidally locked with the primary on the orbital time scale (2.8 days). We note in passing, however, that there is – in contrast to the totally eclipsing system α CrB (cf. Schmitt & Kürster 1993) – no observational proof for this assumption. Nevertheless, X-ray eclipses at secondary optical minimum are expected, yet not all observations of Algol at secondary minimum yield evidence for such eclipses. For example, a long observation of Algol with the EXOSAT satellite (White et al. 1986) centered on secondary optical minimum showed no

Table 1. Properties of Algol A and B: mass M, radius R, effective temperature $T_{\rm eff}$, log g and spectral type are taken from Richards (1993) and references therein, the limb darkening coefficients ϵ are taken from Díaz-Cordovés et al. (1995).

	Algol A	Algol B
d/pc	28	
$M/M_\odot$	3.7 ± 0.3	0.81 ± 0.05
$R/R_\odot$	2.9 ± 0.04	3.5 ± 0.1
$T_{\rm eff}$/K	13000 ± 500	4500 ± 300
log g	4.08	3.2
Spectr. type	B8V	K2IV
ϵ	0.44	0.95

indication for any eclipse, suggesting the interpretation of a corona with a scale height of more than a stellar radius or a somewhat peculiar configuration of the corona at the time of observation. On the other hand, a long ROSAT PSPC observation (Ottmann & Schmitt 1996) did show evidence for a partial eclipse of the quiescent X-ray emission, demonstrating that a significant fraction of the quiescent X-ray emission is emitted within a stellar radius. A BeppoSAX observation (Schmitt & Favata 1999, Favata & Schmitt 1999) of Algol showed the total eclipse of a long-duration flare, and a sequence of four ASCA observations of Algol at secondary eclipse showed evidence for both eclipses and absence of eclipses at different occasions.

Another method to provide information on structure in spatially unresolved data consists of spectroscopic measurements of density. If the density measurements are combined with the measurement of the volume emission measure EM, an estimate of the emitting plasma volume can be obtained; in an eclipsing binary these volumes will be subject to additional light curve constraints. With the high-resolution spectrometers onboard *Chandra* it is possible to carry out high-resolution X-ray spectroscopy for a wide range of coronal X-ray sources. We have obtained a *Chandra* high-resolution X-ray spectrum of Algol, which allows us to combine the information derived from X-ray light curves and X-ray spectroscopy. We will specifically discuss the Algol spectra obtained with the Low Energy Transmission Grating Spectrometer (LETGS).

2. Instrument description and Observation

The LETGS is a diffraction grating spectrometer covering the wavelength range between 5 – 175 Å (0.07 – 2.5 keV) with a resolution $\lambda/\Delta\lambda \sim 2000$ at the long wavelength end of the band pass; typical instrumental line widths are of the order 0.06 Å (FWHM) (cf., Ness et al. 2001a). A detailed description of the LETGS instrument is presented by Predehl et al. (1997). We note in passing that the LETGS uses a microchannel plate detector (HRC-S) placed behind the transmission grating without any significant intrinsic energy resolution. Thus in contrast to CCD based detectors the energy information for individual counting events is solely contained in the events' spatial location.

Accounting for the instrumental line widths the symmetry of the grating is sufficient to co-add both sides of the spectrum in order to obtain a better SN ratio (Ness et al. 2001a). The thus obtained spectrum is shown in Fig. 1. A rich line spectrum with lines from Fe, Si, Ne, O, N, and C can be recognized between 6 and 30 Å as well as many Fe lines above 90 Å. Strong continuum emission is also apparent almost over the whole observed band pass; we note in passing that the spectrum shown in Fig. 1 has not been corrected for effective areas.

3. X-ray fluxes and light curve

Algol was observed with the above described instrumental setup between March, 12, 2000, 18:36 and March, 13, 2000, 17:13. The total on-time was 81.41 ksec, almost identical to the actual exposure time. During this time 106181 source counts were collected on the negative side and 101469 counts on the positive side. The high spectral resolution of the LETGS allows the computation of incident photon and energy fluxes without the need of any plasma emission model. In particular, since the LETGS wavelength range covers both the ROSAT and the Einstein wavelength ranges we can directly calculate fluxes corresponding to the respective band passes of these instruments without the need of any model. Using only bins with $A_{\rm eff} > 0.1\,{\rm cm}^2$ and the distance d from Tab. 1 we compute a total X-ray luminosity of $1.4\,10^{31}$ erg/s. Restricting the wavelength range to the nominal ROSAT wavelength range (6.2-124 Å), we find $1.1\,10^{31}$ erg/s, within the Einstein band pass we find $1.0\,10^{31}$ erg/s (2.8-62 Å). These numbers can be compared with earlier measurements with these instruments. Berghöfer et al. (1996) report an X-ray flux of $L_X = 0.7\,10^{31}$ erg/s measured with ROSAT. This agrees with our *Chandra* measurement to within 30% so that significant long term variability can be excluded. Ottmann & Schmitt (1996) report an X-ray luminosity of $L_X = 20\,10^{31}$ erg/s during a flare, while their quiescent emission is consistent with the values reported by Berghöfer et al. (1996). Our measurement is therefore well within the range of luminosities found in earlier observations.

In order to compute the ephemeris of Algol, we used the expression $JD_{prim} = 2445739.003 + 2.8673285 \times {\rm E}$ (Kim 1989; E being an integer) for the times of primary minimum. Our *Chandra* observation covers the phases 0.74 to 1.06, i.e., outside optical secondary minimum. In Fig. 2 we show the background-subtracted X-ray light curve of the LETGS data (in the ranges 10 - 120 Å, 10 - 20 Å, 20 - 80 Å, and 80 - 120 Å). As is clear from Fig. 2, the light curve shows a more or less continuous decrease in intensity throughout the *Chandra* observations by a

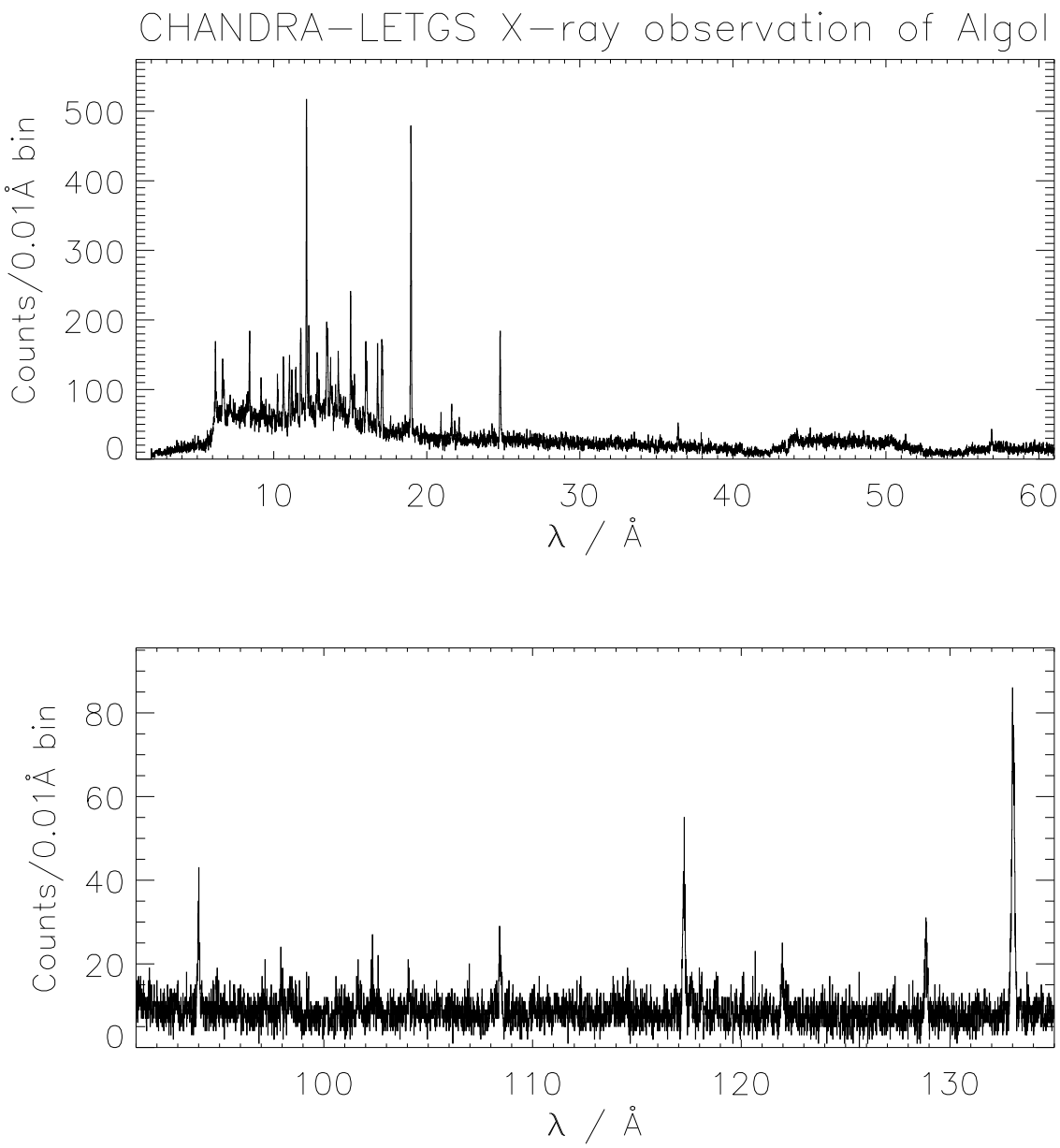

Fig. 1. Top: LETGS spectrum of Algol in the range 1-40 Å. Clearly visible is the strong continuum and many prominent emission lines from Ne, Si, Fe, Mg, N, and O. The Ly$_\alpha$ lines from Mg XII (8.42Å), Ne X (12.14Å), O VIII (18.97Å) and N VI (24.78Å) can be recognized, while C VI (33.75Å) is not visible.
Bottom: Wavelength range from 90-135 Å. Visible are the lines from Fe XVIII at 94 Å from Fe XXI at 117.5 Å and 128.7 Å, and from Fe XXIII/Fe XX at 133Å.

factor of 1.38 (10 - 120 Å), 1.22 (10 - 20 Å), 1.47 (20 - 80 Å), and 1.77 (80 - 120 Å). Phasing of the data suggests the existence of a primary minimum in X-rays, when the late-type star is located in front of the early-type star, but from our discussion above this appears highly unlikely. Since the Algol system is known to be able to produce giant flares, a far more plausible interpretation would be to interpret the X-ray light curve as the "tail" of a long-duration flare, possibly similar to the one observed by Schmitt & Favata (1999) with BeppoSAX. From this assumption we would expect the radiation to become softer in time and to detect a cooling of the plasma. From Fig. 2 no evidence for softening can be deduced, rather the radiation becomes even harder. From the temperature dependent line ratios of the resonance lines of the H-like and He-like ions plotted in Fig. 3 again no evidence for

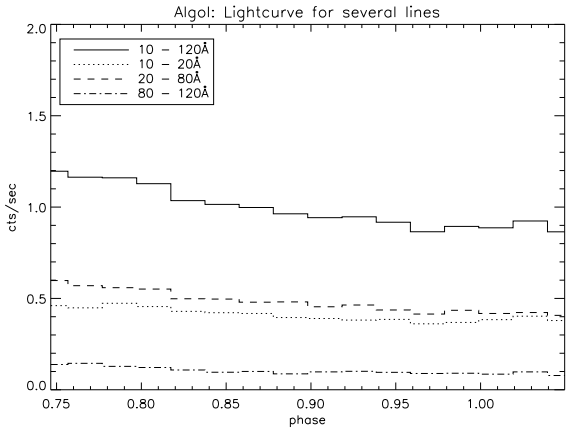

Fig. 2. Light curve of Algol in a hard, medium and a soft energy band.

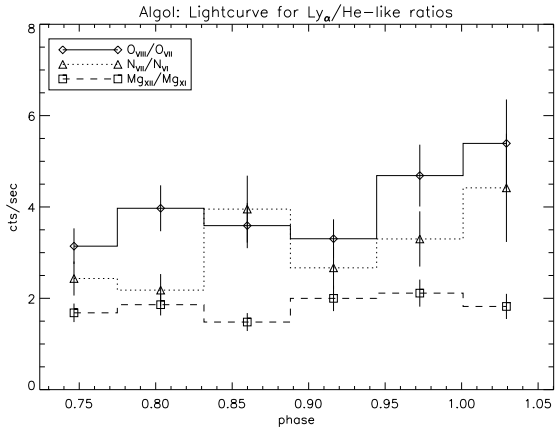

Fig. 3. Light curve of Algol in three different energy bands (top) and development of the temperature dependent ratios of Ly$_\alpha$/He-like resonance line for Oxygen, Nitrogen and Magnesium.

cooling is apparent; the plasma might even become hotter with time, but at a very small rate. For oxygen the ratio raises from 3.6 ± 0.27 to 4.2 ± 0.35, for nitrogen from 2.7 ± 0.25 to 3.3 ± 0.37 and for magnesium from 1.7 ± 0.12 to 2.0 ± 0.16. Thus we find no indication for the "tail" of a long duration flare from this spectral analysis.

4. Data analysis

The data extraction from the HRC-S and analysis of the spectra presented in this paper are identical to the methods described by Ness et al. (2001a). Specifically the spectra are extracted along the spectral trace without any pulse height correction scheme, the background is taken from nearby adjacent regions on the microchannel plate. The two dispersion directions are co-added, but the individual dispersed spectra can still be used to check for inconsistencies in the co-added spectrum. The thus obtained spectrum is shown in Fig. 1.

4.1. Analysis of the continuum

The total spectrum in Fig. 1 shows two components, a multitude of emission lines and a significant continuum. The shape of the continuum suggests thermal bremsstrahlung emission as the dominant continuum emission process. This assumption is supported by the high temperatures measured for Si, Mg, and Fe (cf. Tab. 4). We therefore use the formula

$$\frac{dW}{dV\ dt\ d\lambda} = 2.051 \times 10^{-19} n_e^2 T^{-1/2} \frac{G(\lambda,T)}{\lambda^2} e^{-143.9/(T\lambda)} \quad [\mathrm{erg\,cm^{-3}\,s^{-1}\,\AA^{-1}}] \tag{1}$$

(Mewe et al. 1986) for the specific volume emissivity $\frac{dW}{dV\ dt\ d\lambda}$ to model the continuum. T is the plasma temperature in K and c the speed of light in cm/s. The Gaunt factor $G(\lambda,T) = G_{\rm ff}(\lambda,T) + G_{\rm bf}(\lambda,T)$ is modeled as the sum of the free-free Gaunt factor

$$\log G_{\rm ff}(\lambda,T) = 0.355\lambda^{-0.06}\log\lambda + 0.3\lambda^{-0.066}\log\left(\frac{T}{10^8}\right) + 0.0043 \tag{2}$$

(Mewe et al. 1986) and the bound-free Gaunt factor

$$G_{\rm bf}(\lambda,T) = aT^b e^{cT^d} \tag{3}$$

with the parameters a, b, c, and d adopted from Mewe et al. (1986). Introducing the variable $x = 1/\lambda$ we derive from Eq. 1 an expression for the total number dW of recorded photons divided by effective areas in each wavelength bin:

$$dW = B * G(\lambda, 143.9/\alpha)/\sqrt{143.9/\alpha} * x^2 e^{-\alpha x} \tag{4}$$

with $B = 2.05 \times 10^{-19} EM/(4\pi d^2) * \Delta t * \Delta\lambda$, $\alpha = 143.9/T$, and $x = 1/\lambda$. The plasma temperature can be derived from α and the emission measure $EM = n^2 V$ from B while $\Delta\lambda$=0.01 Å (the binsize of the spectrum), and the exposure time Δt=81.41 ksec. Best fit parameters B and α are obtained with a χ^2 fit. In order to minimize the effects from the emission lines, we actually use the inverse spectrum to be compared with $1/dW(B,\alpha)$. In each iteration step we calculate the temperature from α with $T(\alpha) = 143.9/\alpha$ and the Gaunt factor in each wavelength bin from Eqns. 2 and 3. From our best fit results we find $T = 20.7$ MK and $EM = 67.5 \times 10^{52}\,\mathrm{cm^{-3}}$. This temperature is high, we note, however, that the sensitivity to the temperature is quite different in the different wavelength ranges. In Fig. 4 three such wavelength ranges are shown for three different choices of temperature and the same emission measure $EM = 68 \times 10^{52}\,\mathrm{cm^{-3}}$. Because of the flatness of bremsstrahlung spectra the choice of the temperature is not important above 18 Å, but the position of the cutoff does depend sensitively on temperature. The number of emission lines between 13 and 16 Å is quite high

leading to line blends; the best fit bremsstrahlung continuum is therefore low (cf., middle panel of Fig. 4). With the bottom panel we wish to show that the assumption of $T = 14.4$ MK provides a realistic description for all wavelength ranges and in particular for the region near the thermal cutoff of the X-ray spectrum. In this case 79% of the X-ray luminosity L_X belongs to the continuum, thus $L_{X,cont} = 1.1 \times 10^{31}$ erg/sec. As a cross check we calculate the emission measure from the total luminosity and a mean radiative power loss due to bremsstrahlung of 1.5×10^{-23} erg cm^3/sec, and obtain $EM = 93 \times 10^{52}$ cm^{-3}. From this exercise we note that the continuum can well be modeled with a bremsstrahlung spectrum, and our *Chandra* data are consistent with an emission measure $EM = 68 \times 10^{52}$ cm^{-3} and a (peak) temperature at 15 MK.

4.2. Extracted spectra and measured line ratios

For the analysis of emission lines we use a maximum likelihood method which compares the sum of a model and the instrumental background with the non-subtracted count spectrum. In this way Poisson statistics can be explicitly taken into account. The model spectrum consists of one or more lines with a variable or fixed spacing and a source background, which is assumed to be constant over the region of interest (i.e., the spectral lines under individual consideration). This assumption is well justified since both the instrumental background is quite flat as well as the source background (bremsstrahlung spectrum) once multiplied with the effective areas. The method includes Poisson fluctuations both in the line and background counts. Our code assumes the line profile functions to be Gaussian, but other shapes can be easily implemented. In this paper we used the CORA program[1], version 1.2, for the analysis. It has been developed and described by Ness et al. (2001a), and can be downloaded from `http://ibiblio.org/pub/Linux/science/astronomy/`.

The analysis was performed on the basis of the count spectrum. The measured line counts are given in Tab. 3 and we list the best fits of the wavelengths λ, the Gaussian line-widths, the number of line photons, and the source background *sbg* measured in counts/Å which is assumed constant within the individual parts of the spectrum under consideration. In the last column we list the effective areas (as provided by D. Pease in Oct. 2000) as used for calculating line ratios needed for further analysis from the measurements; all errors in Tab. 3 are 1σ errors. The first part of Tab. 3 contains the He-like triplets Si XIII, Mg XI, Ne IX, O VII, and N VI in combination with their H-like lines Si XIV, Mg XII, Ne X, O VIII, and N VII. Since the Ne triplet is severely blended, the contaminating lines are also listed in Tab. 3.
For the density diagnostics of the higher temperature regions, five Fe XXI lines are also listed in Tab. 3, together with the ratios of each line with respect to the Fe XXI 128.73 Å line. For an estimate of optical depth effects, two Fe XVII lines were also measured and further analysis

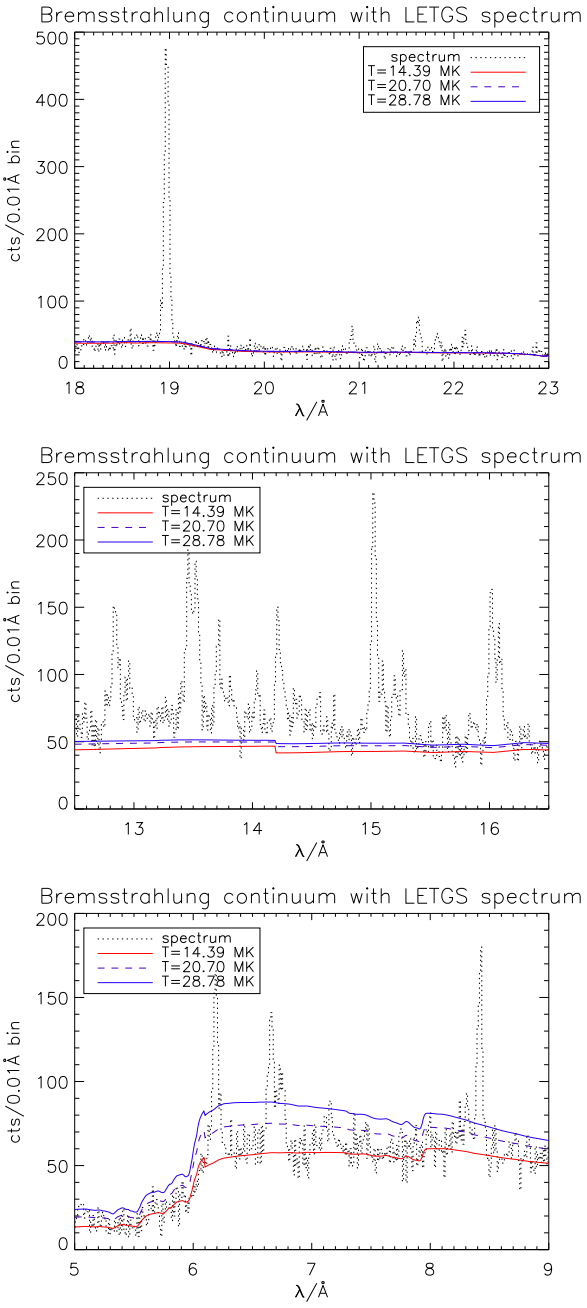

Fig. 4. Modeled bremsstrahlung spectrum with T = 14, 21, and 29 MK and $EM = 68 \times 10^{52}$ cm^{-3} in comparison with the measured spectrum. The model is converted to LETGS counts by use of the effective areas from Deron Pease (Oct. 2000). Top: very little sensitivity to the temperature, middle: attempt to model overlaps with higher temperatures, bottom: strong dependence of temperature suggesting 15 MK the only temperature consistent with all wavelength ranges.

[1] detailed description under
`http://www.hs.uni-hamburg.de/DE/Ins/Per/Ness/Cora`

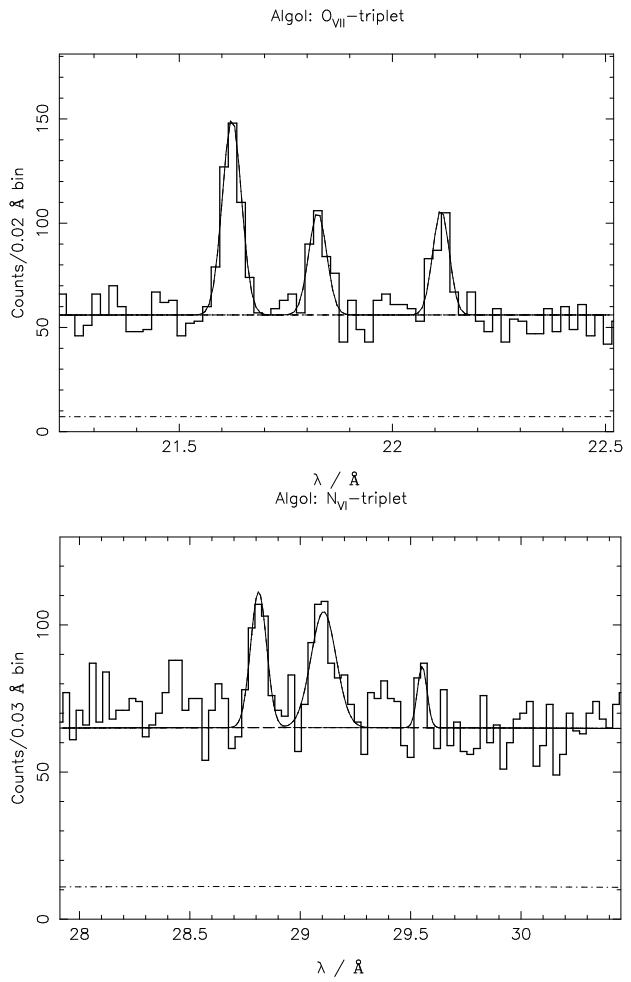

Fig. 5. (a,b) Spectrum (bold line) and best fit (thin solid line) for the triplets O VII (a) and N VI (b) for Algol. The dashed-dotted line represents the instrumental background.

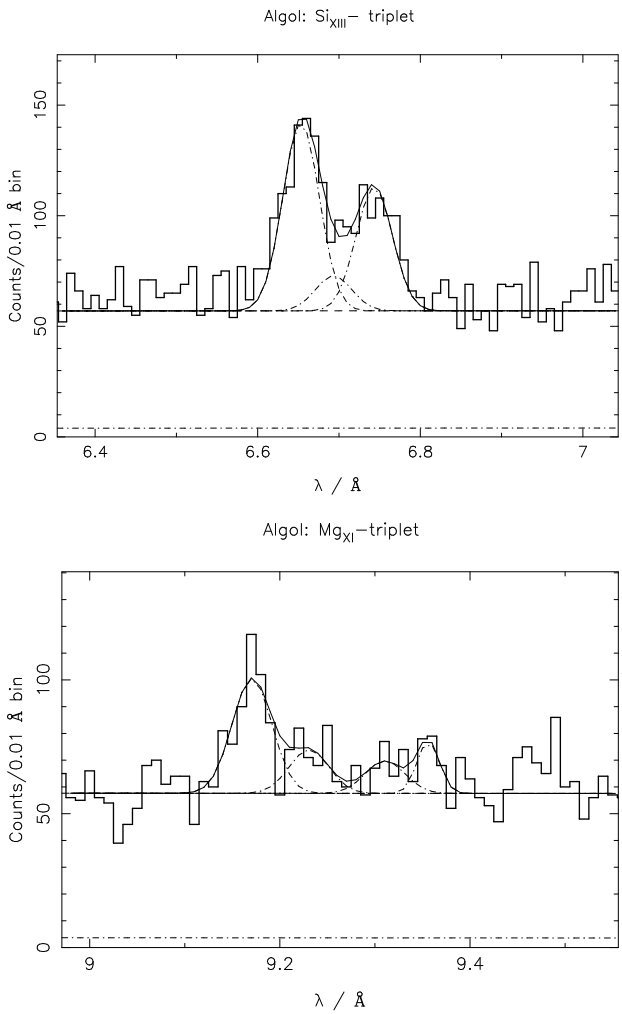

Fig. 6. (a,b) Same as Fig. 5 for Si XIII (a) and Mg XI (b). The unidentified line at 9.36 Å is also fitted with 57 cts.

is performed in Sect. 7.

4.2.1. Analysis of He-like line ratios

We first discuss the lower temperature He-like line systems from oxygen and nitrogen; we have not obtained a clear detection of the C V triplet near 41 Å. Since the C VI line at 33.75 Å is also not detected, we conclude that only very little plasma at temperatures producing C V and C VI is present in Algol's corona. In Fig. 5 (a,b) we show the region around the O VII triplet at 22 Å and the N VI triplet at 28 Å together with best fits of the resonance, intercombination, and forbidden lines. All three lines are clearly detected above the background, which is actually dominated by continuum radiation from Algol itself (cf., Fig. 1).

In Fig. 6 (a,b) we show the Mg XI and Si XIII triplets together with our best fits. Obviously, the relative spectral resolution of the LETGS becomes smaller with smaller wavelengths, and at short wavelengths the *Chandra* HETGS performs far better. Still, the lines are at least partially resolved and line parameters can be determined by fitting a line template to the data whose relative position is fixed. In this fashion the Si XIII triplet blend can be fitted and the determined value for the f/i ratio is consistent with the low density limit. The Mg XI triplet is more complicated. While the Mg XI r-line is clearly detected, there are no clear detections of the i and f-lines. In particular, the Mg XI f-line is unusually broad, yet we are not aware of other strong contaminating lines in that region as is suggested by the fit in Fig. 6 (b). The determined line fluxes and hence line ratios do of course depend on the adopted background levels, yet in no case do we find an f/i-ratio consistent with the low density limit. Since this is in conflict with both the Si XIII data as well as the Fe XXI data discussed below, we consider the "detections" of the Mg XI i and f lines shown in Fig. 6 (b) and reported in Tab. 3 as spurious.

4.2.2. Analysis of the Ne IX triplet

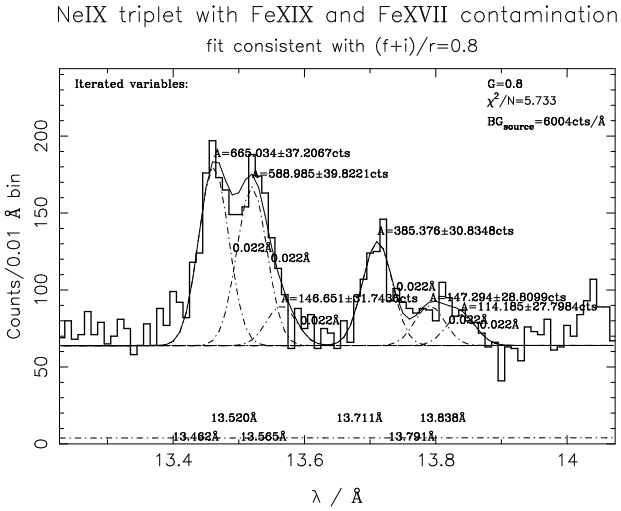

Fig. 7. The Ne IX triplet with blending lines from Fe XIX/XVII. The fit is constrained to (f+i)/r=0.8, i.e., granting a meaningfull G ratio, assuming log$T < 6.7$ (5 MK) for the Ne triplet.

The analysis of the Ne IX triplet is notoriously difficult, because of severe blending of the intercombination line at 13.55 Å with an Fe XIX line at 13.52 Å (cf., Fig. 7 and Tab. 3). The Ne IX resonance and the forbidden lines are clearly detected, while the intercombination line is "lost" in a large line blend longward of the resonance line. Our fits indicate 665 counts in the r-line, 385 counts in the f-line, and 736 counts in the i-line blend. The question is how many of those 736 counts are due to the Ne IX i-line rather than Fe XIX. In the following we estimate that by, first, constraining the fit to G=(f+i)/r=0.8G, and, second, by extrapolating line fluxes from other Fe XIX lines.

The fit shown in Fig. 7 was performed enforcing the boundary condition of G=0.8. With this constraint a reasonable fit is obtained with 147 counts in the intercombination line and the remaining 589 counts in the Fe XIX line. We now discuss whether this line count of 589 counts is consistent with extrapolations from other Fe XIX lines using MEKAL (Mewe et al. 1995) for calculating flux ratios. For this purpose we selected four other Fe XIX lines suitable for comparison, i.e., they are sufficiently isolated and/or sufficiently strong. These lines are located at 13.79 Å, 14.67 Å, 101.5 Å, and 108.5 Å, and our fit results are listed in Tab. 2; for comparison we use as reference line the Fe XIX at 13.52 Å. The measured flux ratios can be used for comparison with theoretical line flux ratios taken from MEKAL (Mewe et al. 1995). From the temperature analysis in Sect. 5 and from Tab. 4 we assume a temperature of 10 MK for extrapolating flux ratios from the theoretical fluxes.

The measured Fe XIX and Fe XVII ratios listed in Tab. 2 indicate that the measured flux ratios are systematically smaller than the theoretical ratios from MEKAL. This effect is more significant when using the Chianti data base. But the general trend is quite convincing indicating the Fe XIX lines at 13.52 Å and 13.79 Å to be well modelled in Fig. 7 and in Tab. 3. Also the results for Fe XVII at 13.84 Å seem to be realistic.

Eventually a reduction of Fe XIX at 13.52 Å would cure the difference between measured and theoretical ratios, leading to a higher value of the intercombination line. This would mean a higher G ratio (i.e., a lower temperature) and a lower f/i ratio (i.e., a higher density). But this reduction, in combination with a reduced Fe XIX at 13.79 Å flux, would also require an enhancement of the Fe XVII line at 13.84 Å in order to retain the sum of the blend at 13.79Å/13.84 Å, and the ratio of this line with the very strong 15 Å line would become smaller, which is the opposite effect of what would be intended with the reduction. We therefore trust our results obtained from the constrained fit only fixing the G ratio to 0.8.

Table 2. Measured line flux ratios for Fe XIX and Fe XVII lines used for consistency checks of the treatment of the Ne IX blend in Fig. 7. Values for effective areas $A_{\rm eff}$ are taken from In-Flight Calibration by Deron Pease (31. October 2000). The measured ratios are corrected for interstellar absorption with the values from Tab. 3. Theoretical flux ratios are obtained from MEKAL (Mewe et al. 1995) assuming log$T = 7.0$ (10 MK, cf. Tab. 4).

λ/Å	A [cts]	$A/\lambda/A_{\rm eff}$ ~[erg/cm^2]		Flux ratio	
			λ/13.52	meas.	theor.
Fe XIX lines			13.79	0.24 ± 0.05	0.30
13.52	588.98	1.66 ± 0.11	14.67	< 0.12	0.11
13.79	147.30	0.40 ± 0.07	101.5	0.07 ± 0.02	0.16
14.67	< 80.	< 0.20	108.5	0.19 ± 0.02	0.42
101.5	77.670	0.11 ± 0.02	λ/13.79		
108.5	204.00	0.29 ± 0.02	13.52	4.09 ± 0.85	3.3
			14.67	< 0.49	0.39
			101.5	0.3 ± 0.08	0.56
Fe XVII lines			108.5	0.80 ± 0.18	2.5
15.00	1042.7	2.56 ± 0.09	Ratio for Fe XVII λ/13.84		
13.84	114.20	0.31 ± 0.07	15.00	8.16 ± 2.0	12.9

4.2.3. Analysis of Fe XXI line ratios

The analysis of most of the Fe XXI lines was straightforward. For the Fe XXI line at 121.21 Å only an upper limit could be determined. Some difficulties were encountered for the Fe XXI 102.22 Å and the Fe XXI 117.505 Å lines. The Fe XXI line at 102.22 Å is partially blended with the 6^{th} order of Fe XVII at the original wavelength at 17.054 Å. The

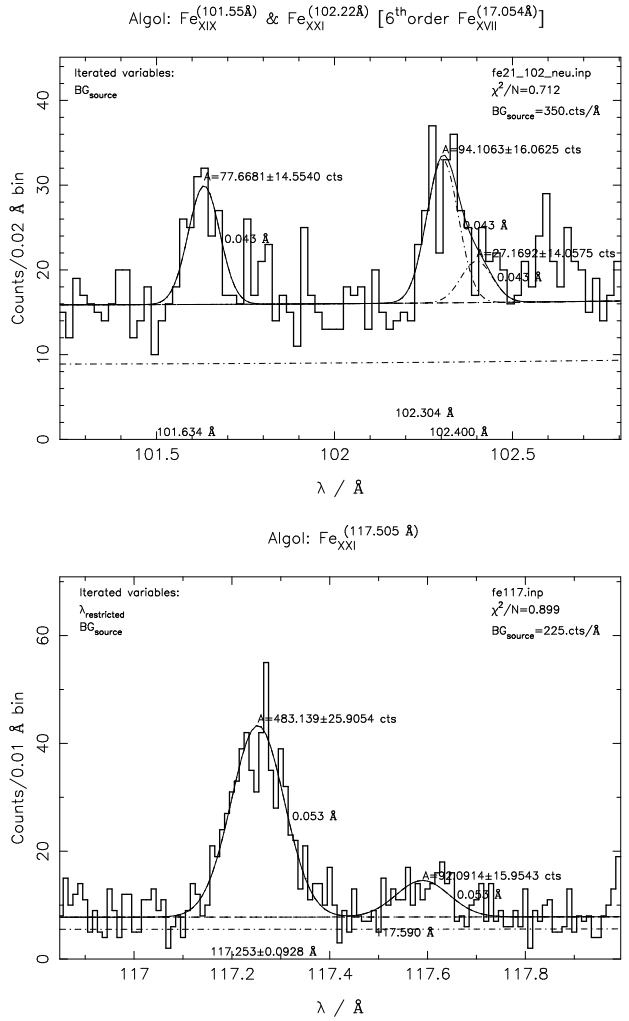

Fig. 8. Fitting of Fe XXI Top: Fe XXI (102.22 Å) in combination with Fe XIX (101.55 Å) and 6^{th} order of Fe XVII (17.054 Å) Bottom: Fe XXII (117.17 Å) and Fe XXI (117.505 Å)

Fe XXI line at 117.505 Å is found to be very broad such that it is difficult to find the correct wavelength position. In the top panel of Fig. 8 our model with the isolated Fe XIX line at 101.55 Å together with Fe XXI at 102.22 Å and the 6^{th} order of Fe XVII is shown. In the bottom panel of Fig. 8 the Fe XXI at 117.505 Å is shown in combination with the strong, isolated Fe XXII line at 117.17 Å. In both cases the isolated lines are used to determine the line shift of our measurement in comparison with the theoretical wavelengths. In that way the expected wavelength position for the weaker, or blended lines under consideration was used for the fit.

5. Temperature diagnostics

We carry out temperature diagnostics using temperature sensitive line ratios of Ly_α/He_r and of Fe Y/Fe Y + 1. The results are listed in Tab. 4. The ratios Ly_α/He_r were calculated from the line fluxes corrected for effective areas, as listed in Tab. 3. We assume plasma emissivities as calculated in the Codes MEKAL (Mewe et al. 1985; Mewe et al. 1995) and SPEX (Kaastra et al. 1996) and compare the measured ratios with the calculated emissivity ratios in order to derive line formation temperatures. The results are listed in Tab. 4 as T(H-He).

Table 4. Temperature diagnostics from the ratios of Ly_α/He_r for the ions Si XIV/XIII, Mg XII/XI, Ne X/IX, O VIII/VII, and N VII/VI. Temperatures for various Fe ions are calculated in the same manner by using theoretical line ratios from MEKAL.

	Ly_α/r	T(H-He) [MK]	$T_{\rm apex}$ [MK]
Si XIV / Si XIII	1.42 ± 0.13	14.2 ± 0.4	15.85/10.0
Mg XII / Mg XI	2.21 ± 0.29	10.1 ± 0.5	10.0/6.3
Ne X / Ne IX	3.91 ± 0.24	7.2 ± 0.2	5.62/3.98
O VIII / O VII	7.05 ± 0.62	4.6 ± 0.2	3.16/2.2
N VII / N VI	7.20 ± 1.10	3.2 ± 0.2	2.0/1.4
		flux ratio	T/MK
Fe XVII/Fe XVIII			
15.265/16.078		0.67 ± 0.07	7.93 ± 0.43
Fe XXI/Fe XXII			
117.51/117.17		0.19 ± 0.03	10.41 ± 0.71
Fe XXI/Fe XXII			
121.83/117.51		2.28 ± 0.46	10.38 ± 0.83
118.66/117.51		1.08 ± 0.27	10.73 ± 1.22

In addition we also investigate the temperature of Fe emitting layers with various Fe flux ratios (cf. Tab. 4 bottom). We used the photon fluxes corrected for effective areas from Tab. 3 and compared the ratios with theoretical ratios derived with MEKAL and SPEX, in the same manner as for the Ly_α/He_r ratios. The theoretical flux of the Fe XVIII 16.078 Å was corrected (enhanced) by a factor of 2.14 following Mewe et al. (2001).
From this analysis we find a cooler component of 8 MK, which is consistent with the Ly_α/He_r result for Ne. We also find hotter plasma at 10.5 MK in which the highly ionized Fe ions are formed. The ratios and derived temperatures are listed in Tab. 4. Clearly, a multitude of spectral components is present in the X-ray spectrum and we defer a discussion of the admissible emission measure distributions to a forthcoming paper.

Table 5. Atomic Parameters for He-like triplets. $T_{\rm apex}$ is the peak line formation temperature (MEKAL), R_0 is the low-density limit and $N_{\rm c}$ is the density were R falls to half its low-density value. R_0 and $N_{\rm c}$ are taken from Pradhan & Shull (1981) and Blumenthal et al. (1972).

ion	$T_{\rm apex}$/MK	R_0	$N_{\rm c}/(10^{10}{\rm cm}^{-3})$
Si XIII	10.0	2.67	3900
Mg XI	6.3	2.6	620
Ne IX	4.0	3.5	59.0
O VII	2.2	3.95	3.40
N VI	1.4	6.0	0.53

6. Density diagnostics

Estimates of coronal density can be obtained from the density sensitive f/i ratio of He-like triplets and from the Fe XXI line ratios. The He-like N VI, O VII, and Ne IX ions probe the lower temperature components, while the Mg XI, Si XIII, and the Fe XXI ions are used to probe the higher temperature components of the coronal plasma. The low-Z He-like ions are sensitive at densities $\log(n_e)$ between 9 and 12, while the high-Z He-like ions can only be used for higher densities above $\log(n_e)$ >12. Lower densities $\log(n_e) > 11$ at high temperatures ≈ 10 MK can be diagnosed from the Fe XXI ratios.

6.1. He-like ions

6.1.1. Theory of He-like triplets

The theory of the atomic physics of He-like triplets has been extensively described in the literature (Gabriel & Jordan 1969, Blumenthal et al. 1972, Mewe & Schrijver 1978, Pradhan et al. 1981, Pradhan & Shull 1981, Pradhan 1982, Pradhan 1985, and recently Porquet & Dubau 2000, Porquet et al. 2001, and Ness et al. 2001a).

In this paper we will determine electron densities n_e from the equation

$$R(n_e) = \frac{\rm f}{\rm i} = \frac{R_0}{1 + \phi/\phi_c + n_e/N_{\rm c}} \quad (5)$$

where R_0 denotes the low density limit and the parameter $N_{\rm c}$ the so-called critical density (cf. Tab. 5), around which the observed line ratio is density-sensitive. Finally, the parameters ϕ (the radiative absorption rate from $2\,^3S$ to $2\,^3P$ induced by an external radiation field) and ϕ_c describe the additional possible influence of the stellar radiation field on the depopulation of the ^3S state (cf., Sect. 6.1.2). Values for R_0 and $N_{\rm c}$ used in this paper are listed in Tab. 5. Also listed are the peak formation temperatures $T_{\rm peak}$ for the ions.

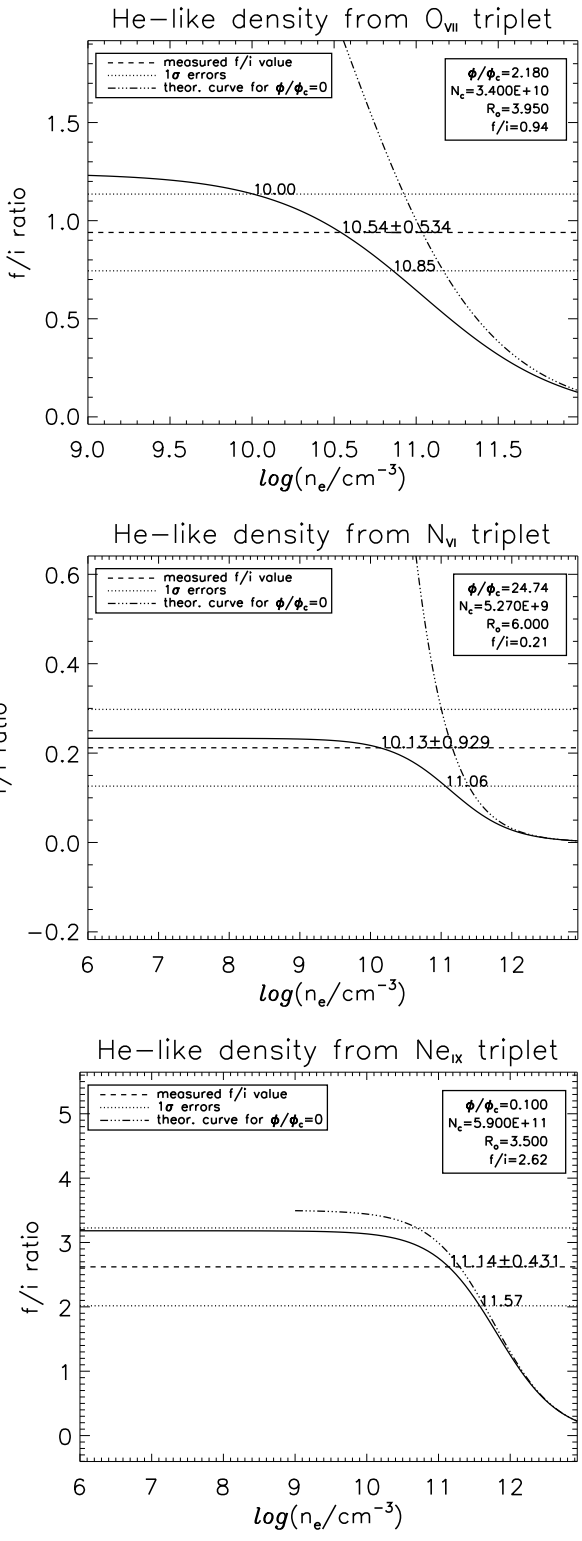

Fig. 9. He-like densities n_e from the ions O VII, N VI, and Ne IX. For comparison the theoretical curve assuming $\phi/\phi_c = 0$ is also plotted (cf. Eq. 5).

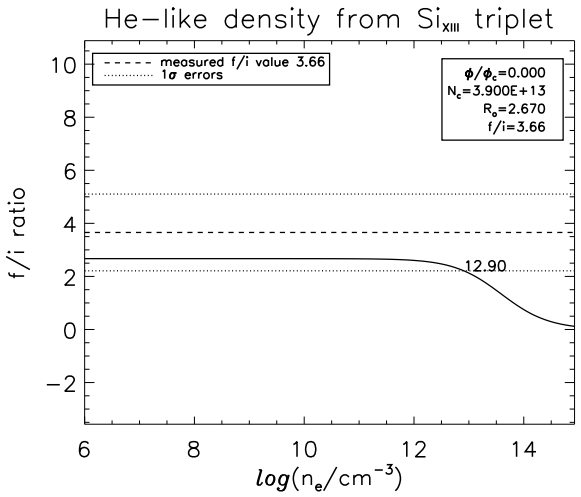

Fig. 10. He-like densities n_e from the Si XIII ion.

Table 6. Investigation of the influence of the stellar radiation field originating from the B8 star. Measured fluxes from the IUE satellite F_λ are converted to intensity I_λ taking into account limb darkening effects using ϵ from Tab. 1.

	N VI	O VII	Ne IX
$\lambda_{f\to i}$/Å	1900	1630	1266
I_{pot}/eV	552.1	739.3	1195.3
$\frac{F_\lambda}{(10^{-10}\frac{ergs}{cm^2\ s\ Å})}$	20 ± 2	22 ± 2.2	20 ± 6
$\frac{I_\lambda}{(10^{7}\frac{ergs}{cm^2\ s\ Å\ strd})}$	9.1 ± 0.91	9.98 ± 1.0	9.1 ± 2.7
T_{rad}/K	12066 ± 186	12708 ± 190	13686 ± 560
dilution factor		0.01	
ϕ/ϕ_c	24.74 ± 2.41	2.18 ± 0.29	0.1 ± 0.03

6.1.2. Influence of the stellar radiation field

Given the effective temperature of 13000 K of Algol A and its close proximity to Algol B (cf., Tab. 1), we must check to what extent the X-ray radiation originating from the corona of Algol B is influenced by the UV radiation from Algol A; the UV-radiation from the Algol B component itself is small when comparing its effective temperature with Capella ($T_{\rm eff} \leq$5000 K) and the values computed for ϕ/ϕ_c to be used in Eq. 5 as derived by Ness et al. (2001a). Also the measurements of other G and K type stars, as presented by Ness et al. (2001) suggest Algol B not to contribute to the total radiation field. Following Ness et al. (2001a) we used IUE measurements of Algol in order to derive radiation temperatures for the desired wavelengths, listed in Tab. 6. From this we calculated values ϕ/ϕ_c for N VI, O VII, and Ne IX using a dilution factor of

$$W = \frac{1}{2}\left[1 - \left\{1 - \left(\frac{r_\star}{a}\right)^2\right\}^{1/2}\right] = 0.01 \qquad (6)$$

(Mewe & Schrijver 1978) using as distance between Algol A and B $a = 14.6\,R_\odot$ (Forbes 1997) and the radius of Algol A $r_\star = 3.5\,R_\odot$ (Tab. 1). The result of our analysis is listed in Tab. 6. Since we assumed the worst case scenario, we find the maximally possible values ϕ/ϕ_c, so that the effects are not negligible for O VII and not zero even for Ne IX. We do point out, however, that in the phases between 0.74 and 1.06 (cf. Sect. 3) much of the visible coronal emission could originate from regions not illuminated by the B star. With an inclination angle of 81.5° and the assumption of a uniform distribution of the coronal plasma, geometrical considerations lead to the result that at phase $\phi = 1$ only plasma near the polar regions can be illuminated by the primary component. A detailed discussion of these geometrical considerations is given in Ness et al. (2001). In the following analysis we calculate coronal densities with and without the effects of the radiation field from the B star, i.e., assuming $\phi/\phi_c = 0$ and with the values for ϕ/ϕ_c from Tab. 6.

6.1.3. Densities with the He-like ions

The measured ratios f/i, corrected for $A_{\rm eff}$ (Deron Pease, Oct. 2000; the values are listed in the last column of Tab. 3), as quoted in Tab. 3, were used for density diagnostics. The theoretical curves from Eq. 5, with the values ϕ/ϕ_c from Tab. 6 and the other parameters from Tab. 5, are plotted in Figs. 9 and 10 for each ion in comparison with our measurements for f/i with 1σ errors. For the low-Z elements O, N, and Ne we also considered the case of no radiation field from the B star affecting the emitting layers with a line-dotted line in Fig. 9. The influence is most severe for N VI and O VII, but is also visible for Ne IX. Assuming a negligible radiation field from the primary component we obtain definite deviations from the low density limit for N VI and O VII and a marginal deviation for Ne IX; in the latter the latter case the 2σ error includes the low density case. In these cases we find densities between 1–2 $\times 10^{11}$ cm^{-3} (cf., Tab. 7). Assuming the full radiation field supplied from the B star to be effective the sensitivity of our measurements to detect densities is significantly reduced because the difference between the R-value in the high density case (R = 0) and low-density case becomes smaller and smaller. Specifically, for our Algol LETGS spectrum we find that the data are consistent with the low-density limit for nitrogen and neon, and even for oxygen the low density limit is included within the 2σ error bars. For silicon and magnesium radiation effects are unimportant. The derived f/i-ratio for silicon is consistent with the low density limit, while our measurements for magnesium (formally) yield densities of $\approx$ log $n_e = 13$; as discussed in Sect. 4.2.1 and Fig. 6 (b), we consider the measurements of the i and f lines in magnesium spurious.

6.2. Density diagnostic with Fe XXI

In addition to He-like ions, ions with more than two electrons can be used as a density diagnostic. The ground configuration of Fe XXI $1s^2 2s^2 2p^2$ splits up into ^3P, ^1D, ^1S. The energy difference between the ground state $^3P_0$ and the excited levels $^3P_1$ and $^3P_2$ is 9 eV and 14.5 eV, respectively, and 30 eV between ground state and $^1D_2$. In low-density plasmas virtually all atoms are in the ground state ^3P, while in high-density plasmas a Boltzmann equilibrium with the higher level will be obtained. Consequently, from excited levels certain lines will appear only in high-density plasmas. In contrast to He-like lines the appearance of certain lines is an indicator of high-density plasmas.

Our measurements of four Fe XXI ratios, corrected for effective areas and interstellar absorption are listed in Tab. 3 (effective areas and values from interstellar absorption are listed in the last two columns) and plotted in comparison with theoretical flux ratio vs. n_e curves obtained with Chianti (Dere et al. 2001) in Figs. 11 and 12. As can be seen from Figs. 11 and 12, only low density limits or upper limits are obtained for all Fe XXI line ratios. Similar results are obtained when using the ratios from Brickhouse et al. (1995). The most sensitive upper limit ($\log n_e < 11.52$) comes from the Fe XXI 102.2 Å/128.7 Å ratio, and is a factor ~ 24 below the upper limit derived for the Si XIII triplet, which is formed at similar temperatures. This comparison clearly shows that Fe XXI line ratios yield far more sensitive density constraints at high temperature as compared to He-like triplets from magnesium, silicon, and higher ions.

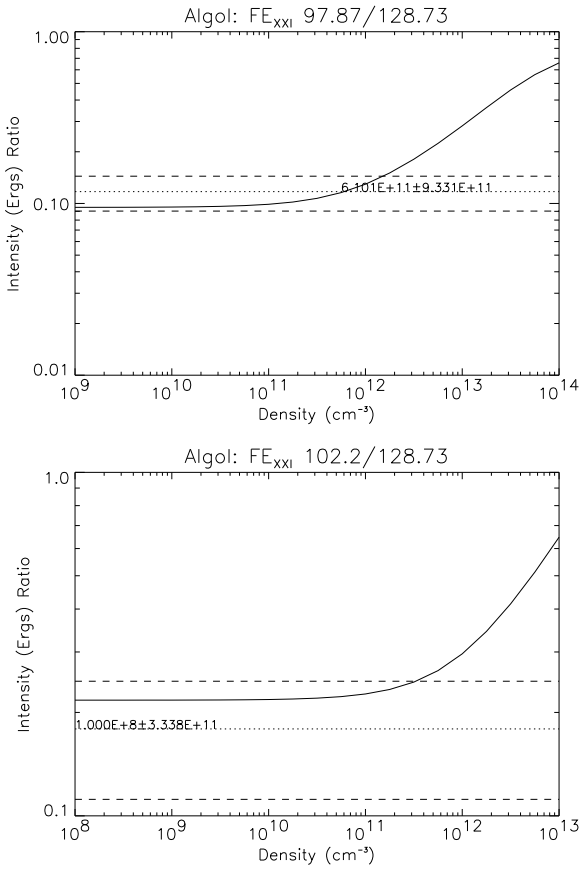

Fig. 11. Density diagnostic with Fe XXI ions. 1σ errors are indicated with dashed line style (used 2σ error for 102 Å ratio).

7. Optical depth effects

The *Chandra* Algol spectrum contains a number of strong Fe XVII lines which are sensitive to optical depth effects. In order to estimate the optical depth, we use an "escape factor" model with a homogeneous mixture of emitters and absorbers in a slab geometry (e.g., Kaastra & Mewe 1995, Mewe et al. 2001). In this geometry the escape factor is $P(\tau) \sim [1 + 0.43\tau]^{-1}$. Significant optical depths will lead to resonant scattering in strong lines. Photons originally traveling outwards may be backscattered and lost in lower layers. The optical depth in a given line can be computed from (Schrijver et al. 1994)

$$\tau = 1.2\ 10^{-17} \left(\frac{n_i}{n_{el}}\right) A_z \left(\frac{n_H}{n_e}\right) \lambda\ f \sqrt{\frac{M}{T}} n_e \ell \qquad (7)$$

(Schrijver et al. 1994) with the fractional ionization denoted by n_i/n_{el}, the elemental abundances by A_z, the ratio of hydrogen to electron density $n_H/n_e = 0.85$, the oscillator strength f for the ion under consideration, the atomic number M, the wavelength λ, measured in Å, the temperature T in K, the electron density n_e in cm^{-3} and the mean free path denoted by ℓ. If one considers two lines produced by the same ion, the ratio of the optical depths is given by

$$\frac{\tau_1}{\tau_2} = \frac{\lambda_1\ f_1}{\lambda_2\ f_2}. \qquad (8)$$

Therefore, one must look for lines from the same ion and large difference in oscillator strength or wavelength. In the solar context one usually studies the ratio of the strong Fe XVII 15.03 Å resonance line ($f = 2.66$) and another, nearby Fe XVII line with a small oscillator strength (e.g., 15.265 Å, $f = 0.593$). Estimating the escape factor P from $P = \left(\frac{15.03\ \text{Å}}{15.27\ \text{Å}}\right)_{\text{meas}} / \left(\frac{15.03\ \text{Å}}{15.27\ \text{Å}}\right)_{\tau=0}$ we can deduce the optical depth.

For the measured Fe XVII 15.03/15.265 photon flux ratio we obtain a formal fit result of 2.81 ± 0.25 (cf. Tab. 3). This ratio does depend on the assumed background value and can vary between 2.32 and 3.45 when varying the source background (between 4000 and 5000 cts/Å; comp. Tab. 3). In this particular wavelength region (cf., Fig. 4, middle) line blending is severe and a correct "eye" placement of the continuum is difficult. However, our continuum modeling predicts relative stable values of 4500 cts/Å so that we are confident that our quoted result is correct

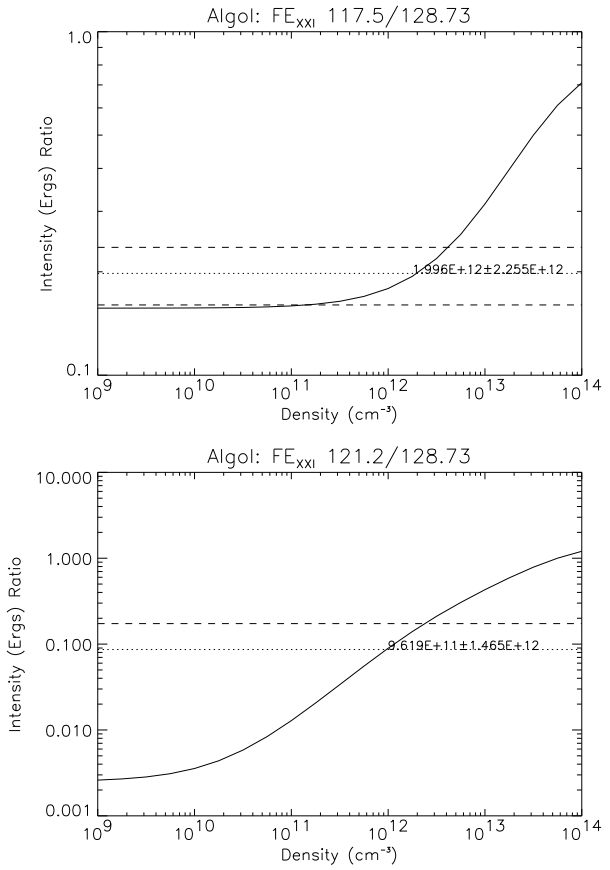

Fig. 12. Density diagnostic with Fe XXI ions.

Table 7. Summary of derived densities.
* Resulting density values accounting for stellar radiation fields.
** 2σ upper limit.

He-like triplets		
	f/i	$\log(n_e)$
Si XIII	3.66 ± 1.44	<12.9
Mg XI	0.90 ± 0.37	n.a.
Ne IX	2.62 ± 0.61	11.30 ± 0.60
*Ne IX		<11.57
O VII	0.94 ± 0.20	11.04 ± 0.13
*O VII		10.54 ± 0.53
N VI	0.21 ± 0.09	11.16 ± 0.23
*N VI		10.13 ± 0.93
Fe XXI ratios		
λ/Å	ratio	$\log(n_e)$
97.87	0.12 ± 0.03	<12.19
102.22	0.18 ± 0.03	< 11.52**
117.51	0.20 ± 0.04	<12.63
121.22	<0.09	<12.4

and not affected by systematic errors from the placement of the continuum background. We point out that this measurement agrees remarkably well with the same line ratio as measured in Capella (Mewe et al. 2001); this is interesting because in Capella no measurements of density could be obtained.

The measured photon flux ratio must be compared to the $\tau = 0$ flux ratio, which can be deduced either from theory or laboratory measurements. With SPEX we predict a ratio of 3.5, thus $P = (2.81 \pm 0.25)/3.5 = 0.8 \pm 0.07$, and therefore $\tau = 0.57 \pm 0.26$. With Chianti (Dere et al. 2001), a ratio of ≈ 4 is expected for $\tau = 0$, and using $P = (2.81 \pm 0.25)/4 = 0.7 \pm 0.06$ we find $\tau = 0.98 \pm 0.3$. In either case we find optical depths significantly different from zero (at $\sim 2 - 3\sigma$ level).

Unfortunately theory does not agree with experiment. The very same line ratio can be measured in the Livermore Electron Beam Ion Trap (EBIT; Brown et al. 2001, Laming et al. 2000). These experiments typically yield Fe XVII 15.03/15.265 photon flux ratios in the range 2.5 - 3.0, which are significantly different from those expected theoretically. Also, Brown et al. (2001) point out that contamination of the 15.265 Å with Fe XVI further lowers the observed 15.03/15.265 photon flux ratio. Comparing the Algol (and Capella) flux ratios in 15.03/15.265 to the values quoted by Brown et al. (2001) we therefore conclude that the observations are fully consistent with an optical thin plasma without any significant optical depth with possibly some contamination arising from Fe XVI. It is worrying that the theoretically predicted emission from some of the strongest emission lines observed in solar and stellar X-ray spectra appears to be wrong by ≈ 30 percent.

8. Discussion and Interpretation

From the derived parameters we can obtain structural information on Algol's corona. From the lower temperature He-like ions definite coronal densities could be determined, from the higher temperature He-like ions as well as from the Fe XXI line ratios (cf., Tab. 7) upper limits to the coronal density at a temperature of 10 MK can be derived. Since $\mathrm{EM} = n_e^2 V$, typical coronal volumes V can be estimated from the recorded emission measures.

We now assume that Algol's corona is composed of a multitude of individual, but identical loops, all of which obey the loop scaling equation (Rosner et al. 1978)

$$n_e L = 1.3 \times 10^6 T_{\mathrm{apex}}^2, \qquad (9)$$

with the densities n_e, the apex temperature T_{apex}, and the loop semilength L, all in *cgs* units. Of course, the apex temperature T_{apex} cannot be directly measured, it must however be close to the formation temperature of the ion with the highest ionization temperature and it can certainly not exceed the temperature of the bremsstrahlung continuum (Sect. 4.1). It is also clear that in Algol one is most likely dealing with a distribution of X-ray emitting

loops as is the case in the solar corona. However, our data does not allow us to constrain the parameters of these distributions and therefore we model the distributions by their presumed mean values. From Tab. 4 we conclude that the apex temperatures $T_{\rm apex}$ must be approximately 15 MK, which is also supported by the continuum temperature, while from Tab. 7 we conclude that $\log n_e < 11.5$. Obviously the densities at 15 MK could be arbitrarily low. However, if we assume that the material at 15 MK is in thermal pressure equilibrium with the material at 2 MK (where the O VII line is produced) we estimate densities in the range $\log n_e \sim 9.7$ - 10.2, depending on whether the X-ray emitting corona of Algol B is immersed in the UV radiation field of Algol A or not. For $\log n_e = 11.5$ we compute $L = 9 \times 10^8$ cm while for densities $\log n_e =$ 9.7 - 10.2 we find L = 180 - 460$\times 10^8$ cm. In either case, the loop lengths are much smaller than the stellar radius of 2.45 $\times 10^{11}$ cm so that we assume to deal with an essentially planar geometry. If we assume "canonical loops" with circular cross sections of a tenth of the loop length, the volumes of such coronal building blocks are in the range $2.5\,10^{25}$ cm^3 to $3\,10^{30}$ cm^3, again depending on the assumed density, and in all cases one requires at least 1000 loops (or more) in order to account for the total observed emission measure.

Let us next assume that the considered loops are semicircular and extend to height

$$H = \frac{2L}{\pi}. \tag{10}$$

We define the coronal filling factor as the ratio between the available volume $4\pi R^2 H$ and the actual volume of X-ray emitting material $V_{\rm cor} = EM/n_e^2$:

$$f = \frac{V_{\rm cor}}{V_{\rm available}} = \frac{EM}{8 n_e^2 R^2 L}, \tag{11}$$

where R denotes the stellar radius. Inserting the scaling law to replace L with $T_{\rm apex}$ and n_e, we finally find

$$f = 9.6 \times 10^{-8} \frac{EM}{n_e R^2 T_{\rm apex}^2} = 9.6 \frac{EM_{52}}{n_{10} R_{11}^2 T_6^2} \tag{12}$$
$$[EM_{52} = EM/10^{52}\,{\rm cm}^{-3}, R_{11} = R/10^{11}\,{\rm cm},$$
$$T_6 = T_{\rm apex}/10^6\,{\rm K}, n_{10} = n_e/10^{10}\,{\rm cm}^{-3}].$$

Using the continuum values $EM_{52} = 68$ and $T_6 = 15$ we find $f \times n_e = 5 \times 10^9$ cm^{-3}. Since the filling factor f can be unity at most, we deduce that $n_{min} = 5 \times 10^9$ cm^{-3} and the actual density ought to exceed that value. Interestingly, $n_{min} T_{\rm apex}/T_{\rm OVII}$ is close to the density determined from demanding that the high temperature material is at the same pressure as the O VII emitting material (assuming that it is immersed in the primary's radiation field). Alternatively, density values of 1.5×10^{10} cm^{-3} lead to filling factors of ≈ 0.3. These densities can only be reached without the illuminating UV radiation field of the primary component. The overall phase range covered by the *Chandra* LETGS observations is 0.32. During that period the star rotates by 115°; therefore most of the hemisphere visible at the beginning of our observations are not visible at the end. The observed light curve (cf. Fig. 2) with its slowly decreasing trend does not appear to give the impression of coming from a number of unrelated regions, rather, it appears to come from the same region on the star. This is only possible if the region is located near the pole (in which case it would be immersed in the radiation field) or if it is fortuitously located in a equatorial region which happens to be visible during the whole phase interval. While the latter possibility cannot be excluded, the former option appears more plausible given the previous evidence for polar activity in Algol (Schmitt & Favata 1999), the available VLBI images of Algol (Mutel et al. 1998) and the general occurrence of polar spots in Doppler images in general. It is attractive to interpret the observed X-ray emission as arising from the circumpolar regions, possibly from a long-duration flare similar to the one observed by Schmitt & Favata (1999). Assuming as height the limit inferred from the eclipsing BeppoSAX flare (H $\leq 7\ 10^{10}$ cm) and as filling factor arbitrarily a value of 1 percent (which is the surface area of the circumpolar polar cap), we find a volume of 4×10^{32} cm^3, which requires densities of $2.5\ 10^{10}$ cm^{-3} when combined with the observed emission measures. These densities refer to the hot material at temperatures of $\approx 15\,10^6$ K. Clearly, these densities are fully consistent with the observed upper limits.

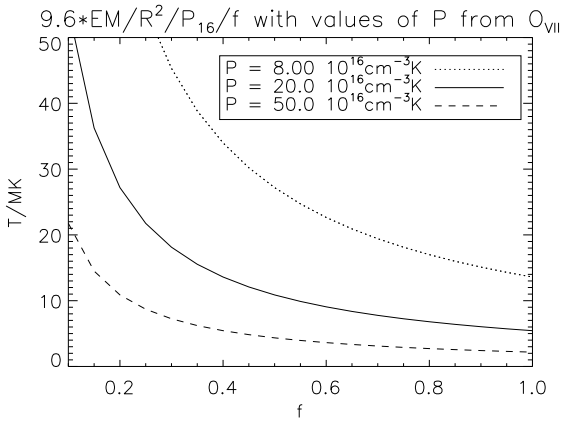

Fig. 13. Temperatures required for asserting certain filling factors (cf. Eq. 13) assuming constant pressures calculated from the densities and temperatures measured for O VII. For the emission measure we use the value obtained from the continuum $EM = 68 \times 10^{52}$ cm^{-3}.

Continuing in our picture of "canonical" loops, we can compare a typical pressure scale height $H_p = 5000\,T_{\rm apex}/(g/g_\odot) = 3.8 \times 10^{11}$ cm using $T_{\rm apex} = 15$ MK and $g/g_\odot = 0.2$, with a typical loop size $L \approx 30 \times 10^8$ cm (Eq. 9). Since $H_p >> L$, the assumption of constant pressure is well justified. Hence $P = n_e * T$ must be constant

and thus Eq. 12 can be rewritten as

$$f = 9.6\frac{EM_{52}}{P_{16}R_{11}^2T_6} \Longleftrightarrow T_6 = 9.6\frac{EM_{52}}{P_{16}R_{11}^2 f} \quad (13)$$
$$[P_{16} = n_e * T/10^{16}\,\mathrm{cm}^{-3}\mathrm{K}],$$

which relates the unknown filling factor with the - in principle - measured parameters stellar radius, emission measure and coronal pressure. In Fig. 13 we plot the dependence of temperatures on filling factor for different pressures, using Eq. 13; the emission measure obtained from the continuum (Sect. 4.1) was used. The pressures are calculated from the measured temperatures (Tab. 4) and densities (Tab. 7) for O VII. In the case of the radiation field from the B star to influence the density diagnostics, a lower limit for the pressure of $P = 8 \times 10^{16}\,\mathrm{cm}^{-3}\mathrm{K}$, using the peak formation temperature $T = 2.2\,\mathrm{MK}$ is calculated, while we obtain $P = 50 \times 10^{16}\,\mathrm{cm}^{-3}\mathrm{K}$ for the higher density from omitting the possible effects from the radiation field and the higher temperature obtained from the Ly_α/r ratio (Tab. 4).

It is clear that T must exceed 10 MK and is very likely below 30 MK. For low pressure ($\mathrm{P}_{16} = 8$) the filling factor would have to exceed 0.45, while for high pressure ($\mathrm{P}_{16} = 50$) the filling factor would have to be in the interval $0.07 < f < 0.21$. Since we feel that filling factors $f \sim 1$ are unlikely, we favor a high pressure scenario.

Acknowledgements. J.-U.N. acknowledges financial support from Deutsches Zentrum für Luft- und Raumfahrt e.V. (DLR) under 50OR98010.
The Space Research Organization Netherlands (SRON) is supported financially by NWO.

References

Berghöfer T.W., Schmitt J.H.M.M., & Cassinelli J.P., 1996, A&A 118, 481
Blumenthal G.R., Drake G.W., & Tucker W.H., 1972, ApJ 172,205
Brickhouse N.S., Raymond J.C., and Smith B.W., 1995, ApJS 97, 551
Brown G.V., Beiersdorfer P., Liedahl D.A., et al., 1998, ApJ 502, 1015
Brown G.V., Beiersdorfer P., Chen H., et al., 2001, ApJ 557, L75
Díaz-Cordovés J., Claret A., & Giménez A., 1995, A&AS 110, 329
Dere K. P., Landi E., Young P. R., & Del Zanna G. 2001 ApJS 134, 331, The Chianti database, with extension to X-Ray wavelengths
Favata F. & Schmitt J.H.M.M., 1999, A&A 350, 900
Forbes T.G. in *Magnetic Reconnection in the Solar Atmosphere* (eds Bently, R.D. & Mariska, J.T.) Vol. 111, 259 (ASP Conf. Ser., 1997)
Gabriel A.H. & Jordan C., 1969, MNRAS 145, 241
Kaastra J.S., Mewe R., & Nieuwenhuijzen H., 1996, in UV and X-ray Spectroscopy
Kaastra J. & Mewe R., 1995, A&AL 302, L13
Kim Ho-Il, 1989, ApJ 342, 1061
Laming J.M., Kink I., Takacs E., et al., 2000, ApJ 545, L161
Mewe R., Gronenschild E.H.B.M., & van den Oord G.H.J., 1985, A&AS 62, 197
Mewe R., Kaastra J.S., & Liedahl D.A., 1995, Legacy 6, 16 (MEKAL)
Mewe R., Raassen A.J.J., Drake J.J., et al., 2001, A&A 368, 888
Mewe R. & Schrijver J., 1978, A&A 65, 99
Mewe R., Lemen J.R., & van den Oord G.H.J., 1986, A&AS 65, 511
Mutel R.L., Molnar L.A., Waltman E.B., & Ghigoi F.D., 1998, ApJ 507, 371
Ness J.U., Mewe R., Schmitt J.H.M.M., et al., 2001a, A&A 367, 282
Ness J.U., Mewe R., Schmitt J.H.M.M., et al., 2001b, PASP submitted (Poster at Stellar Coronae 2001)
Ness J.U., Mewe R., Schmitt J.H.M.M., et al., 2001c, PASP submitted (Talk at CS12)
Oord G.H.J. van den, Mewe R., 1989, A&A 213, 245
Ottmann R. & Schmitt J.H.M.M., 1996, A&A 307, 813
Porquet D. & Dubau J., 2000, A&AS 143, 495
Porquet D., Mewe R., Dubau J., et al. 2001, A&A 376, 1113
Pradhan A.K., 1982, ApJ 263, 477
Pradhan A.K., 1985, ApJ 288, 824
Pradhan A.K., Norcross D.W., & Hummer D.G., 1981, ApJ 246,1031
Pradhan A.K. & Shull J.M., 1981, ApJ 249,821
Predehl P., Braeuninger H., Brinkman A., et al., 1997, Proc. SPIE 3113, 172
Preś P., Siarkowski M., & Sylwester J., 1995, MNRAS 275, 43
Richards M.T., 1993, ApJ 86, 255
Rosner R., Tucker W.H., & Vaiana G.S., 1978, ApJ 220, 643
Schmitt J.H.M.M. 1998, ASP Conference Series, Vol. 154
Schmitt J.H.M.M. & Favata F., 1999, Nature 401, 44
Schmitt J.H.M.M. & Kürster, 1993, Science 262, 215
Schrijver C.J., van den Oord G.H.J., & Mewe R., 1994, A&AL 289, L23
White N.E., Culhane J. L., Parmar A. N., et al., 1986, ApJ 301, 262

Table 3. Measured line counts for Algol with 1σ errors. Values of the total effective areas $A_{\rm eff}$ are taken from In-Flight Calibration by Deron Pease (31. October 2000). The Transmissions from the ISM are based on N(H I) = 2.5×10^{18}, N(He I)/N(H I) = 0.09, N(He II)/N(H I) = 0.01

	λ [Å]	σ [Å]	A [cts]	sbg [cts/Å]	$R_{\rm obs}$ =f/i $[R]^{(2)}$	$G_{\rm obs} = \frac{\rm i+f}{\rm r}$ $[G]^{(2)}$	$A_{\rm eff}$ [cm^2]
He-like and H-like (cf. Sects. 5 and 6.1.3)							
Si XIV	6.19 ± 0.0016	0.025 ± 0.002	658.32 ± 35.06	5119			36.22
Si XIII*r*	6.65 ± 0.004		480.7 ± 35.95				37.54
i	6.69 ± 0.014	0.022± 0.003	86.4 ± 33.10	5300	3.64 ± 1.44	0.83 ± 0.15	37.38
f	6.74 ± 0.006		314.1 ± 30.60		[3.66 ± 1.45]$^{(2)}$	[0.84 ± 0.15]$^{(2)}$	37.16
Mg XII	8.42 ± 0.0016	0.02 ± 0.002	578.04 ± 33.13	5900			32.28
Mg XI*r*	9.17 ± 0.0015		224.12 ± 26.15				27.69
i	9.23 ± 0.0015	0.02 ± 0.002	84.85 ± 23.29	5400	0.90 ± 0.36	0.72 ± 0.22	27.42
f	9.31 ± 0.0015		76.09 ± 22.80		[0.90 ± 0.37]$^{(2)}$	[0.73 ± 0.23]$^{(2)}$	27.24
Ne X	12.14 ± 0.0004	0.021 ± 0.0008	2481.48 ± 56.31	6510			24.96
Ne IX	*cf. Sect.4.2.2*						
r	13.46 ± 0.003	0.022 ± 0.0022	665.03 ± 37.21				26.16
i	13.56 ± 0.011	0.022 ± 0.0022	146.65 ± 31.74	6000	2.63 ± 0.61	0.80	26.23
f	13.71 ± 0.004	0.022 ± 0.0022	385.38 ± 30.83		[2.62 ± 0.61]$^{(2)}$	–	26.29
Fe XIX	13.52 ± 0.003	0.022 ± 0.0022	588.98 ± 39.82		[fit constrained to G=0.8]		26.21
Fe XIX	13.79 ± 0.007	0.022 ± 0.0022	147.29 ± 28.81				26.31
Fe XVII	13.84 ± 0.07	0.022 ± 0.0022	114.18 ± 27.80				26.32
O VIII	18.9701 ± 0.0004	0.0262 ± 0.0004	2882.96 ± 57.81	3150			24.29
O VII*r*	21.62 ± 0.016	0.022 ± 0.002	262.49 ± 22.6				15.58
i	21.82 ± 0.021	0.021 ± 0.004	128.77 ± 18.7	2439	0.94 ± 0.2	0.95 ± 0.16	15.34
f	22.11 ± 0.022	0.020 ± 0.004	120.9 ± 18.0		[0.94 ± 0.2]$^{(2)}$	[0.97 ± 0.16]$^{(2)}$	15.32
N VII	24.8 ± 0.0012	0.03 ± 0.0012	1119.05 ± 38.38				15.23
N VI*r*	28.81 ± 0.007	0.037 ± 0.008	141.33 ± 21.10				13.57
i	29.11 ± 0.011	0.058 ± 0.012	188.23 ± 25.53	1800	0.20 ± 0.08	1.60 ± 0.37	13.57
f	29.55 ± 0.011	0.021 ± 0.007	37.5 ± 14.31		[0.21 ± 0.09]$^{(2)}$	[1.65 ± 0.38]$^{(2)}$	12.76
Fe XXI *density diagnostics (cf. Sect. 6.2)*					$\frac{\rm F(\lambda)}{\rm F(128.73Å)}$ $^{(1)}$	ISM	
	97.87	0.049	67.20 ± 14.50	334	0.12 ± 0.03	0.9206	7.17
	102.22	0.043	94.11 ± 16.1	350	0.18 ± 0.07	0.9111	6.64
	117.505	0.058	92.10 ± 16.00	225	0.20 ± 0.04	0.8734	6.13
	121.22	0.055	< 36	117	< 0.09	0.8633	5.55
	128.73	0.058	266.32 ± 20.90	73	1	0.8420	3.64
Ne IX *consistency check (cf. Sect. 4.2.2)*							
Fe XIX	14.66 ± 0.007	0.02 ± 0.002	< 80	5010		0.999	26.99
Fe XIX	101.63 ± 0.007	0.043 ± 0.006	77.67 ± 14.55	350		0.9124	6.69
Fe XIX	108.45 ± 0.007	0.054 ± 0.006	203.53 ± 19.42	311		0.8964	6.42
Fe XVII *optical thickness (cf. Sect. 7)*					$\frac{\rm F(15.03Å)}{\rm F(15.27Å)}$	$\frac{\rm F(15.03Å)}{\rm F(15.27Å)}$ $^{(2)}$	
Fe XVII	15.026 ± 0.001	0.021 ± 0.001	1018.44 ± 38.93	4500			27.21
Fe XVII	15.27 ± 0.008	0.023 ± 0.003	364.71 ± 28.92	4500	2.79 ± 0.25	[2.81 ± 0.25]$^{(2)}$	27.42
Fe *temperatures (cf. Sect. 5)*					A[cts/cm^2]$^{(2)}$		
Fe XVII	15.28 ± 0.004	0.024 ± 0.003	375.73 ± 29.30	4500	14.22 ± 1.11		26.42
Fe XVIII	16.082 ± 0.0031	0.03 ± 0.004	572.78 ± 35.95	4500	21.07 ± 1.32		27.19
Fe XXII	117.25 ± 0.093	0.053 ± 0.06	483.14 ± 25.91	225	78.56 ± 4.21		6.15
Fe XX	118.81 ± 0.014	0.0623 ± 0.013	97.87 ± 16.98	225	16.26 ± 2.82		6.02
Fe XX	121.98 ± 0.009	0.0675 ± 0.009	180.88 ± 19.23	138	34.19 ± 3.64		5.29

$^{(1)}$ Fluxes accounting for $A_{\rm eff}$ and ISM as in last but one column. $^{(2)}$ Fluxes corrected for $A_{\rm eff}$ listed in the last column.

Chapter 5

Coronal density diagnostics for seven cool stars

Talk held in Noordwijk, June 26, 2001 at

Stellar Coronae 2001

to be published in ASP Conf. Series

TITLE
ASP Conference Series, Vol. **VOLUME**, **PUBLICATION YEAR**
EDITORS

Coronal density diagnostics with Helium-like triplets: CHANDRA–LETG observations of Algol, Capella, Procyon, ϵ Eri, α Cen A&B, and UX Ari

Jan-Uwe Ness

Universität Hamburg, Gojenbergsweg 112, D-21029 Hamburg, Germany

Rolf Mewe

Space Research Organization Netherlands (SRON), Sorbonnelaan 2, 3584 CA Utrecht, The Netherlands

Jürgen H.M.M. Schmitt

Universität Hamburg, Gojenbergsweg 112, D-21029 Hamburg, Germany

Anton J.J. Raassen

Space Research Organization Netherlands (SRON), Sorbonnelaan 2, 3584 CA Utrecht, The Netherlands

Rob L.J. van der Meer

Space Research Organization Netherlands (SRON), Sorbonnelaan 2, 3584 CA Utrecht, The Netherlands

Vadim Burwitz

Max-Planck-Institut für Extraterrestrische Physik (MPE), Postfach 1603, D-85740 Garching, Germany

Peter Predehl

Max-Planck-Institut für Extraterrestrische Physik (MPE), Postfach 1603, D-85740 Garching, Germany

Albert C. Brinkman

Space Research Organization Netherlands (SRON), Sorbonnelaan 2, 3584 CA Utrecht, The Netherlands

Abstract. Electron density and temperature diagnostics based on the triplets of Helium-like ions are applied to the X-ray spectra of seven cool stars measured with the Low Energy Transmission Grating Spectrometer (LETG) on board the Chandra X-ray Observatory. New theoretical models for the calculation of the line ratios between the forbidden (f), intercombination (i), and the resonance (r) lines of the He-like triplets are used. The effects from stellar radiation fields were taken into account.
A strong correlation between the H-like, He-like line ratios with total X-ray luminosities is found for nitrogen and oxygen. Since this ratio is a

temperature indicator we conclude that active stars have higher plasma temperatures than less active stars.
The densities found for O VII show a trend indicating that in inactive stars low densities are present, comparable to the quiescent Sun, while for the active stars we measure both low and high densities, as high as measured in solar flares. We want to point out, however, that most of the emission is produced at higher temperatures, thus the densities derived from O VII represent a weaker and cooler (2 MK) plasma component.

1. Introduction

1.1. The instrument

The new generation of X-ray telescopes provides with XMM and Chandra a new dimension concerning sensitivity (XMM) and resolution (Chandra). Spectroscopic measurements can be performed with both instruments using the Reflection Grating Spectrometer (RGS) onboard XMM and the High Energy Transmission Grating (HETG), Medium Energy Transmission Grating (METG) and the Low Energy Transmission Grating (LETG) onboard Chandra. While RGS, HETG and METG provide large effective areas for high energies ranging from 5 to 40 Å with high resolution, the LETG covers a much larger wavelength range from 5 – 175 Å with high spectral resolution comprising both the ROSAT bandpass (5 – 124 Å) and the Einstein bandpass (3 – 84 Å). The spectral resolution in the long wavelength region even exceeds the resolution of the other instruments with reasonable effective areas.
One advantage of the LETG is the large wavelength range measuring, e.g., the N VI triplet at around 29 Å and the C V triplet at around 41 Å, not covered by METG and RGS. But also the measurement of O VII is important, since the METG suffers from steep gradients in effective area in the respective wavelength range around 22 Å. The LETG is the only new instrument covering long wavelengths >100 Å, thus a number of highly ionized Fe (XVIII to XXIII) lines can also be measured.

1.2. The spectra

The spectra obtained with the LETG are shown in Fig. 1 for the stars Algol, Capella, and Procyon. As can be seen from Fig. 1, our sample of stars covers a range of quite different X-ray emitters. While for Procyon most of the emission is found in spectral lines, continuum emission is seen for Capella while the strongest continuum is found for Algol. The continua are mainly found around 17 Å where also strong emission lines, mainly from Fe, Si, Ne, and Mg, are seen for Algol and Capella, but not for Procyon. For Procyon the strongest line is Fe IX at 171 Å, formed at low temperatures, which is very weak in Capella, and not detected in the Algol spectrum. Instead we find highly ionized Fe ions from Fe XVIII (94 Å) up to Fe XXIII (e.g. 132 Å).
We want to point out that isolated lines can be measured and line ratios can be calculated.

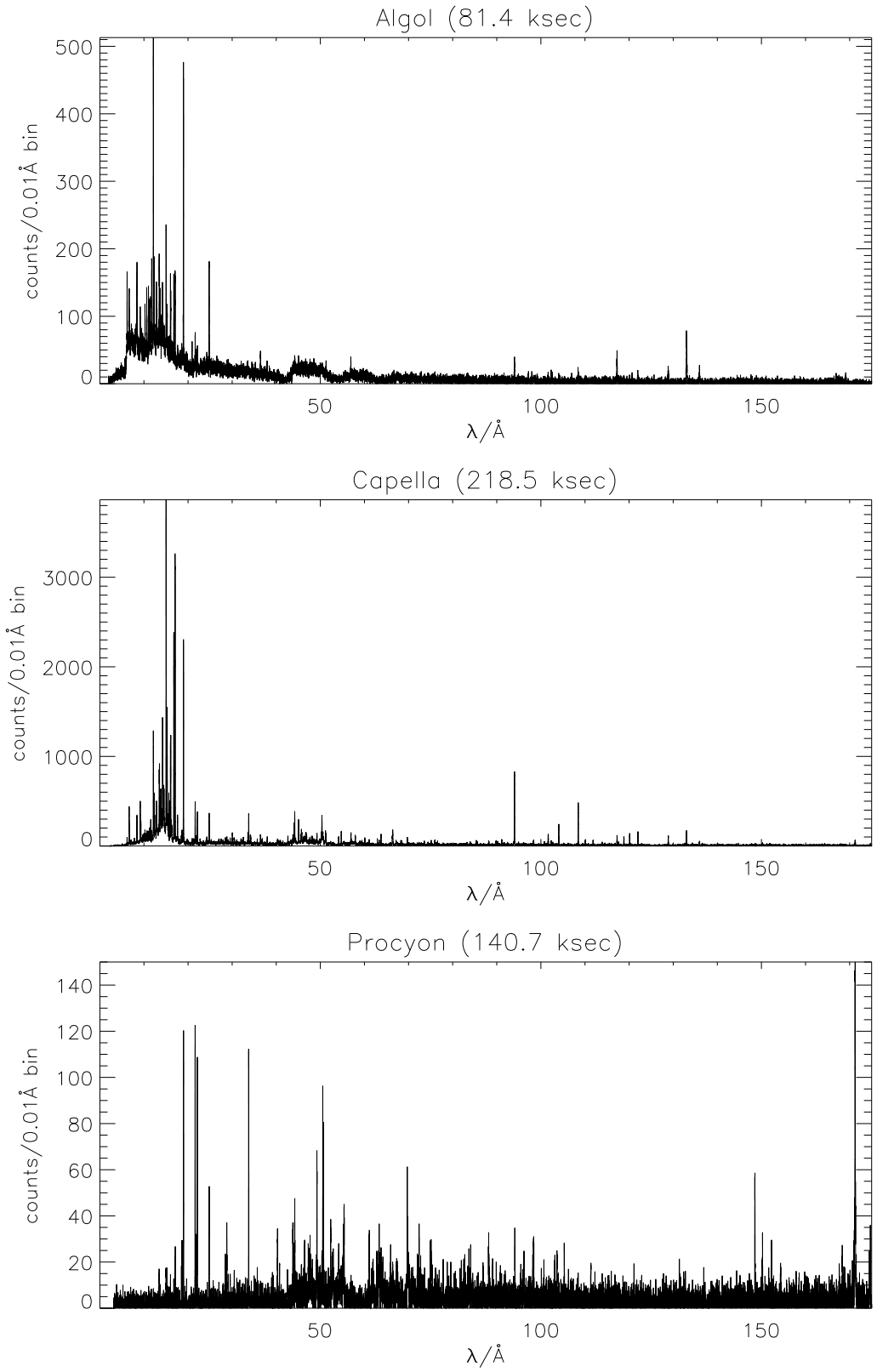

Figure 1. Total LETG spectra of Algol, Capella and Procyon.

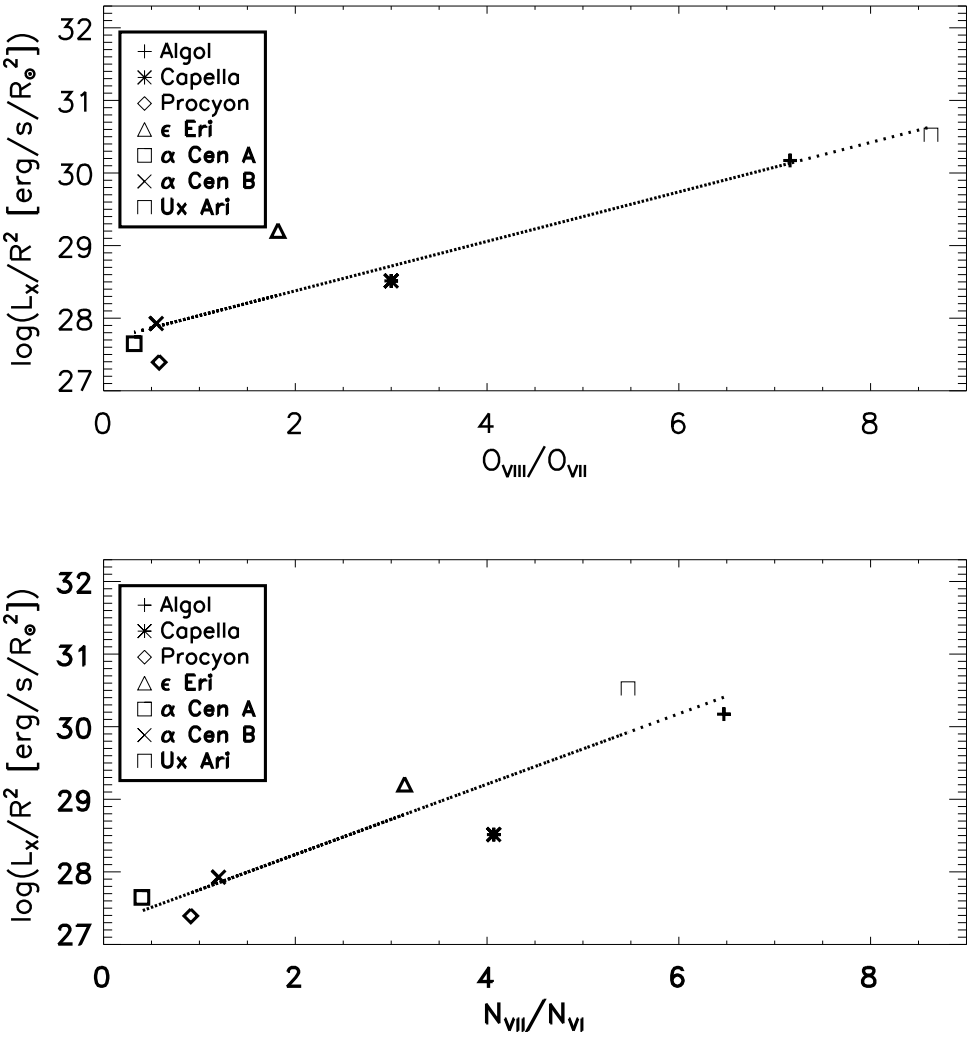

Figure 2. Relation between line ratio Ly_α/He-like and surface flux $L_X/R_\star$ with the stellar radii $R_\star$ in units $R_\odot$ for O VIII/O VII (top panel) and N VII/N VI (bottom panel)

2. The stars

The selected sample of stars comprises a range of X-ray luminosities L_X from few 10^{27} up to 10^{32} ergs/sec. For the inactive stars Procyon and α Cen A and B ($L_X \sim 6\,10^{27}$ ergs/sec) we measure small ratios O VIII/O VII ~ 1. This ratio is a measure of plasma temperatures with a high ratio indicating high temperatures. For the most active stars Algol ($L_X = 2\,10^{31}$ ergs/sec) and UX Ari ($L_X = 7\,10^{31}$ ergs/sec) we measure the highest ratios 7.2 and 8.6. The intermediate active stars ϵ Eri ($L_X = 10^{29}$ ergs/sec) and Capella ($L_X = 3\,10^{30}$ ergs/sec) are measured with intermediate ratios with 1.8 and 3, respectively. The relation between plasma temperature and X-ray luminosity is not entirely new (e.g, Schrijver et

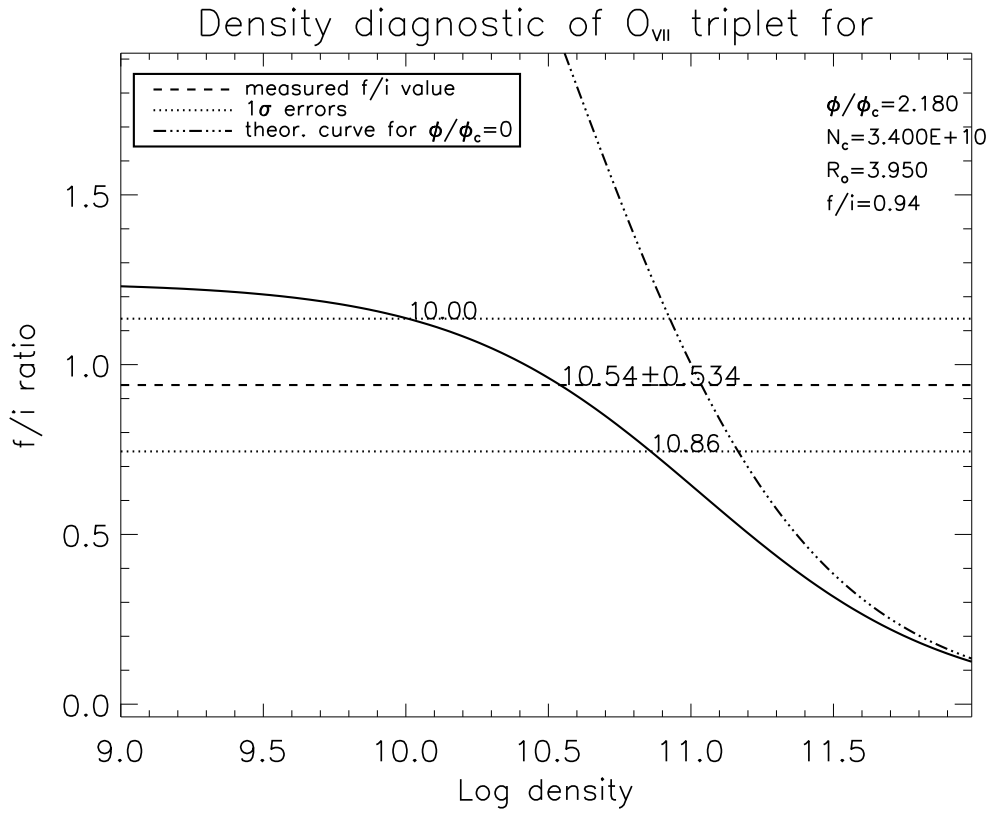

Figure 3. Inferring densities from the line ratio f/i for the example of Algol. The term ϕ/ϕ_c was measured with IUE, and the theoretical curves given with and without radiation term (i.e. ϕ/ϕ_c=0)

al. 1984), but measuring these line ratios reflecting the plasma temperature is new. In Fig. 2 the relation is plotted using the surface luminosity $L_X/R_\star^2$ for the line ratios O VIII/O VII and N VII/N VI, where the lines involved were detected in all the stars.

3. Theory of He-like triplets

For details of He-like triplet density diagnostics we refer to Gabriel & Jordan (1969), Blumenthal et al. (1972), Mewe & Schrijver (1978), Pradhan et al. (1981), Pradhan & Shull (1981), Pradhan (1982), Pradhan (1985), and recently Porquet & Dubau (2000), Porquet et al. (2001) and Ness et al. (2001a). In the notation of He-like triplets we use an r denoting the resonance line ($1s2p\,^1P_1$), an i for the intercombination line ($1s2p\,^3P_1$) and an f for the forbidden line ($1s2s\,^3S_1$) with all lines decaying radiatively to the ground level $1s^2\,^1S_0$. The electron densities are derived from the line ratio f/i of forbidden line f and intercombination line i, where in a high density plasma ions in the forbidden level will be excited by collisions into the intercombination level from where they can decay radiatively. Special care is necessary when dealing with, e.g., early type stars providing strong UV radiation fields triggering the excitation

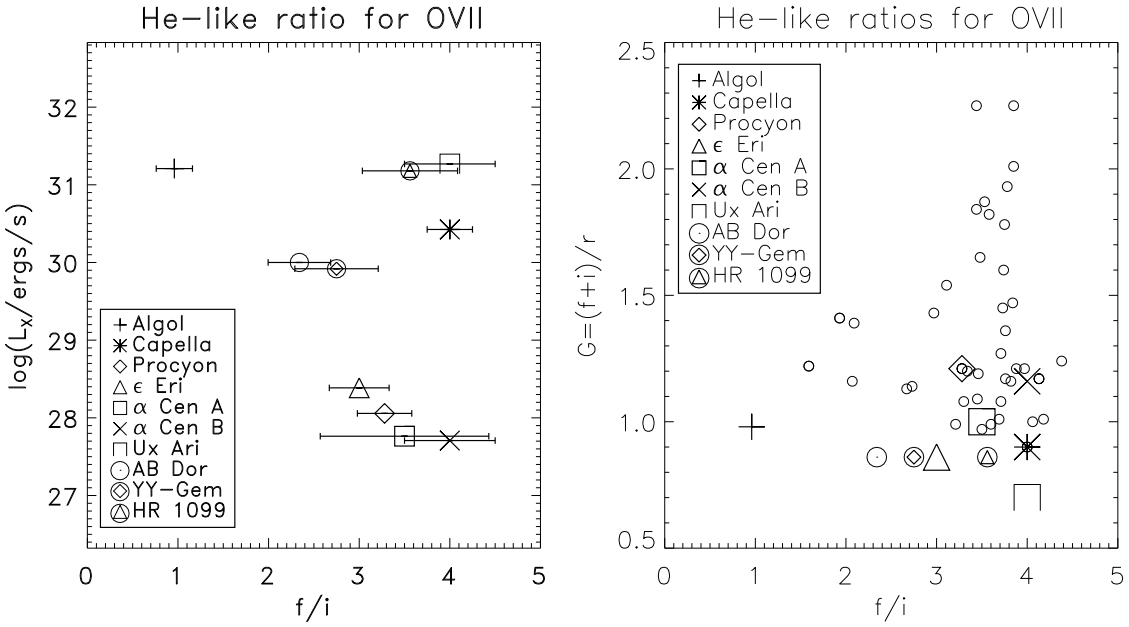

Figure 4. Left panel: f/i ratios for the stars vs. X-ray luminosity (ROSAT bandpass). The encircled measurements are XMM measurements (Güdel, Audard et al. 2001a,b).
Right panel: R=f/i vs. G=(f+i)/r for the stars in comparison with solar measurements (for references see Ness et al. 2001a)

f $\rightarrow$ i radiatively. In our sample Procyon and Algol are of particular importance in this respect. For more details on this we refer to Ness, Mewe, & Raassen (2001) and Ness, Mewe, & Schmitt (2001b).
Fig. 3 shows how densities can be derived from the measured line ratio f/i in the example of Algol. The solid line represents the theoretical curve taking into account the measured UV radiation field (represented by the term ϕ/ϕ_c, cf. Blumenthal et al. 1972), while the dash-dotted line represents the theoretical curve neglecting the radiation field. In this particular case it is not clear whether the measured radiation field actually affects the measured coronal emission, since it does not originate from the stellar surface but from the companion B star (Ness et al. 2001c). The electron density can be derived by comparing the measured f/i ratio, represented by the dashed line, with errors (dotted), with the corresponding theoretical curve (dash-dotted for neglecting the radiation field and solid line for accounting for the entire radiation field i.e. $\phi/\phi_c = 2.18$).

4. Results

For comparison between the stars we use the measured f/i ratios instead of densities, because deriving densities from f/i requires atomic data, which might be ambiguous. The f/i ratios, though, contain all effects, thus also the influence of radiation fields, satellite lines etc. In Fig. 4 we plot the f/i ratio for O VII versus the X-ray luminosity L_X (left panel) and versus the ratio G=(f+i)/r

(right panel), which is commonly used as a temperature indicator. The X-ray luminosities are converted to ROSAT luminosities, which is possible with the LETG, because it covers a wavelength range including the ROSAT bandpass. XMM observations of YY Gem, AB Dor and HR1099 were added for completion of the sample (He-like ratios from Güdel et al. 2001a,b and ROSAT luminosities from, e.g., Hünsch et al. 1998). The small circles in the right panel are solar measurements collected from the literature (e.g. McKenzie & Landecker 1982). For YY Gem, AB Dor and HR 1099, no G-ratios were given in the literature, so values close to one were assumed, but the G-ratio is not used for further analysis.

5. Conclusions

With the high-resolution spectra obtained with Chandra and XMM it is possible for the first time to measure single lines in the X-ray range with reasonable effective areas over a wide bandpass. In this way densities can be obtained in a direct way by using the theory of the He-like triplets. Other line ratios, e.g., Fe XXI lines, can also be used to obtain densities. The densities are the missing piece between emission measure and volumes. Measuring the densities independently is thus a step to obtain structural information of the otherwise spatially unresolved stellar coronae.
Using the line ratio f/i of the He-like triplets we see a trend, indicating that inactive stars tend to have low densities in general, while in more active stars higher densities can be measured. One needs to be careful with this conclusion concerning, e.g. Algol, where the radiation effect might lead to a low f/i ratio. But from our discussion of Algol in Sect. 3 we rather assume high densities to be in charge of the low f/i ratio. In Fig. 4 three exceptions can be seen with the active stars Capella, UX Ari and HR1099, where we measure low densities with high f/i ratios. From the small sample of stars it is difficult to draw reliable conclusions. It must be kept in mind that the O VII triplet is formed only in a small temperature regime around $\log T \sim 6.3$. But the dominant emission measure lies not in the peak formation temperature of O VII for the active stars. A similar trend can be seen for N VI, which is also detected for all stars.
From the right panel of Fig. 4 it can be seen that the solar G-ratios scatter, while they are close to one for all stars, which is expected for collision dominated plasmas (Porquet et al. 2001). In this sense the solar scattering is puzzling, however, these data are collected from different sources in the literature (cf. Ness et al. 2001a) and are sometimes ambiguous concerning the observed parts of the Sun. Also, quite different instrumentation was used.
Concerning the f/i ratios we find that active stars with high densities have similar f/i ratios for O VII than solar flare data and the inactive stars lie in the bulk of quiescent solar data.

Acknowledgments. J.-U.N. acknowledges financial support from Deutsches Zentrum für Luft- und Raumfahrt e.V. (DLR) under 50OR98010.
The Space Research Organization Netherlands (SRON) is supported financially by NWO.

References

Blumenthal G.R., Drake G.W. & Tucker W.H., 1972, ApJ 172, 205
Gabriel A.H. & Jordan C., 1969, MNRAS 145, 241
Güdel M., Audard M., Briggs K. et al., 2001a, A&A 365, L336
Güdel M., Audard M., Magee H. et al., 2001b, A&A 365, L344
Hünsch M., Schmitt J.H.M.M. & Voges W., 1998, A&A 132, 155
McKenzie D.L. & Landecker P.B., 1982, ApJ, 259, 372
Mewe R. & Schrijver J., 1978, A&A 65, 99
Ness J.U., Mewe R., Schmitt J.H.M.M. et al., 2001a, A&A 367, 282
Ness J.U., Mewe R., Schmitt J.H.M.M. et al., 2001b, ASP Conf. Series, submitted
Ness J.U., Schmitt J.H.M.M., Burwitz V. et al., 2001c, in preparation
Ness J.U., Mewe R. & Raassen A.J.J., 2001, PASP submitted
Porquet D. & Dubau J., 2000, A&AS 143, 495
Porquet D., Mewe R., Dubau J. et al. 2001, A&A, submitted
Pradhan A.K. & Shull J.M., 1981, ApJ 249, 82
Pradhan A.K., Norcross D.W. & Hummer D.G., 1981, ApJ 246,1031
Pradhan A.K., 1982, ApJ 263, 477
Pradhan A.K., 1985, ApJ 288, 824
Schrijver C.J., Mewe R., Walter F.M., 1984, A&A 138, 258

Chapter 6

Influence of UV radiation fields on the density diagnostics for Algol and Procyon

Poster presented in Noordwijk, June 25-June 29, 2001 at conference

Stellar Coronae 2001

to be published in ASP Conf. Series

TITLE
ASP Conference Series, Vol. **VOLUME**, **PUBLICATION YEAR**
EDITORS

Influence of radiation fields on the density diagnostics CHANDRA–LETGS observations of Algol and Procyon

Jan-Uwe Ness

Universität Hamburg, Gojenbergsweg 112, D-21029 Hamburg, Germany

Rolf Mewe

Space Research Organization Netherlands (SRON), Sorbonnelaan 2, 3584 CA Utrecht, The Netherlands

Jürgen H.H.M. Schmitt

Universität Hamburg, Gojenbergsweg 112, D-21029 Hamburg, Germany

Anton J.J. Raassen

Space Research Organization Netherlands (SRON), Sorbonnelaan 2, 3584 CA Utrecht, The Netherlands

Abstract. Spectroscopic density diagnostics based on He-like triplets have been used to investigate the structure of the solar corona for more than three decades. With the new instrumentation onboard Chandra and XMM this method of analysis can now also be applied to stellar coronae. In collision-dominated plasmas the He-like ratio R=f/i of the forbidden line ($1s2s\,^3S_1 \rightarrow 1s^2\,^1S_0$) and the intercombination line ($1s2p\,^3P_{2,1} \rightarrow 1s^2\,^1S_0$) is used as a sensitive indicator of electron density, yielding high values of R for low densities ($n_e < 10^9$ cm^{-3}). Measuring a low flux in the forbidden line compared to the intercombination line, however, is not always an indicator for high densities, it might also indicate that the depopulation of the forbidden line level ($1s2s\,^3S_1 \rightarrow 1s2p\,^3P_{2,1}$) is due to a relatively strong UV radiation field rather than to collisions in a high-density plasma.
We illustrate this effect with Chandra LETGS measurements of the binary Algol, consisting of an X-ray dark B star and a K star with a very active corona, and the inactive F star Procyon. Focusing on the triplets of C V, N VI, O VII, and Ne IX, we show that the radiation fields might have significant influence on the density analysis of the low-Z ions of C, N and O in both cases, in spite of the different radiation dilution factors. The sources of the UV radiation are of completely different origins for the two stars. While for Procyon the radiation originates from the stellar surface, the radiation in the case of Algol is supplied by the companion B star. A detailed investigation of whether the observed part of Algol's corona is actually illuminated by the radiation field of the B star, is thus necessary.

1. Introduction

In Fig. 1 spectra obtained with Chandra LETG of the resolved O VII triplet for the stars Algol and Procyon are shown. As can be seen, the ratio of the forbidden line (f) and the intercombination line (i) differ quite noticeably. We want to find out whether a low f/i ratio indicates high densities or not.

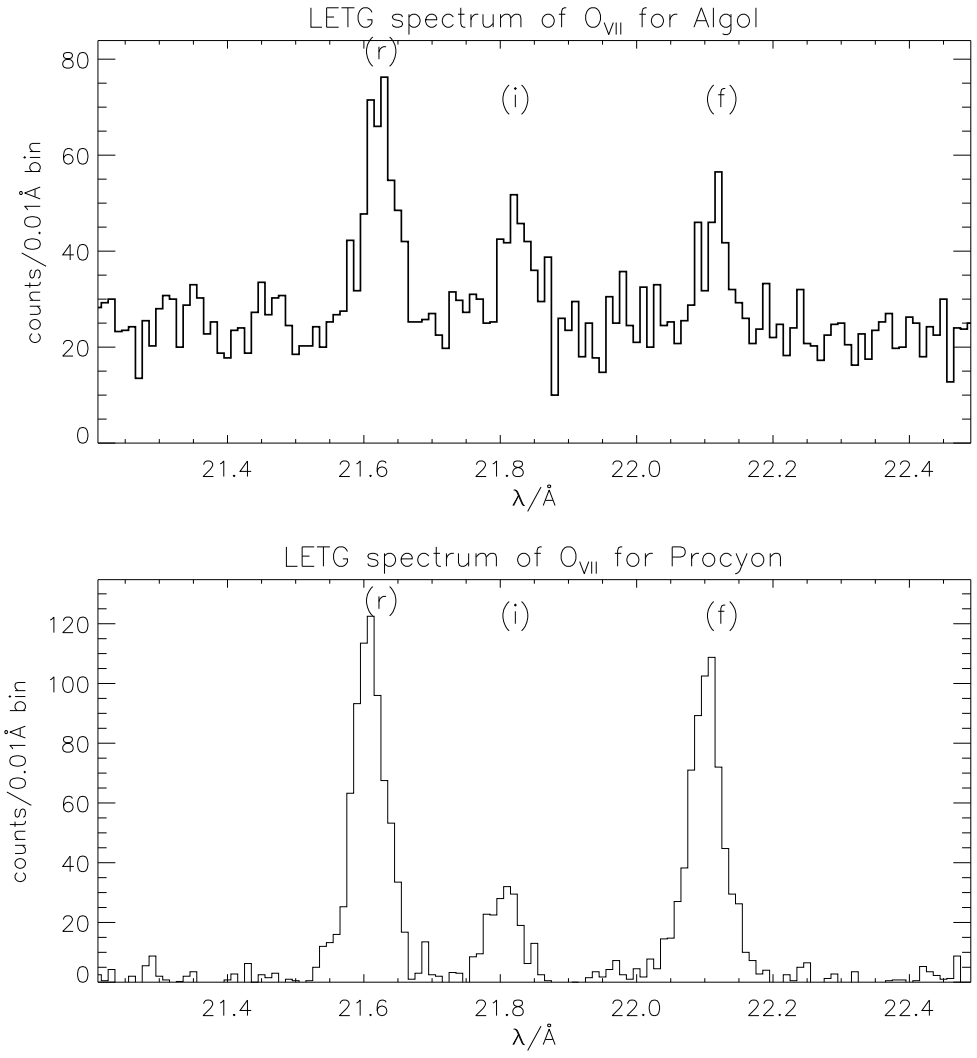

Figure 1. LETG Spectra of Algol and Procyon showing the O VII triplet

2. Theory of He-like triplets

He-like triplet density diagnostics were developed by Gabriel & Jordan (1969), and refined by Blumenthal et al. (1972), Mewe & Schrijver (1978), Pradhan et

al. (1981), Pradhan & Shull (1981), and recently Porquet et al. (2001). In the notation for He-like triplets we use an r denoting the resonance line ($1s2p\,^1P_1$), an i for the intercombination line ($1s2p\,^3P_{2,1}$), and an f for the forbidden line ($1s2s\,^3S_1$) with all lines ending in the ground level $1s^2\,^1S_0$ (cf. Fig. 2). The transition under consideration is from $1s2s\,^3S_1$ (metastable) to $1s2p\,^3P_{2,1}$, or f $\rightarrow$ i, competing with the radiative de-excitation of the f level ($1s2s\,^3S_1 \rightarrow 1s^2\,^1S_0$). The balance between these two depopulation mechanisms of the forbidden line determines the ratio f/i of forbidden and intercombination line, since the excitation f $\rightarrow$ i opens an alternative channel for the depopulation of the f line via the i line. The density diagnostics are based on the assumption that the excitation f $\rightarrow$ i is only performed by electron collisions, but in some cases photons with the corresponding energy can be provided from, e.g., the stellar surface. Radiative transitions f $\rightarrow$ i can thus compete with the density dependent collisional transitions. Inference of densities n_e is done using the formula

$$\frac{\mathrm{f}}{\mathrm{i}} = \frac{R_0}{1 + \phi/\phi_c + n_e/N_c} \tag{1}$$

with R_0 the low-density (and low radiation field) limit, ϕ/ϕ_c the radiation term, and N_c the density where f/i falls to half its low-density value. Eq. 1 shows that radiation and collisions influence the f/i ratio in exactly the same fashion.

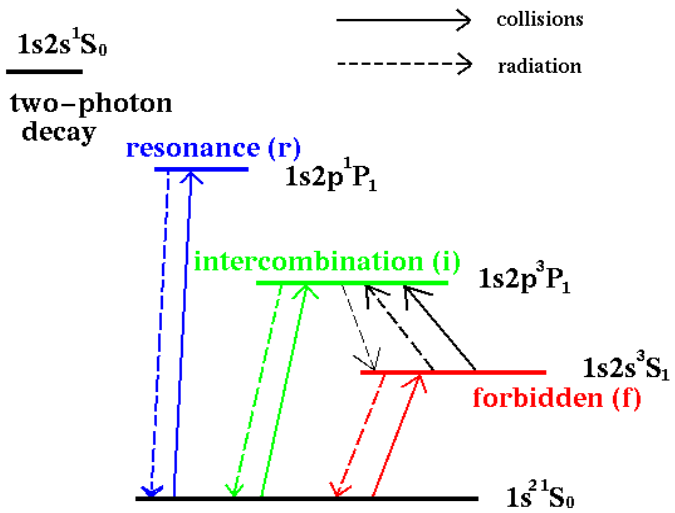

Figure 2. Simplified term diagram of He-like triplets in a collisional plasma with the resonance (r), the intercombination line (i), and the forbidden line (f). The excitations are performed exclusively by collisions. This may not be true for the transition f $\rightarrow$ i.

2.1. Measuring the radiation term ϕ/ϕ_c

A detailed description of how to measure the radiation term is given by Ness et al. (2001b). Basically the UV flux is measured at the wavelength for the transition f $\rightarrow$ i with the IUE satellite and is converted into an intensity to be compared with Planck curves for different radiation temperatures in order

to find the correct radiation temperature. The correct Planck curve is used to calculate ϕ/ϕ_c following Blumenthal et al. (1972). The results for Procyon and Algol are shown in Tab. 1. The radiation term is calculated using a dilution factor W accounting for the extension and the distance of the radiation source with respect to the X-ray emitting plasma. For Procyon $W = 1/2$ is used, but for Algol we use $W = 0.01$ (cf. Ness et al. 2001c, and Mewe & Schrijver 1978), because we assume the companion B star to be the dominant UV source (cf. Sect. 3).

Table 1. Measured radiation temperatures and radiation terms for Procyon (P) and Algol (A). n_e^* is the density obtained when neglecting the radiation field (ϕ/ϕ_c=0)

	C V		N VI		O VII		Ne IX	
	P	A	P	A	P	A	P	A
T_{rad}/K	5530	–	5780	12070	5410	12710	–	13690
ϕ/ϕ_c	26.67	–	1.58	24.74	0.01	2.18	–	0.1
log n_e/cm^{-3}	<8.92	–	9.96	10.13	<9.6	10.54	–	12.35
log n_e^*/cm^{-3}	10.2	–	10.27	11.16	<9.6	11.04	–	12.36

3. The Algol system

As can be seen from Fig. 3 the Algol system consists of a K star and a B star. The inclination angle is $i = 81.5°$ and the stellar radii are both about 3 $R_\odot$. It is commonly assumed, that all the X-ray emission originates from the corona of the late type star, and the B star is X-ray dark. From the radiation temperatures measured with IUE (cf. Tab. 1) it can be concluded, that the B star dominates the UV emission. With Fig. 3 we wish to illustrate that estimating the influence of the UV radiation field on the density diagnostics with He-like triplets is more complicated for Algol than for Procyon. In the case of Procyon the UV field is provided from the surface of the F star, and the corona is illuminated uniformly. In the case of Algol the external radiation field from the B star illuminates only the coronal plasma facing the B star. The coronal plasma on the opposite side is shadowed by the K star itself. Our observations with the Chandra LETGS can thus be a composite of both illuminated and non-illuminated plasma. The fraction of illuminated plasma contributing to the X-ray emission depends on the geometrical configuration of the system at the time of observation and on the distribution of the coronal plasma above the K star. The geometrical configuration is shown in Fig. 3, where a uniform distribution of coronal plasma is assumed. In that case only half of the plasma is illuminated at phase $\phi = 0.75$ (at the beginning of the LETGS observation) and only very little plasma at the poles is illuminated at phase $\phi = 1.0$ (at the end of the observation). Since nothing is known about the distribution of the coronal plasma, the phasing information alone cannot be used to derive the fraction of illuminated plasma. The radiation terms in Tab. 1 represent the case of totally illuminated plasma,

$\phi/\phi_c = 0$ applies to the case of non-illuminated plasma.

Inspection of Tab. 1 shows, that for O VII the radiation field has no influence on the result for Procyon, but for Algol the densities with and without radiation field differ by a factor three. From the phasing information ($\phi = 0.74 - \phi = 1.0$) we conclude, that the radiation field cannot be neglected, but the full illumination or non-illumination can only be applied in the case of a very non-uniform spatial distribution of the coronal plasma.

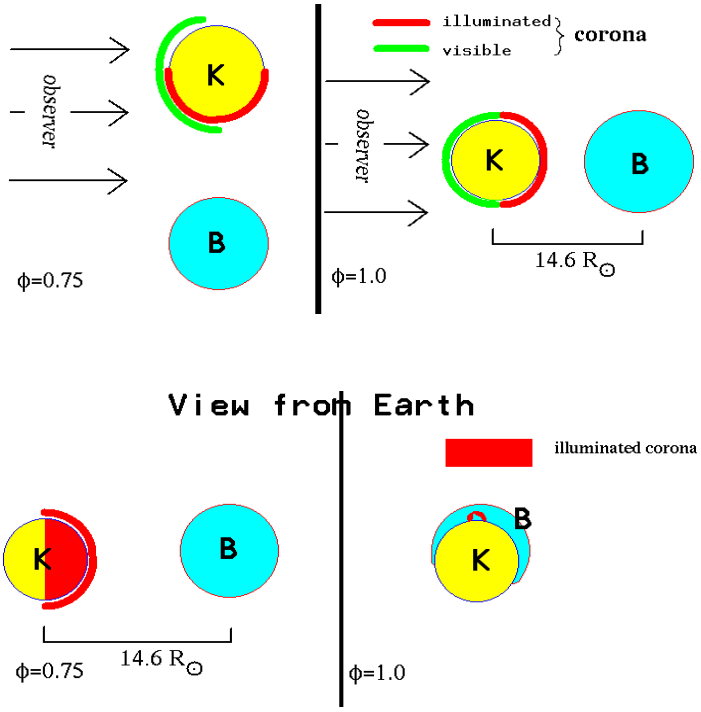

Figure 3. The Algol system with the K star as the X-ray source and the B star, the UV source. The phases correspond to the actual observation times.

References

Blumenthal G.R., Drake G.W. & Tucker W.H., 1972 ApJ 172, 205

Gabriel A.H. & Jordan C., 1969, MNRAS 145, 241

Mewe R. & Schrijver J., 1978, A&A 65, 99

Ness J.U., Mewe R., Schmitt J.H.M.M. et al., 2001a, A&A 367, 282

Ness J.U., Mewe R., Schmitt J.H.M.M. et al., 2001b, PASP in press (oral presentation at Cool Stars workshop CS12)

Ness J.U., Schmitt J.H.M.M., Burwitz V. et al., 2001c, in preparation

Porquet D., Mewe R., Dubau J. et al., 2001, A&A, in press

Pradhan A.K. & Shull J.M., 1981, ApJ 249, 82

Pradhan A.K., Norcross D.W. & Hummer D.G., 1981, ApJ 246, 1031

Chapter 7

Influence of UV radiation fields on density diagnostics with He-like triplets

Talk held in Boulder, Co, USA, August 2, 2001 at

Cool Stars 12

to be published in PASP Conf. Series

Influence of UV radiation fields on density diagnostics with He-like triplets

Jan-Uwe Ness[1], Rolf Mewe[2], Jürgen H.M.M. Schmitt[1], Anton J.J. Raassen[2,3]

Abstract. Spectroscopic density diagnostics based on He-like triplets are routinely used to investigate the solar corona. With the new instrumentation onboard Chandra and XMM this method of analysis can also be applied to stellar coronae.
In collision-dominated plasmas the forbidden line f ($1s2s\,^3S_1 \rightarrow 1s^2\,^1S_0$), disappears at high densities, and the intercombination line i ($1s2p\,^3P_{2,1} \rightarrow 1s^2\,^1S_0$) increases at higher densities on cost of the forbidden line. Therefore, the ratio f/i is used as a sensitive indicator of electron density. However, depopulation of the forbidden line compared to the intercombination line, is not always an indicator for high densities, it might also indicate that the depopulation of the forbidden line level ($1s2s\,^3S_1 \rightarrow 1s2p\,^3P_{2,1}$) is due to a UV radiation field instead of the collisions in a high-density plasma.
We illustrate this effect with IUE measurements of Capella, Procyon, Algol and α Cen A and α Cen B and a simulation showing the trend of the radiation fields when regarding stars with different surface temperatures. Focusing on the triplets of C V, N VI, O VII and Ne IX, we show that the radiation fields can have significant influence on the density analysis of the low-Z He-like ions of C, N and O. We present Chandra LETGS measurements and calculate the densities accounting for the measured radiation fields and neglecting them. The sources of the UV radiation are assumed to be the respective stellar surfaces, but in the case of Algol the radiation is supplied by the companion B star. A detailed investigation of whether the observed part of Algol's corona is actually illuminated by the radiation field of the B star, is necessary.

1. Introduction

The method of using He-like triplets for determination of electron densities in high temperature plasmas has been developed by Gabriel & Jordan (1969). It has been refined by, e.g., Blumenthal et al. (1972), Mewe & Schrijver (1978),

[1]Universität Hamburg, Hamburger Sternwarte

[2]Space Research Organization of the Netherlands

[3]Astronomical Institute Amsterdam

Pradhan et al. (1981), Pradhan & Shull (1981), and Pradhan (1982). The method has been exploited for the Sun quite extensively, but was not accessible for other stars until the advent of the high-resolution spectrometers on Chandra and XMM. A recent revision of the He-like line ratio technique has been carried out by Porquet et al. (2001) (see also Mewe et al. 2001).
In this paper we will explain the principle of how the lines of He-like triplets react to density effects and how UV radiation can interfere with these effects. We will then show that the radiation field parameters for the density diagnostics can be measured. Some LETGS measurements will be introduced in Sect. 4 where the influence of radiation fields on the low-density limit is shown. We will finally give an impression in which cases UV radiation fields must be measured and included in the analysis.

2. Atomic physics of He-like triplets

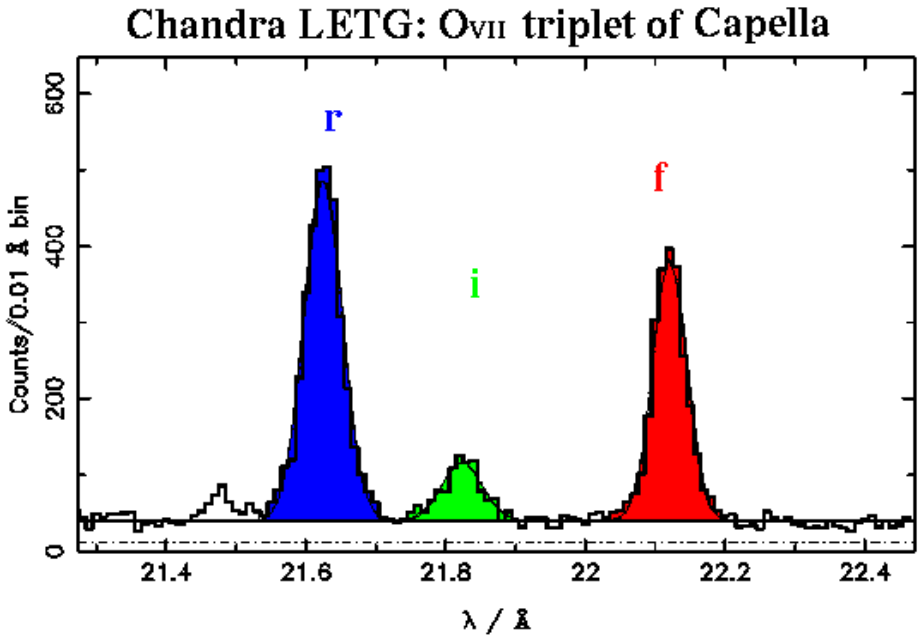

Figure 1. LETGS measurement of Capella's corona: O VII triplet.

He-like ions are ions consisting of a core with two electrons. The most prominent lines emitted by He-like ions are the He-like triplets. In Fig. 1 we show a measured spectrum of the O VII triplet for Capella. The three important transitions resonance r ($1s2p\,^1P_1$), intercombination i ($1s2p\,^3P_1$) and forbidden f ($1s2s\,^3S_1$) are denoted. The ground state is $1s^2\,^1S_0$. The term diagram with corresponding colors as in Fig. 1 is shown in Fig. 2.

Most important for the density diagnostics is the transition between f and i, thus $1s2s\,^3S_1 \rightarrow 1s2p\,^3P_1$. In low-density plasmas this transition should not occur. In higher densities this excitation can be triggered by collisions, because

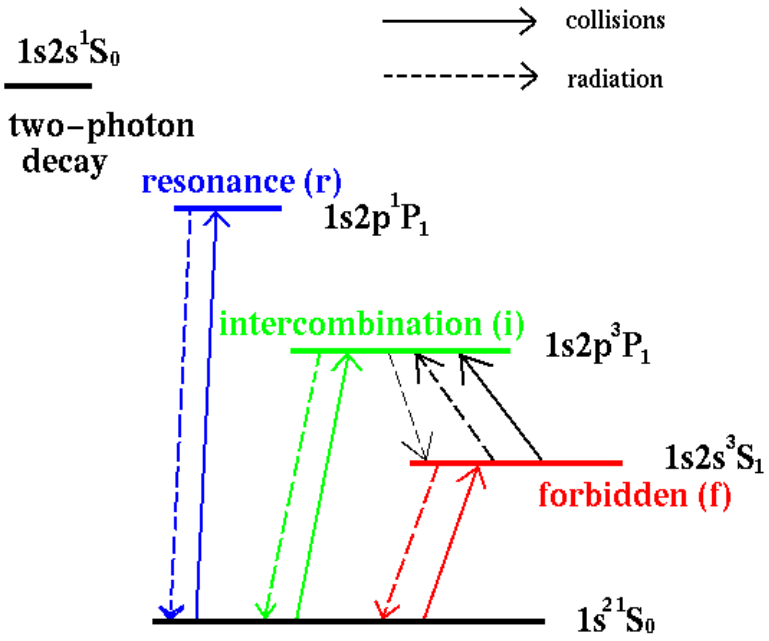

Figure 2. Simplified term diagram of He-like triplets.

the $1s2s\,^3S_1$ level is metastable, thus allowing sufficient time for suffering from collisions. In comparison with the low-density case, more de-excitations via the intercombination level will be encountered, thus the intercombination line will become stronger, and the forbidden line will become weaker. The ratio f/i is therefore a very sensitive density indicator.
But, as can also be seen from Fig. 2, this decisive transition can also be excited by photons with the energy dE = E_f-E_i. dE lies in the UV range for the commonly used He-like ions. In order to decide whether photons with the respective energy are supplied one needs to look out for strong UV fields in the vicinity of the emitting plasma. When investigating coronal plamas the stellar surface is a candidate, but we will find that even companion stars are also good candidates for the sources of significant UV radiation.

As can be seen from Fig. 2 the influence from a radiation field should compete with collisions on the same level. A term accounting for the radiation field has first been included in the density diagnostics by Gabriel & Jordan (1969). In our analysis we use the relation

$$\frac{\mathrm{f}}{\mathrm{i}} = \frac{R_0}{1 + \phi/\phi_c + n_e/N_c} \qquad (1)$$

with R_0 the low-density (and low radiation field) limit, ϕ/ϕ_c the radiation term, n_e the desired electron density, and N_c the density where f/i falls to half its low-density value. Densities are derived by just comparing measured f/i values with the errors with the theoretical curve represented by the right side of Eq. 1.

UV radiation fields are accounted for by using $\phi/\phi_c \neq 0$. The atomic parameters R_0 and N_c are provided by, e.g., Pradhan & Shull (1981).

3. Measuring the influence of UV radiation fields

From Eq. 1 it can be seen that the radiation field is represented by the term ϕ/ϕ_c in the analysis. The task is now to find adequate values for ϕ/ϕ_c. This is done by first finding the wavelength for the transition f $\rightarrow$ i (cf. Mewe & Schrijver 1978) for each individual ion. The values used in our analysis are listed in Tab. 1.

Table 1. Wavelengths for the transition $1s2s\,^3S_1 \rightarrow 1s2p\,^3P_{2,1}$ for C V, N VI, O VII and Ne IX. Also ionization potentials used in Eqs. 6 and 7 are listed.

	C V	N VI	O VII	Ne IX
$\lambda_{f\rightarrow i}$/Å	2272	1900	1630	1266
I_{pot}/eV	392.1	552.1	739.3	1195.3

The level $1s2p\,^3P_{2,1}$ is split up into three levels, but the mean value of the three transition energies can be used. A good reference is the use of databases, e.g. the NIST[1] server or the Kurucz[2] line list.
The next step will be to find a flux from the star at the respective wavelength. For our analysis we used IUE data, obtained from the IUE[3] archive. But also the HST-STIS[4] archive can be used. The measured flux can be converted into an intensity with

$$I_\lambda = F_\lambda \frac{d^2}{R^2} \frac{1}{2\pi(1-\frac{\epsilon}{2})}\,, \tag{2}$$

with the distance of the star d, the stellar radius R, and the linear limb darkening coefficient ϵ. ϵ can be obtained from, e.g., Díaz-Cordovés et al. (1995). The thus obtained intensity can be compared with a set of Planck curves

$$I_\lambda = W \frac{2hc^2}{\lambda^5} \frac{1}{\exp\left(\frac{hc}{\lambda k T_{\rm rad}}\right) - 1} \tag{3}$$

in order to infer a radiation temperature $T_{\rm rad}$. The dilution factor W is calculated with

$$W = \frac{1}{2}\left[1 - \left\{1 - \left(\frac{r_\star}{a}\right)^2\right\}^{1/2}\right] \tag{4}$$

[1] http://physics.nist.gov/cgi-bin/AtData/lines_form

[2] http://cfa-www.harvard.edu/amdata/ampdata/kurucz23/sekur.html

[3] http://ines.laeff.esa.es/cgi-ines/IUEdbsMY

[4] http://archive.eso.org/archive/hst/

(Mewe & Schrijver 1978) with the stellar radius $r_\star$, and the distance a between the UV source and the corona. For the case of the stellar surface to be the UV source, $a = r_\star$, thus $W = 1/2$ is commonly used.
The correct Planck curve u_ν is used to calculate the term ϕ/ϕ_c with

$$\frac{\phi}{\phi_c} = \frac{3(1+\mathrm{F})c^3}{8\pi h\nu^3} \frac{\mathrm{A}(2\,^3\mathrm{P} \rightarrow 2\,^3\mathrm{S})}{\mathrm{A}(2\,^3\mathrm{S}_1 \rightarrow\ 1\,^1\mathrm{S}_0)} u_\nu \tag{5}$$

(Blumenthal et al. 1972) with $\phi_c = \mathrm{A}(2\,^3\mathrm{S}_1 \rightarrow\ 1\,^1\mathrm{S}_0)/(1+\mathrm{F})$, transition probabilities $\mathrm{A}(j \rightarrow k)$, and u_ν the spectral energy density at the appropriate $2\,^3\mathrm{P}_1 \rightarrow\ 2\,^3\mathrm{S}_1$ frequency ν. The factor 3 is the ratio of the statistical weights of the levels $2\,^3\mathrm{P}$ and $2\,^3\mathrm{S}$. F is approximated by Blumenthal et al. (1972) through

$$\mathrm{F}(\xi) = \frac{3\xi\mathrm{H}(\xi)exp(\xi/4) + 1.2\xi + 2\mathrm{H}(\xi) + 2}{3\xi exp(\xi/4) + 0.6\xi\mathrm{H}(\xi) + \mathrm{H}(\xi) + 1}, \tag{6}$$

where

$$\mathrm{H}(\xi) = \frac{\mathrm{C}(1\,^1\mathrm{S} \rightarrow\ 2\,^3\mathrm{S})}{\mathrm{C}(1\,^1\mathrm{S} \rightarrow\ 2\,^3\mathrm{P})}, \tag{7}$$

with $\xi = I_{\mathrm{pot}}/kT_{\mathrm{rad}}$ and the collisional excitation rate coefficients $\mathrm{C}(j \rightarrow k)$. Values for the ionization potentials I_{pot} for each ion are given in Tab. 1 (cf., e.g., Pradhan & Shull 1981). Collisional excitation rate coefficients $\mathrm{C}(j \rightarrow k)$ can be taken from Pradhan et al. (1981). The described method has been applied by Ness et al. (2001) for the ions C V, N VI, and O VII for the stars Capella and Procyon.

4. Application of the method

The method described in Sect. 2 has been applied to the stars Capella, Procyon, and Algol. In Fig. 3 the theoretical curve from Eq. 1 is plotted in comparison with the f/i value measured with Chandra LETGS for Algol. The atomic parameters for O VII from Pradhan & Shull (1981) were used. From the measured UV flux $f = 2.2\,10^{-9}$ erg/cm^2/s/Å we derive a radiation temperature of 12700 K. Since this temperature is not typical for a K star (the most probable X-ray source in the Algol system) it is rather to assume, that the UV radiation is provided by the companion B star. We therefore applied a dilution factor $W = 0.01$, accounting for the distance (a=14.6 R$_\odot$) and the radius (R=3.5 R$_\odot$) of the companion star for calculating the radiation term $\phi/\phi_c = 2.18$. Despite of the much smaller dilution factor, the O VII triplet is only in the case of Algol really influenced by the radiation field. For Procyon and Capella it can be neglected. This can be seen from Tab. 2, where all steps are recorded according to Eqs. 2 to 7 for the stars Capella, Procyon, and Algol. As can be seen, Capella has the lowest temperatures, while the F star Procyon is much hotter and Algol's B star is the hottest star.

In Tab. 3 we present the results from our density diagnostics with and without (ϕ/ϕ_c=0) radiation fields. The f/i ratios have been obtained with Chandra LETGS. As can be seen, the densities are overestimated when leaving out the effects of radiation fields. But in the case of Algol, an exact estimate is more

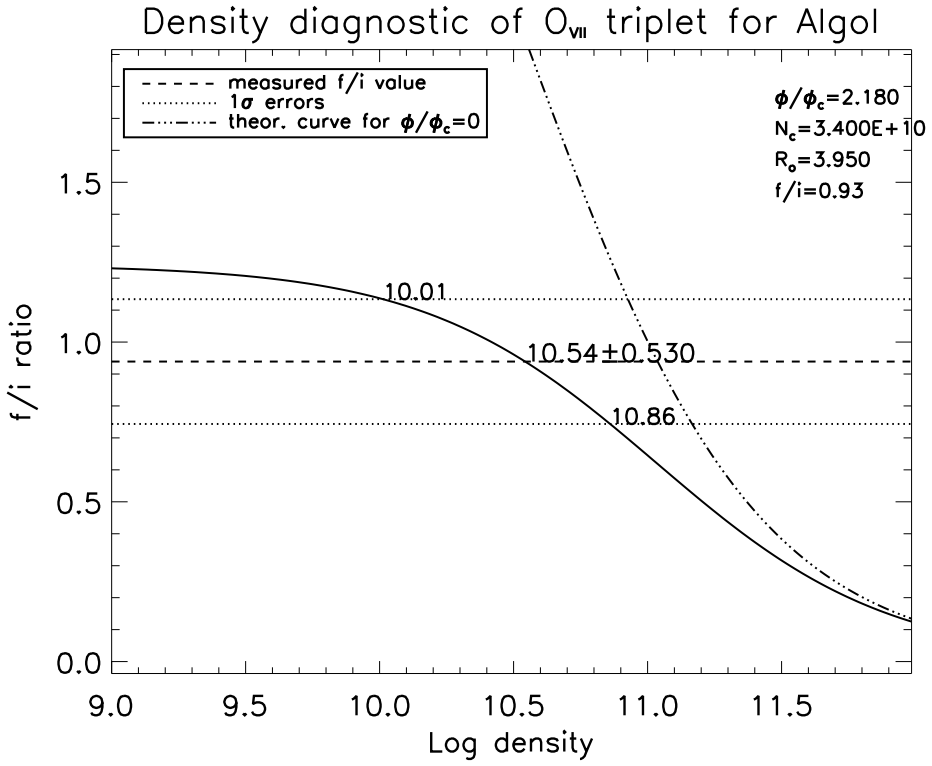

Figure 3. Inferring densities from the line ratio f/i (broken line: Chandra LETGS measurement, with errors dotted) for the example of Algol. The term $\phi/\phi_c = 2.18$ was measured with IUE, and the theoretical curves given with (solid line) and without (line-dotted line) radiation term (i.e. ϕ/ϕ_c=0).

complicated depending on the chosen geometry, since only half of the corona is illuminated by the companion B star, and the influence of the UV radiation depends on how much of the illuminated corona we actually observe. This consideration is discussed in detail by Ness et al. (2001a) and Ness et al. (2001b).

5. Results

5.1. The low-density limit

In Eq. 1 the low-density limit R_0 is introduced as an atomic parameter representing the ratio f/i to be measured when no transitions f $\rightarrow$ i take place, thus $\phi = 0$ and $n_e = 0$. For the purpose of density diagnostics the low-density limit puts a constraint on the range of measurable densities. When significant radiation fields influence the density diagnostics, this does not necessarily mean that no density diagnostics can be performed, but the range of measurable densities will be reduced. This is illustrated with Fig. 4, where the reduced low-density limit $R_0/(1 + \phi/\phi_c)$ is plotted versus the atomic number Z. The black curve represents the isolated values R_0 taken from Pradhan & Shull (1981).

Table 2. Investigation of the influence of the stellar radiation fields for Capella ([1]), Procyon ([2]) and Algol ([3]). Measured fluxes from the IUE satellite F_λ are converted to intensity I_λ taking into account limb darkening effects using $\epsilon = 0.83$ (Capella), $\epsilon = 0.724$ (Procyon) and $\epsilon = 0.44$ (Algol). The dilution factor is 0.5 except for Algol ($W = 0.01$).

	C V	N VI	O VII	Ne IX
$\frac{F_\lambda}{(10^{-10}\frac{\text{ergs}}{\text{cm}^2\,\text{s}\,\text{Å}})}$				
1	0.2 ± 0.05	0.12 ± 0.05	0.025 ± 0.005	
2	1.5 ± 0.4	0.7 ± 0.3	0.06 ± 0.03	
3		20 ± 2	22 ± 2.2	20 ± 6
$\frac{I_\lambda}{(10^4\frac{\text{ergs}}{\text{cm}^2\,\text{s}\,\text{Å}\,\text{strd}})}$				
1	1.98 ± 0.5	1.19 ± 0.3	0.25 ± 0.5	
2	21 ± 5	9.8 ± 4	0.84 ± 0.4	
3		9100 ± 910	9980 ± 100	9100 ± 270
T_{rad}/K				
1	4590 ± 100	4980 ± 150	5030 ± 50	
2	5530 ± 150	5780 ± 200	5410 ± 300	
3		12060 ± 190	12710 ± 190	13690 ± 560
ϕ/ϕ_c				
1	2.54 ± 0.86	0.2 ± 0.1	0.003	
2	26.67 ± 9.3	1.58 ± 0.84	0.01 ± 0.015	
3		24.74 ± 2.41	2.18 ± 0.29	0.1 ± 0.03

As can be seen from Fig. 4 the influence of the radiation field is only important for C V and N VI for all the stars except for Algol. For the ions with higher Z the influence of the radiation fields becomes smaller. For Ne IX (Z=10) a measurable influence is perhaps only encountered in the case of Algol.

5.2. Densities

In order to demonstrate the effect of radiation fields on the results of the density diagnostics, we calculated the expected densities for the ions C V, N VI, O VII and Ne IX assuming a hypothetically measured ratio f/i=3.0 (Fig. 5 upper panel) and a dilution fcator $W = 1/2$. The radiation field is given in terms of radiation temperatures. To give an orientation, the spectral types of stars corresponding to the temperatures are indicated. As can be seen from Fig. 5 (upper panel) the resulting densities are constant as long as the radiation temperatures are low. For higher radiation temperatures the densities calculated for f/i=3.0 are much smaller. This effect can be seen to be most severe for C V, while higher radiation temperatures can be tolerated for Ne IX.
The same procedure has been applied for a hypothetical measurement of f/i=1.0. As can be seen from Fig. 5 (lower panel) the obtained densities are higher and the results are less sensitive to high radiation temperatures. While in coronae with low densities (f/i=3.0) an F star can already harm the density diagnostics with O VII, the results in the density diagnostics are not influenced by the same radiation field in the case of a high-density plasma with f/i=1.0.

Table 3. Results of density diagnostics from Chandra LETGS measurements with and without radiation fields for the stars Capella, Procyon, and Algol. In addition the stellar parameters distance d, effective temperature $T_{\rm eff}$ and linear limb darkening parameter ϵ are given.

	Capella G1III/G8		Procyon F5IV-V		Algol K2IV/B8V	
d/pc	13		3.5		31	
$T_{\rm eff}$/K	5700		6530		4500/13000	
ϵ	0.83		0.724		0.44	
C V	f/i=1.48		f/i=0.48		*no detection*	
ϕ/ϕ_c	2.54	0	26.67	0	–	–
$\log(n_e)$	9.42 ± 0.21	9.66 ± 0.13	< 8.92	10.2 ± 0.12	–	–
N VI	f/i=1.78		f/i=1.33		f/i=0.21	
ϕ/ϕ_c	0.2	0	1.58	0	24.74	0
$\log(n_e)$	9.86 ± 0.12	10.09 ± 0.09	9.96 ± 0.23	10.27 ± 0.13	10.13 ± 0.93	11.16 ± 0.23
O VII	f/i=4.0		f/i=3.28		f/i=0.94	
ϕ/ϕ_c	0.003	0	0.01	0	2.18	0
$\log(n_e)$	<9.4	<9.4	<9.6	<9.6	10.54 ± 0.53	11.04 ± 0.13

6. Conclusions

From our analysis of the influence of UV radiation fields on the density diagnostics with He-like ions we conclude, that in the analysis of coronal plasmas it is important to keep this effect in mind. When leaving out the radiation field, one might obtain overestimated densities.
We have shown, that the radiation effects can be taken care of with the term ϕ/ϕ_c which again can be measured. With reliable measurements of ϕ/ϕ_c one can get improved densities. It has also been shown, that the influence of radiation fields on the density diagnostics are most severe for the low-Z ions C V and N VI, although for strong UV sources also O VII might be influenced. When investigating individual stars, one needs to take special care of this effect when dealing with hot stars with high $T_{\rm eff}$.
We want to point out, that the effect from UV radiation is only one major effect that might influence the density diagnostics. There are other effects like blended dielectronic satellite lines to each line of the triplets. This affects especially the high-Z ions like Ne IX, Mg XI, and Si XIII (Porquet et al. 2001). Also recombination from H-like ions can be important for photo-ionized plasmas or innershell ionization of Li-like ions in transient plasmas (Mewe et al. 2001).

Acknowledgments. J.-U.N. acknowledges financial support from Deutsches Zentrum für Luft- und Raumfahrt e.V. (DLR) under 50OR98010.
The Space Research Organization Netherlands (SRON) is supported financially by NWO.

References

Blumenthal G.R., Drake G.W. & Tucker W.H., 1972, ApJ 172, 205

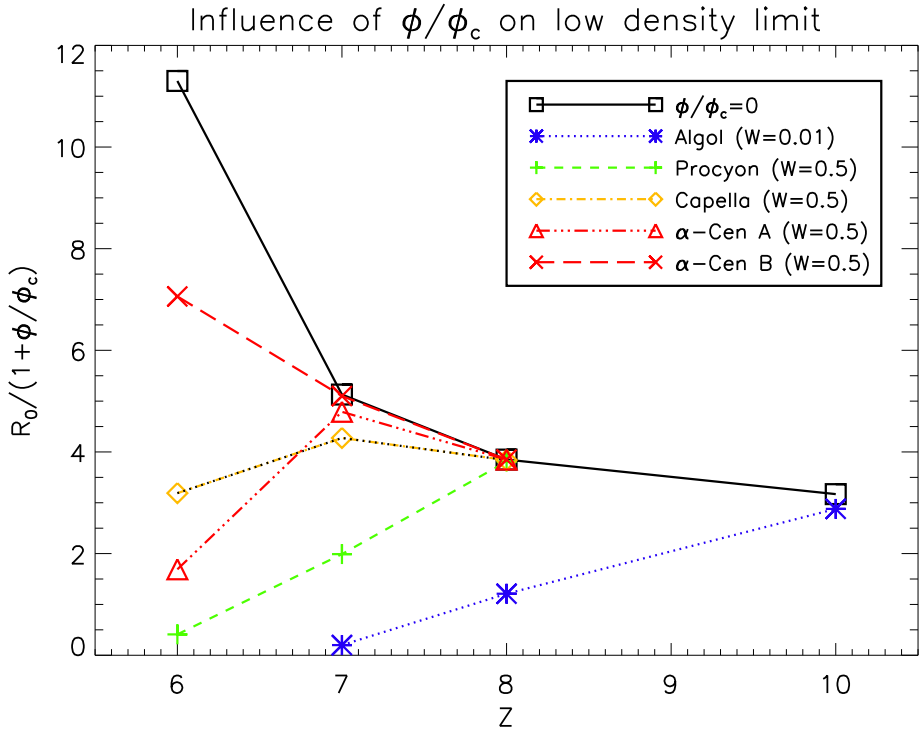

Figure 4. Influence of different radiation fields on the low-density limit restricting the density diagnostics. W is the dilution factor applied for the geometry of the stars. Plotted is the expected f/i ratio for the case $n_e = 0$ (cf. Eq. 1) versus atomic number Z.

Díaz-Cordovés J., Claret A. & Giménez A., 1995, A&AS 110, 329

Gabriel A.H. & Jordan C., 1969, MNRAS 145, 241

Mewe R. & Schrijver J., 1978, A&A 65, 99

Mewe R., Porquet D., Raassen A.J.J., et al., 2001, PASP, in press (poster 11.08 presented at Cool Stars workshop CS12)

Ness J.-U., Mewe R., Schmitt J.H.M.M. et al., 2001, A&A 367, 282

Ness J.-U., Schmitt J.H.M.M., Burwitz V. et al., 2001a, in preparation

Ness J.-U., Mewe R., Schmitt J.H.M.M. et al., 2001b, PASP, in press (presentation at Stellar Coronae 2001)

Porquet D., Mewe R., Dubau J. et al. 2001, A&A, in press

Pradhan A.K. & Shull J.M., 1981, ApJ 249, 82

Pradhan A.K., Norcross D.W. & Hummer D.G., 1981, ApJ 246, 1031

Pradhan A.K., 1982, ApJ 263, 477

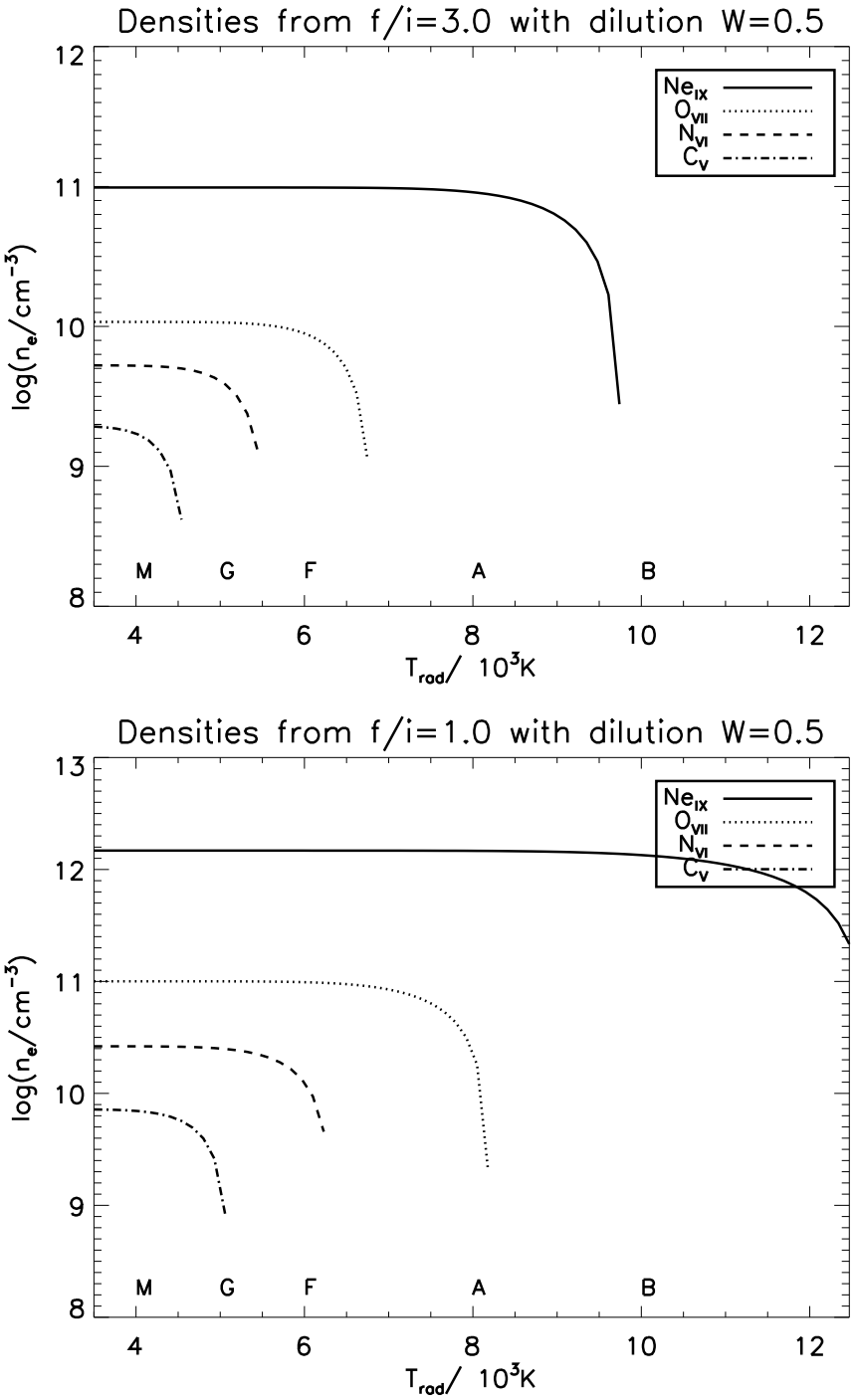

Figure 5. Simulation of derived densities for a hypothetic measurement of f/i=3.0 (upper panel) and f/i=1.0 (lower panel) as a function of radiation temperatures. To give an impression the spectral types M to B are given.

Chapter 8

Summary and concluding remarks

8.1 Results of density diagnostics

The general scope of this work is to measure densities for coronal plasmas in the temperature regime between 2 MK and 20 MK. For the sample of stars investigated in this work, basically two methods are applied, the He-like triplets and the Fe XXI line ratios (cf. Sect.1.4). The results obtained with these methods are as follows:

- The He-like triplets cover a large range of temperatures and densities.
  - The densities and temperatures measured with the He-like ions are listed in Tab. 8.1.
  - Si XIII, Mg XI, and Ne IX are formed at high temperatures and are sensitive at very high densities which are not reached by all stars in my sample.
  - O VII and N VI are formed at lower temperatures I measure:
    - for inactive stars f/i ratios close to low density limit
      → comparable with quiescent sun
    - for active stars higher densities
      → comparable with solar flares.
    - The low density measurements for three active stars are against this trend
    - All three are binaries with both stars being potential X-ray sources:
      - UX Ari: G5V/K0IV
      - Capella: G1III/K0III
      - HR 1099: G5IV/K1IV
    - Larger emitting volumes in RS CVn systems are a possible explanation.
  - C V is measured only in the inactive stars with low densities
  - The influence of UV radiation fields are measured and accounted for in the analysis.
- Analysis with Fe XXI:
  - The method is density sensitive at lower densities than Si XIII but is formed at similar temperatures.

  - Still only low density limits are measured for Algol and Capella.

8.2 Comparison with the Sun

The line ratios of He-like triplets are compared with a large number of solar observations of these lines in this work. This can be summarized as follows:

- C V and N VI: only few data for the Sun are found in the literature.
  - Solar flare f/i ratios are reported lower than quiescent values
    $\Longrightarrow$ this indicates higher densities during flares.
- Comparison of O VII measurements:
  - The inactive stars are in bulk of solar observations.
  - Algol has a significant lower f/i ratio than any solar measurement.
  - The G-ratio is around 1 for all stars in my sample, but solar G-ratios scatter.
  - ϵ Eri has an f/i ratio comparable with solar flare data.
  - However, solar data are not unambiguous
    * It is not always clear in which regions the reported values were measured
    * low spatial resolution
    * different instrumentation
  - f/i ratios of Capella, Procyon, α Cen A and B, and UX Ari are close to the low density limit
    $\Longrightarrow$ O VII emitting layers of these stars are similar to the Sun
    Algol has a much higher density (even when accounting for the radiation field from the B star comanion)
  - Solar flare data are consistent with high density plasmas.

8.3 Results of analyzing radiation fields

Special effort in this work is dedicated to the analysis of the influence of radiation fields on the analysis of densities with the He-like triplets. The results are:

- The influence of radiation fields can be determined independently from UV spectra, e.g., IUE.
- UV radiation fields must be included in analysis.
- Effects from radiation fields are most severe for
  - hot stars
  - low Z ions
- Without considering radiation fields, densities are overestimated.

Table 8.1 *Results for O VII and N VI. The errors are 1σ errors. For each ion the measured He-like ratios R=f/i and G=(f+i)/r, and the ratios Ly$_\alpha$/r are given. The derived T(Ly$_\alpha$/r) and T(G) and the densities log(n_e(f/i)) are also given. The radiation terms ϕ/ϕ_c used for the density diagnostics were measured with IUE as described by, e.g., Ness et al. (2001). Effective areas are taken from Deron Pease, Oct. 2000.*

	Algol	Capella	Procyon	ϵ Eri	α Cen		UX Ari
					A	B	
N_c=3.4 10^{10} cm^{-3}				**O VII**			
T_m=2.0 MK				[1] densities accounting for ϕ/ϕ_c			
f/i	0.96 ± 0.2	3.92 ± 0.25	3.22 ± 0.30	2.96 ± 0.32	3.44 ± 0.91	5.5 ± 1.39	>4
$T_{\rm rad}$/K	12710	5030	5410	0	4653	4181	0
ϕ/ϕ_c	2.18 ± 0.29	0.003	0.01	0	0	0	0
[1]log(n_e/cm^{-3})	10.5 ± 0.62	<9.38	9.28 ± 0.4	10.03 ± 0.23	9.64 ± 0.62	–	–
log(n_e/cm^{-3})	11.04 ± 0.12	8.36 ± 1.04	9.89 ± 0.26	10.06 ± 0.21	9.70 ± 0.58	–	–
T(Ly$_\alpha$/r)/MK	4.58 ± 0.15	3.38 ± 0.02	2.12 ± 0.03	2.89 ± 0.04	1.87 ± 0.07	2.10 ± 0.06	5.02 ± 0.17
T(G)/MK	1.72 ± 0.74	2.0 ± 0.13	0.96 ± 0.25	2.22 ± 0.30	1.65 ± 0.71	1.11 ± 0.54	3.14 ± 0.83
N_c=5.2 10^{9} cm^{-3}				**N VI**			
T_m=1.4 MK				[1] densities accounting for ϕ/ϕ_c			
f/i	0.21 ± 0.09	1.78 ± 0.25	1.33 ± 0.28	1.15 ± 0.55	2.19 ± 0.86	2.09 ± 1.4	1.44 ± 0.86
$T_{\rm rad}$/K	12060	4980	5780	0	4626	3994	0
ϕ/ϕ_c	24.74 ± 2.41	0.2 ± 0.1	1.58 ± 0.84	0	0.07	0.005	0
[1]log(n_e/cm^{-3})	10.20 ± 0.93	9.86 ± 0.12	9.96 ± 0.23	10.35 ± 0.33	9.95 ± 0.30	9.99 ± 0.65	10.23 ± 0.47
log(n_e/cm^{-3})	11.16 ± 0.23	10.09 ± 0.09	10.27 ± 0.12	10.35 ± 0.32	9.96 ± 0.30	10.00 ± 0.64	10.23 ± 0.47
T(Ly$_\alpha$/r)/MK	3.21 ± 0.20	2.58 ± 0.06	1.59 ± 0.04	2.33 ± 0.18	1.31 ± 0.09	1.71 ± 0.15	2.90 ± 0.19
T(G)/MK	<0.7	0.46 ± 0.28	1.28 ± 0.46	< 2.4	< 1.2	<1.8	2.1 ± 0.9

8.4 Particular comparison between Capella and Procyon

The two stars Capella and Procyon are quite different in their coronal properties, and a comparison between those stars is presented in this work. The results are basically:

- Plasma Temperatures: $T_{Proc} < T_{Cap}$
- Densities: $n_e(Procyon) \not< n_e(Capella)$
- $\Longrightarrow$ Pressure: $p_{Proc} \sim p_{Cap}$
- A comparison of fluxes from lines in highest ionization stages gives: $\frac{T_{max}(Capella)}{T_{max}(Procyon)} > 2$
- $\Longrightarrow$ typical loop scale length L: $L_{Capella} \geq 8 L_{Procyon}$ (derived from the loop scaling law $pL \sim T^3$)
- pressure for Procyon: 4.4 dyn/cm^2 ($p = 2 n_e k T$)
- $\Longrightarrow$ L$_{Procyon} = 2.7 \times 10^8$ cm
  $\Longrightarrow$ L$_{Capella} > 8 \times 10^9$ cm which is a significant fraction of Capella's radius.
- loop structures at large heights are unexpected
  $\Longrightarrow$ typical for active stars? Or typical only for RS CVn stars?

8.5 A detailed analysis of Algol

A very detailed analysis of an LETGS spectrum of the Algol system is presented in this work with a variety of results. These are:

- The light curve is slowly decreasing, and no convincing indication is found suggesting any flare activity.
- For the density measurements with He-like triplets, the radiation field from the companion B star must be accounted for.
  $\Longrightarrow$ Two scenarios are consistent with the data:
  - Low densities with a distribution of the plasma in a way that it is always immersed in the radiation field e.g., at the poles.
  - Higher densities, allowing a more uniform distribution of the emitting plasma.
- The continuum is consistent with a bremsstrahlung spectrum, and an upper temperature of ~ 15 MK.
- The assumption of a uniform distribution of identical loops leads to:
  - Loop lengths are smaller than the stellar radius $\Longrightarrow$ planar geometry, pressure equilibrium
  - Two scenarios are consistent with the data: 1) low pressure P= $8\,10^{16}$ K cm^{-3} and large filling factors > 0.45 or 2) high pressure P= $50\,10^{16}$ K cm^{-3} and small filling factors $0.07 < f < 0.21$

8.6 A special reduction software

A special software has been developed in the frame of this work. The basic features are:

- Strict conversation of Poissonian statistics by avoiding:
  - Subtraction of Poissonian statistics (background subtraction)
  - No division by effective areas, exposure time, etc.
- CORA can handle higher orders and/or redshifts
- Nice plots and LaTeX-tables are returned adequate for inclusion in publications
- Easy installation and handling
- Quick way of obtaining line counts and fluxes, but doing it right

8.7 Comparison with other recent work

The results presented in this work have to be interpreted in the context of other projects. Capella can be regarded a standard star for stellar X-ray emission and was observed by nearly all X-ray missions. In Chapter 1 measurements of Capella carried out with *Einstein* are mentioned. The LETGS data analyzed in this work are calibration data, which were also analyzed by Mewe *et al.* (2001). Their results are consistent with my results, but the hotter material was also analyzed. HETGS measurements of Capella are presented by, e.g., Canizares *et al.* (2000), and their analysis of the O VII triplet differs from my result, finding a higher density from a lower f/i ratio. From discussions with Nancy Brickhouse from Harvard-Smithsonian Center for Astrophysics, who participated in that project, a different treatment of the background could be the reason for the discrepancy, assuming or not assuming unresolved weak lines to make up a fraction of the source background. However, the instrumental differences between the HETGS and the LETGS in this wavelength region are quite large (cf. Fig. 1.8). While the LETGS can measure quite reliably in this wavelength region, the HETGS is designed for lower wavelengths, but the effective areas suffer from deep gradients in the wavelength region above $\sim$ 18 Å. This presumption is supported by the measurements presented by Audard *et al.* (2001). They analyzed an XMM-RGS spectrum of Capella and found similar densities for O VII emitting layers as I did. My conclusion from the comparison of these three instruments is that the O VII measurements from the HETGS must be treated with care. A detailed investigation of a Capella spectrum obtained with the HETGS is presented by Phillips *et al.* (2001), comparing these data with EUVE measurements. Their analysis of He-like triplets returned the higher densities for O VII, but only upper limits for Fe XXI, Ne IX, and Mg XI line ratios.

8.8 Future perspectives

The results obtained in this work are only the beginning of high-resolution spectroscopy in the X-ray wavelength band. Important aspects are discussed concerning the special

challenges associated with the new opportunities provided with the missions *Chandra* and XMM. The densities given in this work are rather low. The atomic physics utilized for the analysis provides good density diagnostics for plasma with temperatures ranging at around 2 MK and around 10 MK. However, densities below $\sim 10^9\,\mathrm{cm}^{-3}$ cannot be measured with these methods. Other methods providing density diagnostics in similar temperature regimes, but sensitive to lower densities than $10^9\,\mathrm{cm}^{-3}$ are highly desirable. An example is the Fe XII ion, formed at around 2 MK, thus in the same temperature regime as O VII. The ground state is $1s^2 2s^2 2p^6 3s^2 3p^3$ (or $^4S_{3/2}$), and forbidden transitions from $^2D_{3/2}$, $^2D_{5/2}$, $^2P_{1/2}$, and $^2P_{3/2}$ are density sensitive below $10^9\,\mathrm{cm}^{-3}$. These emission lines from Fe XII are accessible with the Hubble Space Telescope (HST), and measurements have been carried out by, e.g., Jordan *et al.* (2001) for ϵ Eri.
An interesting aspect in this work is the modeling of the continuum of the Algol spectrum returning quite encouraging results. In this work this was done in a provisional way, which is absolutely sufficient for the purpose pursued here. A more refined continuum model, consistent with measured line ratios, however, can be developed in a future effort. Emission measure modeling is a popular means of analyzing X-ray spectra. The presently available algorithms for this task, however, are optimized only for low-resolution spectra, and particular difficulties arise from the application to the new high-resolution spectra. New approaches are necessary in order to obtain emission measure distributions that can be used for obtaining reliable temperature and abundance distributions. Abundances can be used for a more and more precise picture of the FIP (First Ionization Potential) effect in combination with heating mechanisms. For the Sun, the low-FIP elements are over-abundant in the corona, suggesting a heating process, preferring ionized material to be transported up to the corona. The investigation of abundances in stellar coronae can help understanding the heating mechanism in other stars.